Moore, G.F., Taira, A., and Klaus, A., et al.
Proceedings of the Ocean Drilling Program, Initial Reports Volume 190

6. Site 1175[1]

Shipboard Scientific Party[2]

SITE SUMMARY

Site 1175 (proposed Site ENT-07A) was designed to penetrate the slope sediments that cover the large thrust-slice (LTS) zone just landward of a major out-of-sequence thrust (OOST). Investigation of the age and lithologic characteristics would provide information on (1) the history of accretion, uplift, and deformation of the prism and (2) sedimentation within a trench-slope basin.

We cored three lithostratigraphic units at Site 1175. Unit I (upper slope–basin facies) begins at the seafloor and ends at a sub-bottom depth of 224.75 meters below seafloor (mbsf). Lithologies include nannofossil-rich hemipelagic mud, volcanic ash, and thin turbidites that range in texture from sand to silty sand, clayey sand, and silt. The most characteristic feature of Unit I is the common occurrence of contorted stratification. There are eight discrete zones of soft-sediment deformation. Typical manifestations include variably inclined bedding, small-scale folding, and, in extreme cases, stratal fragmentation. The disruption was probably caused by submarine slumps and debris flows. Unit II (middle slope–basin facies) extends from 224.75 to 301.64 mbsf. Lithologies include hemipelagic mud, poorly sorted muddy sand to sandy mud, sporadic interbeds of volcanic ash, and rare occurrences of thin sand or silt turbidites. The unusual lithology of muddy sand is diagnostic of Unit II and probably was transported downslope by sandy debris flows or mudflows. Unit III (slope to prism transition) begins at 301.64 mbsf and ends at 435.40 mbsf. This unit is typified by carbonate-poor hemipelagic mud with numerous interbeds of silt and silty sand turbidites. The most striking lithology, however, is gravel to pebbly mudstone. Its characteristics include disorganized and poorly sorted clast fabric, lack of internal stratification, partial to complete support of clasts by a matrix of clayey silt, and subrounded to rounded clasts up to 5.5 cm in size. A polymictic clast population was transported downslope by debris

[1]Examples of how to reference the whole or part of this volume.
[2]Shipboard Scientific Party addresses.

Ms 190IR-106

flows. The boundary between the lowermost slope sediment and the top of the accretionary prism cannot be defined with certainty using lithologic criteria, but it probably occurs within the upper 25–30 m of Unit III.

Site 1175 exhibits little evidence for tectonic deformation. However, the upper 205 m shows intervals of recumbent, isoclinal slump folding and disaggregated sediment interlayered with subhorizontal intact bedding. Fold orientations suggest the slumping was northward directed. Below 220 mbsf, bedding is subhorizontal except for localized chaotic zones between 350 and 388 mbsf and dips up to 21° at 400 mbsf. Core-scale faults, probably compaction related, occur from 298 to 302 mbsf and sporadically from 340 to 435 mbsf. Possible web structure occurs in sands at 406.9 and 425.8 mbsf; near the bottom of the hole, an indurated sand contains several low-angle small faults.

Biostratigraphic age control was provided by calcareous nannofossils that are well preserved and abundant throughout the section. Ten biostratigraphic events were identified within the nannofossil assemblages. The continuous sedimentary record spans the time interval from the Pliocene (Zone NN18) through the Pleistocene (Subzone NN21b). Based on the biostratigraphic ages, sedimentation rates for the upper sedimentary units show high sedimentation rates (0.52 m/k.y.) for the upper to middle slope–basin deposits, with decreasing rates for the slope to prism transition (0.13 m/k.y.).

Hole 1175A inclination data after alternating-field (AF) demagnetization at 30 mT allowed interpretation of geomagnetic polarity changes from late Pliocene to Pleistocene. The 0.78-Ma Brunhes/Matuyama boundary is interpreted to occur at 298.80 mbsf (interval 190-1175A-32X-5, 80 cm). Seven short reversal events were observed in the Brunhes Chron and may represent geomagnetic excursions.

In Hole 1175A, pore fluids are less intensively modified from seawater than the pore fluids in Holes 1173A and 1174A. The main characteristics of the pore fluid concentration-depth profiles indicate that the intense microbially mediated reactions occur in the top <200 mbsf of the section. Microbial sulfate reduction is complete at ~15 mbsf. The alkalinity maximum also occurs at this depth. Only relatively small changes in the chemical gradients occur throughout the section and across the major lithologic boundaries in the abiogenic components. Volcanic ash alteration is insignificant because of the rather low geothermal gradient of 54°/km. Instead of ash alteration, as indicated by the Ca, Mg, and alkalinity concentration-depth profiles, carbonate, particularly dolomite, diagenesis is the dominant diagenetic reaction. Dolomite forms both by direct precipitation of authigenic dolomite and by replacement of precursor biogenic calcite, which is abundant in this section. Carbonate diagenesis should influence some of the index physical properties such as porosity and density. An unidentified silicate reaction occurring below the drilled section controls the concentration profiles of K, Na, Si, and alkalinity below ~300 mbsf, corresponding to lithostratigraphic Unit III. The inferred diffusion of lower chlorinity interglacial water into the pore fluids at Sites 1173 and 1174 is absent at this site. One possible explanation is that the signal has been erased by widespread slumping in Unit I.

The sediments at Site 1175 contain low inorganic carbon (~0.11–4.59 wt%), and carbonate contents range up to 40 wt%, resulting in very immature organic matter and low hydrocarbon abundances. The low sulfate and high methane concentrations in sediments below the sulfate

reduction zone and throughout Hole 1175A are consistent with a bacterial origin.

Bacterial abundance was enumerated in 18 samples obtained at Site 1175. The abundance near the surface is 6.97×10^7 cells/cm^3 and declines rapidly, which is consistent with the decrease in sulfate concentrations. Abundances increase below 14.6 mbsf, consistent with increases in methane concentrations. The sample at 50.8 mbsf is notable in that it contains 7.28×10^7 cells/cm^3 (i.e., slightly more bacteria than the near-surface sample). This is followed immediately with almost the lowest population enumerated of 3.71×10^5 cells/cm^3 at 59 mbsf. The deepest sample is 400 mbsf with 3.59×10^5 cells/cm^3, equivalent to 0.5% of the near-surface population. Estimates of drilling fluid intrusion into the interior of the cores examined at this site range from below detection to 0.02 µL/g. In addition to the onboard assays, 17 whole-round cores were taken for shipboard enrichment cultures, cell viability, and shore-based microbiological analysis to measure potential bacterial activities, culture microorganisms, characterize nucleic acids, and investigate fatty acid biomarkers.

Porosities within the upper slope–basin facies (Unit I) are characterized by high variability and decrease slightly with depth from values of 62%–70% at the mudline to 61%–68% at ~100 mbsf. Porosities decrease abruptly at ~100 mbsf to values of 57%–61% and then decrease gradually to the transition between the upper and middle slope–basin facies (220 mbsf). Below 220 mbsf (within the middle and lower slope–basin facies), porosity decreases more rapidly with depth than in the upper slope–basin facies, reaching values of 38%–47% at 400 mbsf. The rapid decrease in porosity below 220 mbsf coincides with increasing *P*-wave velocity. There is no clear change in porosity, bulk density, or grain density at the depth of the middle slope–basin/lower slope–basin facies boundary (301 mbsf; Units II and III). A spike of high velocity and impedance 20 m above this transition may correspond to a seismic reflector. The depth of this spike coincides with the depth of the upper unconformity on the depth converted seismic profile. Four successful in situ temperature measurements at Site 1175 indicated a thermal gradient of 0.054°C/m.

Gas-probe permeameter measurements illustrate the huge influence of lithology. Uniformly low values are given by the hemipelagic clays that dominate the section, whereas a coarse, friable black ash at 23 mbsf gave a measurement six orders of magnitude higher. Turbiditic sands between 60 and 90 mbsf also yielded exceptionally high values. Thin bands of white-gray ash also give relatively high values, in agreement with shallow, unaltered ash at the other sites.

This site revealed that the age of accretion of the LTS zone is very young (<2 Ma). The young age of the accretion indicates rapid growth of the frontal part of the Nankai accretionary prism, ~40 km oceanward growth in 2 m.y. This rate of growth provides a significant revision to first order constraints for kinematic, structural, and hydrogeologic modeling of the prism.

OPERATIONS

Site 1175 (ENT-07A)

A seafloor positioning beacon was dropped at 2230 hr on 22 June, establishing Site 1175. A new advanced hydraulic piston corer (APC)

bottom-hole assembly consisting of a 9.875-in polycrystalline diamond compact bit, a bit sub with a lockable float valve, a seal bore drill collar, landing saver sub, modified top sub, modified head sub, nonmagnetic drill collar, seven 8.25-in drill collars, a tapered drill collar, a crossover sub, six joints of 5.5-in drill pipe, and a crossover sub to 5-in drill pipe was assembled and run in the hole. The precision depth recorder indicated a seafloor depth of 3024.4 meters below rig floor (mbrf). The bit was positioned at 3010 mbrf, and the water-sampling temperature probe (WSTP) was deployed to take a seafloor water sample prior to establishing any circulation. The WSTP was recovered with traces of sediment on it, indicating that the water depth was shallower than anticipated.

Hole 1175A

After recovering the WSTP, the bit was positioned at 3006.7 mbrf and Core 1H was taken, recovering 7.12 m of core and establishing a seafloor depth of 3009.1 m (Tables T1, T2). Hole 1175A was then APC cored from the mudline to 92.7 mbsf (3101.8 mbrf), where Core 11H resulted in a short stroke and recovered 2.32 m of loose sand. The bit was washed ahead without coring to 100.8 mbsf (3109.9 mbrf) in an attempt to get through the loose sand. Core 12H from 100.8 to 110.3 mbsf (3109.9–3119.4 mbrf) recovered 9.58 m of sediment. Normal APC coring operations continued without unusual overpull until Core 22H (195.8–205.3 mbsf; 3204.9–3214.4 mbrf), which could not be pulled out of the formation. The drill-string spaceout was such that a short kelly was left after shooting the core; therefore, only 3 m of the core barrel could be drilled over. After drilling over these 3 m, the core barrel was pulled out with 120,000 lb of overpull and heavy circulation.

Twenty-two APC cores were taken from Hole 1175A, recovering 197.68 m of sediment from 199.5 m of cored section (99% recovery); 5.8 m was drilled without coring. After recovering Core 22H, the extended core barrel (XCB) coring system was used to obtain Cores 23X through 47X (205.3–445.5 mbsf) and recover 129.3 m of sediment (54%).

After terminating coring in Hole 1175A, the hole was displaced with 136 bbl of heavy mud. Because the formation contained a considerable amount of loose sand, the bit was pulled to 289.92 mbsf (3299.02 mbrf) with the top drive in place. The top drive was racked back, and the bit was pulled 153.7 m above the seafloor for the move to Site 1176. The bit cleared the seafloor at 0500 hr on 26 June, and the seafloor positioning beacon was released. The beacon was recovered at 0615 hr on 26 June, ending operations at Site 1175.

T1. Coring summary, p. 62.

T2. Coring summary by section, p. 63.

F1. Stratigraphic column, p. 27.

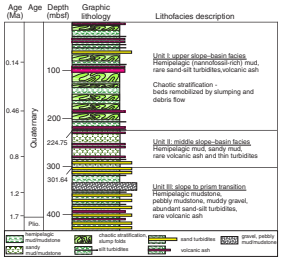

T3. Summary of stratigraphic relations, p. 69.

LITHOSTRATIGRAPHY

We recognized three lithostratigraphic units at Site 1175 (Fig. F1). All units represent stages of sedimentation during the creation and deformation of a small basin on the lower trench slope.

Unit I (Upper Slope–Basin Facies)

Unit I is Quaternary in age and extends from the seafloor to a depth of 224.75 mbsf (Table T3). This unit consists predominantly of nannofossil-rich hemipelagic mud (silty clay to clayey silt) interlayered with

volcanic ash and a few thin beds of sand, silty sand, clayey sand, and silt. Contorted stratification is conspicuous. The base of the unit is above a 55-cm-thick clayey sand (Section 190-1175-25X-1, 15 cm).

The hemipelagic mud in Unit I is gray, greenish gray, or olive green in color and homogeneous, faintly laminated, or mottled as a result of bioturbation. The composition includes abundant clay minerals and biogenic debris, together with lesser amounts of volcanic glass and lithic fragments (see **"Site 1175 Smear Slides,"** p. 45). Diatoms and sponge spicules are more common in the upper part of the unit, whereas nannofossils are more abundant in the lower part.

Volcanic ash beds in Unit I vary in thickness from <1 cm to >2 m (Fig. **F2**). The thickest ash deposit occurs near the top of Core 190-1175A-11H (92 mbsf) but was not recovered completely. Ash layers typically have sharp plane-parallel to irregular lower contacts and gradational upper contacts (Fig. **F3**). Color variations among and within individual ashes range from pale gray to dark gray, white with dark grains (salt and pepper), brown, pink, and greenish gray. Grain size varies from lapilli to fine ash; a grain-size range of 0.1–2.0 mm is most common. The volcaniclastic sediment is composed primarily of fresh glass shards or pumice plus variable amounts of nannofossil-rich silty clay, lithic clasts, and crystals of quartz, plagioclase, and pyroxene (see **"Site 1175 Smear Slides,"** p. 45).

Deposits of sand, clayey sand, and silt are present mainly as thin beds to laminae, but there are also a few thick-bedded units. These coarser-grained deposits have sharp bases, gradational tops, and normal grading (Fig. **F4**). The sand is coarse to fine grained and poorly sorted and includes foraminifers, siliceous and calcareous microfossils, quartz, feldspar, pyroxene, amphibole, volcanic glass, chert, and low-grade metasedimentary rock fragments (see **"Site 1175 Smear Slides,"** p. 45).

Contorted and disrupted stratification is the most noteworthy feature of Unit I. Common manifestations of soft-sediment deformation include steeply inclined stratification (beds and laminae) and small-scale recumbent to inclined folds with overturned beds (Fig. **F5**). In some cases, the hinge zones of these folds are exposed across the core face. Extreme cases of stratal dismemberment have resulted in curviplanar to irregular-shaped fragments of nannofossil-rich mud and ash engulfed in a matrix of contorted mud that is slightly different in color (Fig. **F6**). There are eight discrete zones of soft-sediment deformation and chaotic folding in Unit I ranging from 3 to >10 m in thickness.

The overall facies character of Unit I is consistent with conceptual models of deposition in a trench-slope basin that is isolated from the influx of coarse terrigenous sediment (e.g., Underwood and Moore, 1996). Sedimentation occurred initially through hemipelagic settling of nannofossil-rich mud, occasional turbidity currents, and air falls of volcanic ash. A higher concentration of calcareous nannofossils in the hemipelagic mud is consistent with deposition above the calcite compensation depth. The impressive zones of chaotic stratification evidently were caused by local remobilization of hemipelagic sediment. One likely triggering mechanism for such intraformational mass wasting is seismogenic loading. Another factor is the intrinsic gravitational instability of mud accumulating on steeply inclined bounding ridges of the slope basin, especially during episodes of uplift and tilting associated with offsets along out-of-sequence faults. Following the classification scheme of mass movements described by Martinsen (1994), we recognize a range of core-scale features that span a continuum from slump (coherent mass with considerable internal deformation) to debris

F2. Distribution and thickness of volcanic ash layers, p. 28.

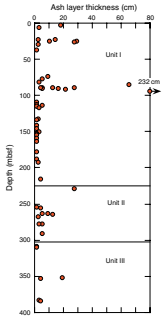

F3. Volcanic ash from Unit I, p. 29.

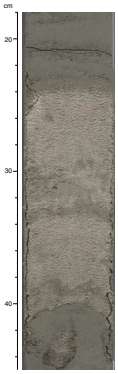

F4. Sandy turbidite of Unit I, p. 30.

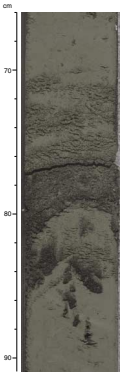

F5. Overturned ash bed from Unit I, p. 31.

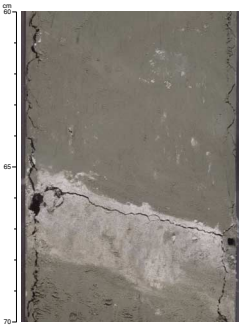

flow (remolded mass with plastic behavior). These designations are scale dependent, however, and there is no evidence of internal deformation within the failed masses at the scale depicted by seismic reflection profiles.

Unit II (Middle Slope–Basin Facies)

Unit II is Quaternary in age and extends from 224.75 mbsf (Section 190-1175A-25X-1, 15 cm) to 301.64 mbsf (Section 33X-1, 4 cm). Lithification of the fine-grained strata is more advanced than in Unit I, and there is an absence of features ascribed to soft-sediment deformation. The most distinctive lithology within Unit II is greenish gray sandy mudstone (Table T3). This relatively unusual type of sediment is poorly sorted and generally structureless. Faint dark green bands are present locally. Grain constituents include abundant nannofossils, clay minerals, monocrystalline quartz, volcanic glass, feldspar, metasedimentary lithic fragments, and polycrystalline quartz (see "Site 1175 Smear Slides," p. 45). Other lithologies within Unit II include a more typical hemipelagic mudstone (silty claystone to clayey siltstone), volcanic ash, and rare beds of sand. The hemipelagic mudstone is greenish gray to gray and massive, faintly laminated, or mottled as a result of bioturbation, with scattered *Zoophycos* and *Chondrites* trace fossils. Pyrite nodules, rounded pumice fragments, and sand patches are present locally. Diatoms, radiolarians, silicoflagellates, and sponge spicules are also present, but the percent of carbonate is generally lower than in Unit I. Thin beds and laminae of volcanic ash are scattered throughout Unit II (Fig. F2) and vary in color from pale brown and pale gray to dark gray. Most of the pyroclastic particles are composed of fresh volcanic glass with some crystals of plagioclase, quartz, amphibole, and pyroxene (see "Site 1175 Smear Slides," p. 45). In some cases the ash is intermixed with terrigenous silt, clay, and calcareous nannofossils; we view this mixing as indicative of remobilization during and/or after ash-fall events.

The most obvious distinction between Units I and II is the absence of chaotic stratal disruption within the middle slope–basin facies. Based on this contrast, we infer that the relief and seafloor gradients of nearby slopes were more subdued during the basin's intermediate phase of sedimentation. The distinctive sandy mudstone deposits were probably transported as relatively fine-grained debris flows or mudflows, with the sand-sized clasts fully supported by the muddy matrix. Delivery of the siliciclastic sand from detrital sources on Shikoku appears likely, based on compositional similarities with rock types currently exposed in the Outer Zone of Japan. Transport of sandy mud beyond the shelf edge could have occurred within transverse channels or as unconfined mudflows.

Unit III (Slope to Prism Transition)

The most distinctive feature of Unit III is the common occurrence of thin- to medium-bedded silt and sand turbidites (Table T3; Fig. F1). The top of Unit III is located just above a package of seven such sand beds (Section 190-1175A-33X-1, 4 cm). The deepest core within this unit is from 435.4 mbsf (Section 190-1175A-47X-CC, 30 cm). The most noteworthy lithology, although less common, is muddy gravel to pebbly mud. Hemipelagic mudstone and/or sandy mudstone is typically present between the coarse-grained beds.

F6. Chaotic bedding of Unit I, p. 32.

The sandy mudstone and hemipelagic mudstone lithologies in Unit III are typically greenish gray, gray, or green in color, and they may be homogeneous, faintly laminated, or mottled as a result of bioturbation. *Zoophycos* and *Chondrites* are present. Microfossils are generally less common than in comparable deposits of Unit II, although nannofossils are abundant locally. Rare laminae and thin beds of light gray vitric ash are scattered through the unit.

The sand and silty sand beds of Unit III are poorly indurated and thin to medium bedded. Plane-parallel laminae are the most common internal sedimentary structure. Cross-laminae and normal grading are less common. Color ranges from medium gray to greenish gray. These deposits are poorly sorted; grain size varies from very coarse sand to silt. Grains are subrounded to angular. Lower bed surfaces are sharp, and most are plane parallel; upper bed contacts are diffuse and gradational. Compositionally the sand is quartz rich, with subordinate amounts of sedimentary or metasedimentary lithic clasts, chert, feldspars, and minor to rare volcanic glass (see **"Site 1175 Smear Slides,"** p. 45). Woody plant fragments are common in some sands.

Five distinctive beds of poorly indurated muddy gravel to pebbly mud are present between 340 mbsf (Section 190-1175A-37X-1, 0 cm) and 347 mbsf (Section 37X-5, 118 cm). The pebbly mud is poorly sorted throughout, with a disorganized clast fabric, lack of internal stratification, and partial to complete support of clasts by a muddy matrix (Fig. **F7**). The matrix is composed of nannofossil-bearing silty clay, similar in composition to the typical hemipelagic deposits of Unit III. The clasts are rounded to subrounded and as large as 5.5 cm across. The polymictic population of clast lithologies includes abundant quartz, chert, and sedimentary to metasedimentary lithic fragments together with feldspar and minor volcanic clasts.

F7. Pebbly mudstone from Unit III, p. 33.

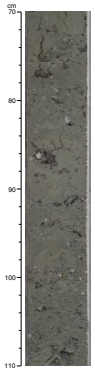

We infer that the sediments within Unit III were deposited by hemipelagic settling, mudflows, muddy turbidity currents, sandy turbidity currents, and pebbly debris flows. The clast population of the debris-flow deposits is consistent with a source that includes rock units currently exposed in the Outer Zone of southwest Japan (e.g., the Shimanto Belt). Deposition occurred in the lower part of a trench-slope environment, according to interpretations of seismic-reflection data. The original basin geometry and contact relations, however, have been obscured by subsequent tectonic disruption and intermixing across the basal unconformity of the slope basin. This process has been referred to as tectonic kneading (Scholl et al., 1980). Interpretation of the depositional environment for the lower part of the unit, therefore, remains ambiguous. Careful petrographic examination may reveal compositional differences between transverse and axial turbidite systems in the trench-wedge facies, although probably not between transverse-trench and transverse-slope turbidites.

Proportions of sandy turbidites and pebbly mud were high relative to hemipelagic setting during deposition of Unit III. Evidently, Site 1175 was adjacent to a through-going shelf to trench sediment conduit, perhaps a submarine canyon and trench fan system, early in its history. In the present day physiography of Nankai Trough, one nearby canyon and fan system of this type is Murotomisaki Canyon, ~10 km to the west of the Leg 190 drilling transect. A second example is Shionomisaki Canyon, which begins to the northeast off shore from the Kii Peninsula (Taira and Ashi, 1993). Submarine canyons are important for controlling sediment transport into both slope basins and trench-wedge environments (Underwood and Karig, 1980; Taira and Ashi, 1993). In

general, however, newly formed basins lower on the trench slope are less likely to connect directly to the shoreline via submarine canyons; their facies associations have been described as immature and consist mostly of hemipelagic mud and locally derived slumps and mudflows (Underwood and Bachman, 1982). Conceptual models of slope-basin evolution predict that uplift and downslope canyon-channel erosion will combine to increase coarse-grained siliciclastic influx to basins as they mature (Underwood and Bachman, 1982). As a consequence, stratigraphic successions should thicken and coarsen upward (Moore and Karig, 1976; Underwood and Moore, 1996). Rerouting of the transverse sediment delivery system must have occurred upslope of Site 1175 during uplift and rotation of the slope basin. Thus, rapid growth of the accretionary prism resulted in termination of sandy siliciclastic input to the slope basin and an overall upward-thinning and upward-fining megasequence.

Based solely on the lithologic characteristics of Unit III, we are not able to locate a definitive boundary between lowermost trench-slope deposits and the uppermost accretionary prism. The preponderance of coarse-grained gravity-flow deposits, especially the gravel and pebbly mudstone from 340 to 347 mbsf, supports the notion of a relatively gentle seafloor gradient to promote deceleration and trigger deposition. The flat floor of the trench satisfies this notion better than a steeply inclined lower slope. On the other hand, some of the thin sand beds within the upper part of Unit III could have settled onto a sedimentary carapace several tens of meters above the uplifting prism as thicker turbidity currents moved across the trench floor and lapped onto the landward wall. To complicate the interpretation further, the slope to prism transition is not defined clearly by seismic reflection data. Thus, we suggest that the base of the trench-slope deposits is probably within the upper 20–40 m of Unit III.

X-Ray Diffraction Mineralogy

The results of X-ray diffraction (XRD) analysis of bulk-sediment samples from Site 1175 are shown in Figure **F8** (see Table **T4** for peak-intensity and peak-area data). Calcite is the only mineral to show significant changes in relative abundance with depth. Carbonate content increases downsection within the nannofossil-rich hemipelagic deposits of Unit I (average = 25%). The average contents of total clay minerals, quartz, and plagioclase within Unit I are 36%, 28%, and 11%, respectively. Similar averages occur within Unit II (Table **T5**). Below the uppermost part of Unit III, calcite content decreases sharply to relative percentages of <12% (average = 10%). This reduction of carbonate within the turbidite-rich facies is probably due to dilution of biogenic-pelagic input by terrigenous silt and clay, as well as to deposition closer to the calcite compensation depth. Average contents of quartz and plagioclase increase within Unit III to 35% and 16%, respectively.

XRD analysis of selected ash layers shows that the degree of alteration of volcanic glass is minimal. Common crystalline minerals within the ash beds include quartz, plagioclase, amphibole, and pyroxene (Table **T6**). There are also small amounts of pyrite, calcite (from nannofossils), and halite (an artifact from evaporation of pore water). In general, unambiguous recognition of cristobalite is precluded by interference from a relatively strong plagioclase peak.

F8. Abundances of total clay minerals, quartz, plagioclase, and calcite, p. 34.

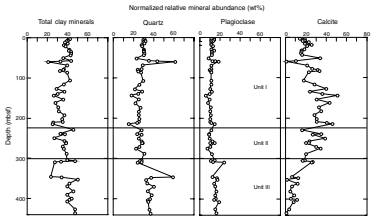

T4. Peak intensities and peak areas from XRD analysis of sediments, p. 70.

T5. Mineral abundances based on XRD analysis of bulk-sediment powders, p. 72.

T6. XRD analysis of bulk-powder volcanic ash, Hole 1175A, p. 74.

STRUCTURAL GEOLOGY

Site 1175, drilled into an actively tilting lower slope basin, exhibits little evidence for tectonic deformation at the core scale; however, there is copious soft-sediment slumping in lithostratigraphic Unit I, the upper slope–basin facies (Fig. F9), and minor faulting in Units II and III. Structural data are presented in Table T7. Overall, the upper 205 m is characterized by extensive soft-sediment slump folding and contortion, whereas the lower interval, from 205 to 445 mbsf, is dominated by subhorizontal bedding and minor faults, mostly steeply dipping and of normal sense. Near the base of the hole, core recovery was extremely poor, but a few pieces of recovered sandstone exhibiting web structure and small faults, as well as a short interval of steeper dips up to 21°, may be consistent with penetration into accreted trench sediments.

In the upper 204 mbsf, APC coring permitted geographic reorientation of well-preserved soft sediment structure with data from the Tensor orientation tool (see "Structural Geology," p. 6, in the "Explanatory Notes" chapter). Below this depth, extensive XCB biscuiting of the partially lithified sediments mostly precluded reorientation, although a few structures were reoriented with paleomagnetic declination data.

F9. Bedding dips relative to the core liner vs. depth, p. 35.

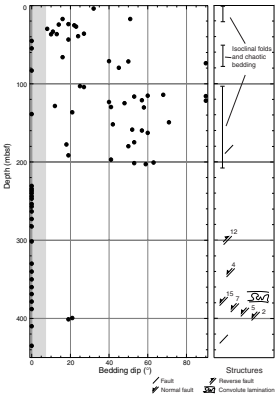

T7. Structural data, p. 75.

Slump Folding and Contorted Bedding

Starting only a few meters below seafloor in the first recovered core, slump features are well developed and common down to 204 mbsf. This slump-dominated interval coincides with lithostratigraphic Unit I. Large variations in bedding attitude, from horizontal to vertical, but only rarely clearly overturned, along with core-scale recumbent to isoclinal folds, chaotically mixed bedding, and rare boudins are the defining features of this interval. Fold amplitudes vary from a few centimeters, visible in the split cores, to several meters, inferred from downcore changes in bedding attitudes. True slump folding is distinguished from possible artificial core flow by the recovery of tight fold hinges with sharp and apparently undistorted intersections with the core margin (e.g., Fig. F10). Intervals from 0 to 20 mbsf, 54 to 83 mbsf, and 103 to 204 mbsf all exhibit disaggregated bedding and small folds marking slumped deposits. Interlayered with these strongly slumped zones are intervals from 20 to 54 and 83 to 103 mbsf that exhibit horizontal to gently inclined bedding.

F10. Example of a slump-fold hinge, p. 36.

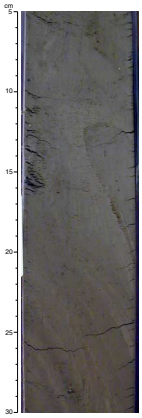

Bedding dips from 0 to 204 mbsf are markedly variable with depth (Fig. F9), but zones of horizontal beds unaffected by slumping are also apparent. Attitudes (reoriented to true azimuth with Tensor tool data) of bedding exhibit a great deal of scatter but very broadly define a north-south girdle of dip directions (Fig. F11A). Where possible, we measured fold axial planes and axes of small folds observed in the cores. These few axial planes strike northwest-southeast and dip to the south-southwest (Fig. F11B), and the fold axes have westward trends and shallow to moderate inclinations.

F11. Stereographic projections of poles to bedding and fold axial planes, p. 37.

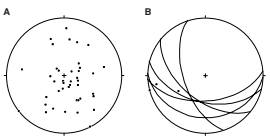

We interpret this zone of slumping as having formed in response to syndepositional tectonic tilting of the slope basin as its southeastern margin was uplifted by slip along the OOSTs imaged in three-dimensional (3-D) seismic reflection data (see "Seismic Stratigraphy," p. 24). The seismic data indicate that the fanning reflectors of the basin dip generally northward in this location. The axial-plane data suggest

northward vergence and, along with bedding, are consistent with downslope slumping toward the north.

Below 220 mbsf, bedding is much more consistently subhorizontal to gently inclined, with a few localized zones of chaotic bedding between 350 and 388 mbsf. It is possible that more extensive slumped sediments were also penetrated below 205 mbsf but were not recognized in the poorly recovered and badly biscuited XCB cores. Significant dips, up to 21°, were observed only in Core 190-1175A-43X at ~400 mbsf; however, core recovery from 400 mbsf to the total depth of 445 mbsf was only 4%, and little is known about this interval.

Beginning at ~298 mbsf, we observed a zone of small, steep faults of mostly normal and occasionally reverse sense, typically showing displacements of <1 mm to a few millimeters. These minor structures are present from 298 to 302 mbsf and sporadically from 340 to 435 mbsf and are similar to those observed at Sites 1173 and 1174. As at those sites, these faults do not exhibit strong preferred orientation (Fig. **F12**) and hence are interpreted as compaction-related features produced during sediment burial and dewatering, although they could also be extensional response to tilting and uplift of the basin.

In Core 190-1175A-44X at 406.9 mbsf, a several-centimeters-long interval in poorly lithified sand exhibits web structure (Fig. **F13**). At 425.8 mbsf, Core 190-1175A-46X recovered only one 2-cm-long piece of sandstone, which contains several low-angle small faults. Unfortunately, core recovery was too poor from 400 to 445 mbsf for us to meaningfully interpret the deformational environment in which these structures formed; the deformation observed is consistent with either deformed slope basin or frontally accreted trench sediments.

Uncalibrated Gas-Permeameter Measurements

Determinations made with the gas permeameter at Site 1175, again subject to the provisos outlined in **"Structural Geology,"** p. 6, in the "Explanatory Notes" chapter, illustrate the huge influence of lithology on gas permeability. The data are summarized in Figure **F14.** As at the other sites, the overall values center on the hemipelagic clays that dominate the section. Results range chiefly between 10^{-16} and 10^{-17} m², although the lowest part of the hole becomes siltier and yields slightly higher values.

A coarse, friable black ash at 23 mbsf gave an exceptionally high measurement (1.2×10^{-11} m²), and turbiditic sands between 60 and 90 mbsf also yielded large values ($>8 \times 10^{-12}$ m²). Thin bands of gray-white ash also gave relatively high determinations (~10^{-12} m²), in line with shallow, unaltered equivalents at the other sites.

BIOSTRATIGRAPHY

Sediments recovered from Site 1175 provide a continuous sedimentary record from the Quaternary (Subzone NN21b) to the Pliocene (NN18). Calcareous nannofossils were used for developing the biostratigraphic framework according to the zonation schemes of Gartner (1977) and Martini (1971) with zonal modifications proposed by Young (1998) (Table **T8**). The interval (core and section) and depth (mbsf) constraints of calcareous nannofossil events recognized at Site 1175 are listed in Table **T9.** For nannofossil ranges at Site 1175 see Table **T10.**

F12. Stereographic projections of the orientation of minor normal faults, p. 38.

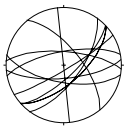

F13. Poorly lithified coarse sand exhibiting apparent web structure, p. 39.

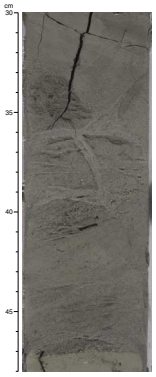

F14. Uncalibrated gas-permeameter results, p. 40.

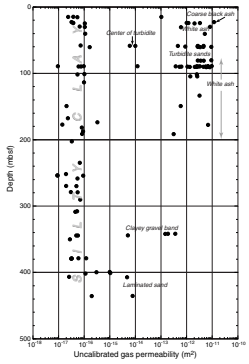

T8. Recognized nannofossil events, p. 78.

T9. Interval and depth constraints of calcareous nannofossil events, p. 79.

T10. Calcareous nannofossil range chart, p. 80.

Calcareous Nannofossils

Hole 1175A was cored to 435.7 mbsf, recovering late Quaternary (Subzone NN21b) to late Pliocene nannofossil assemblages (Zone NN18). Calcareous nannofossils are abundant throughout the sequence and generally well preserved. The upper 200 m of the section is presumed to represent slump deposits. This implies several constraints using nannofossil last and first occurrence datums for age determination. Reworked nannofossils could indicate an older age than their actual time of deposition. Folded sediment strata may also lead to inaccurate sedimentation rates.

Pleistocene

Sediments recovered from 7.11 to 385.84 mbsf (Samples 190-1175A-1H-CC to 41X-CC) yield Pleistocene nannofossil assemblages. Nannofossils are abundant in the Pleistocene and well preserved. Small placoliths such as *Emiliania huxleyi* and *Gephyrocapsa* spp. dominate the assemblage alongside numerous subordinate taxa present. Reworked Neogene taxa such as discoasterids, *Reticulofenestra pseudoumbilicus,* and *Sphenolithus* spp. were encountered frequently throughout the Pleistocene samples. Based on counts of 300 specimens per sample, the onset of the *E. huxleyi* acme Subzone NN21b (0.085 Ma) could be determined between Samples 190-1175A-3H-3, 75–76 cm, to 3H-CC. A further event to subdivide Subzone NN21a was the last occurrence of *Helicosphaera inversa* (0.14 Ma) between Samples 190-1175A-8H-CC and 9H-CC. The base of Subzone NN21a marked by the first occurrence of *E. huxleyi* (0.26 Ma) was observed between Samples 190-1175A-14H-CC and 15H-4, 75–76 cm. The Pleistocene assemblages older than 0.26 Ma are characterized by the dominance of gephyrocapsids. The interval from Samples 190-1175A-15H-4, 75–76 cm, to 20H-3, 78–79 cm, marked by the absence of both *E. huxleyi* and *Pseudoemiliania lacunosa,* was assigned to Zone NN20. The last occurrence of *P. lacunosa* (0.46 Ma) between Samples 190-1175B-20H-3, 78–79 cm, and 20H-CC defines the top of Zone NN19. The last occurrence of *Reticulofenestra asanoi* (0.8 Ma) between Samples 190-1175A-30X-3, 75–79 cm, and 30X-CC and its first occurrence (1.06 Ma) between Samples 190-1175A-32X-CC and 33X-4, 73–74 cm provide further datums to subdivide Zone NN19. Further analysis of relative abundances of the different *Gephyrocapsa* morphotypes may provide a more precise biostratigraphic resolution for Zone NN19.

Pliocene

Sediments cored from 390.25 to 435.69 mbsf (Samples 190-1175A-42X-2, 75–76 cm, to 47X-CC) are assigned a Pliocene age. The late Pliocene assemblages are dominated by reticulofenestrids and *Pseudoemiliania* spp. Nannofossils are well to moderately preserved and generally less abundant than in the Pleistocene sediments. The first occurrence of *Gephyrocapsa oceanica* (1.77 Ma) approximates the Pleistocene/Pliocene boundary. Common reworking of Pliocene species, mainly discoasterids and reticulofenestrids, makes the distinction of Zone NN18 difficult. The last occurrence of *Discoaster brouweri,* defining the top of Zone NN18, was observed between Samples 190-1175A-44X-CC and 46X-CC with fairly abundant and well-preserved *D. brouweri* specimens.

PALEOMAGNETISM

Introduction

Tensor tool orientations were successfully used to correct the magnetic declinations from 16.70 to 205.30 mbsf (Cores 190-1175A-3H through 22H). After measuring the natural remanent magnetization (NRM), all sections of the archive half of the core were partially demagnetized using AF magnetization at 30 mT at 5-cm intervals to remove magnetic overprints. Inclination data obtained after AF demagnetization provide useful information for interpreting late Pliocene to Pleistocene geomagnetic polarity reversals. However, identification of geomagnetic polarity intervals in the lower part of Hole 1175A was difficult because of poor core recovery.

To gain a better understanding of core disturbance caused by drilling, an experiment was conducted to compare the NRM of whole-round cores, working-half cores, and archive-half cores.

Paleomagnetic Results

The declinations of cores from 16.70 to 205.30 mbsf (Cores 190-1175A-3H through 22H) were corrected using Tensor tool orientation data. The gradual change in declination in the range from –90° to 90° reflects the secular variation of the geomagnetic field, although many short intervals with reversed polarity inclinations in this secular variation curve are considered to be possible short geomagnetic events (Fig. F15). Scattered declinations below 205.30 mbsf indicate that several pieces of core rotated individually during XCB coring.

The majority of NRM for all sections is strongly biased toward steep inclinations of ~60°–80°. These overprints were successfully removed by AF demagnetization at 30 mT. Stable positive inclinations were continuously observed from 0 to 298.8 mbsf (Fig. F15). However, short intervals of reversed polarity inclinations were identified. These reversed inclinations probably reflect geomagnetic excursions during this normal chron. This is especially true for the seven reversed polarity inclination peaks that correspond to declination peaks (Table T11). To distinguish between magnetic excursions and core disturbance, detailed postcruise investigations of these inclination anomalies and comparisons with other magnetic records are required.

Magnetic intensity shows slightly low values with some high-intensity peaks from 0 to 311.38 mbsf (Section 190-1175A-33X-CC, 30 cm). These high-intensity peaks closely correspond to high-susceptibility peaks measured with the multisensor track (MST) (see "Physical Properties," p. 21) and likely reflect the presence of magnetic minerals in sediments such as ash layers. Higher intensity was observed below 311.38 mbsf, although it is difficult to interpret intensity changes at this depth because of poor core recovery.

Magnetostratigraphy

Site 1175 magnetostratigraphy is based on polarity changes determined by measuring the inclination of the archive half of the core after AF demagnetization at 30 mT. A magnetic polarity change from normal to reversed at 298.80 mbsf (Section 190-1175A-32X-5, 80 cm) is interpreted as the Brunhes/Matuyama Chron boundary dated at 0.78 Ma (Cande and Kent, 1995) (Fig. F16). Seven short reversed polarity events

F15. Paleomagnetic declination, inclination, and intensity, p. 41.

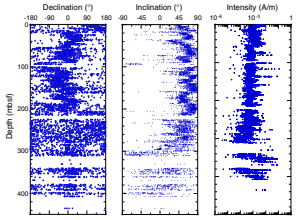

T11. Depths and ages of magnetic chrons, p. 82.

F16. Magnetostratigraphy, p. 42.

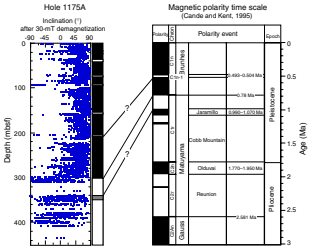

are also observed in the Brunhes Chron at 17.00 mbsf (Section 190-1175A-3H-1, 30 cm), 24.00 mbsf (Section 3H-5, 130 cm), 35.73 mbsf (Section 4H-CC, 5 cm), 73.00 mbsf (Section 8H-6, 130 cm), 92.75 mbsf (Section 11H-1, 5 cm), 158.00 mbsf (Section 18H-1, 20 cm), and 205.35 mbsf (Section 23X-1, 5 cm). These short intervals are thought to represent geomagnetic excursions. Based on previous studies, eight major excursions have been identified in this chron (Champion and Lanphere, 1988). However, identification of excursions is sometimes difficult because they are usually very short events. Furthermore, the possibility of core disturbance remains. In order to identify the excursions, comparison with paleomagnetic results from other locations must be made. The reversed polarity at 158.00 mbsf (Section 190-1175A-18H-1, 20 cm) may be an excursion corresponding to C1n-1 of Cande and Kent (1995).

The Matuyama Chron (0.780–2.581 Ma), characterized by a predominantly reversed polarity, is interpreted to extend from 298.80 mbsf to the bottom of the hole at 435.65 mbsf. In this reversed polarity chron, scattered intensity changes and poor core recovery make identification of short normal polarity geomagnetic events difficult. However, the nearly continuous normal polarity interval below 309.8 mbsf (Section 190-1175A-33X-6, 70 cm) within the Matuyama Chron is considered to be the Jaramillo Event (0.99–1.07 Ma).

Sedimentation Rate

Based on the depth and age of the Brunhes/Matuyama boundary, the sedimentation rate of lithostratigraphic Units I and II is estimated at 38.31 cm/k.y. (Fig. F17). The sedimentation rate within Units I and II corresponds closely to the biostratigraphic sedimentation rate curve (see "Biostratigraphy," p. 10). The age-depth point of the positive inclination zone (Jaramillo Event) within the Matuyama Chron also corresponds closely to the sedimentation curve estimated by biostratigraphic analysis. The sedimentation rate of Unit III could not be estimated using magnetostratigraphy because of poor core recovery.

F17. Age-depth plot, p. 43.

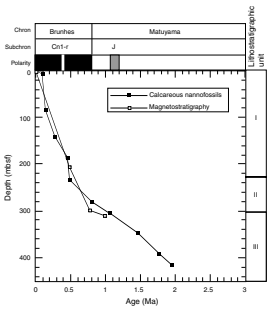

Magnetic Disturbance Experiment

To investigate the effect of core disturbance and the drilling-induced magnetic overprint during APC coring, we conducted an experiment to compare the magnetic remanence of whole- and half-core sections. Cores 190-1175A-3H, 7H, and 12H were selected to determine the influence of drilling, core cutting, and core splitting on magnetic measurements.

Procedure

Whole-round core NRM measurements were taken with the cryogenic magnetometer after susceptibility measurements using the MST. NRM measurements of the working half were taken just after splitting the core with a wire splitter. NRM and magnetic remanence after AF demagnetization at 30 mT were measured on the archive half of the core after lithostratigraphic observation and susceptibility measurements using the AMST (see "Physical Properties," p. 21).

Results

NRM declination directions of working and archive halves followed similar curves from the top to the bottom of Cores 190-1175A-3H, 7H, and 12H. In contrast, the NRM declination curves of working and archive halves do not correspond to the NRM declinations of whole-round cores (Fig. F18). In Core 190-1175A-3H, declinations from 16.75 mbsf (Section 3H-1, 5 cm) to ~19.50 mbsf (Section 3H-2, 130 cm) and from ~24.00 mbsf (Section 3H-5, 130 cm) to 26.1 mbsf (Section 3H-7, 40 cm) show rapid changes in the range from –180° to 180°. Inclinations of archive and working halves show similar curves as the whole-round cores. A gradual increase of inclinations from about –40° to ~85° was observed from 16.75 mbsf (Section 190-1175A-3H-1, 5 cm) to ~19.50 mbsf (Section 3H-2, 130 cm).

Archive-half declinations after 30-mT demagnetization followed a curve similar to the NRM declination curve of the whole-round cores, although scattered declinations were still observed from 16.75 mbsf (Section 190-1175A-3H-1, 5 cm) to ~19.50 mbsf (Section 3H-2, 130 cm) and from ~24.00 mbsf (Section 3H-5, 130 cm) to 26.1 mbsf (Section 3H-7, 40 cm). After demagnetization, the archive half showed a shallowing of inclinations from NRM inclination values of 90°–80° to 50°–60°. Rapid changes of inclination from –45° to 70° were also observed from 16.75 mbsf (Section 190-1175A-3H-1, 5 cm) to ~19.50 mbsf (Section 3H-2, 130 cm) and from ~24.00 mbsf (Section 3H-5, 130 cm) to 26.1 mbsf (Section 3H-7, 40 cm). The changes in inclination between the NRM of whole-round cores and the magnetic remanence of archive halves after AF demagnetization at 30 mT correspond to those in declination (Fig. F18).

Summary

Correspondence of working- and archive-half NRM suggests that sediments in the core have not undergone strong disturbance during APC drilling in this particular case. This is indicated by similar declination and inclination curves between the working and archive halves of the core (Fig. F18). Rapid declination changes in the top and bottom of the core, from 16.75 mbsf (Section 190-1175A-3H-1, 5 cm) to ~19.50 mbsf (Section 3H-2, 130 cm) and from ~24.00 mbsf (Section 3H-5, 130 cm) to 26.1 mbsf (Section 3H-7, 40 cm), indicate that the core top and bottom have probably undergone disturbance during moving on deck after drilling.

The difference in declination between whole-round and halved cores is considered to be secondary magnetic noise acquired during splitting into half sections. Similar NRM declinations between working and archive halves also suggest the sediments acquired a noisy magnetization during splitting.

After AF demagnetization, archive-half declinations correspond to whole-round NRM declinations (Fig. F19), indicating that the magnetic noise was successfully removed from the split half. Archive-half inclinations after AF demagnetization show shallowing from the steep NRM inclination of ~80°–90° to 50°–60°. This shallow inclination corresponds to the expected axial dipole field inclination of 52° at Site 1175. Inclination changes after demagnetization suggest that the magnetic noise acquired by half sections can be removed by weak AF demagnetization.

F18. Magnetic disturbance experiment, p. 44.

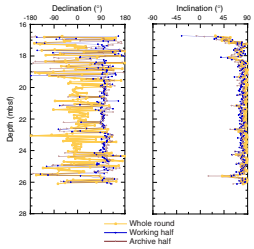

F19. Overprint removal experiment, p. 45.

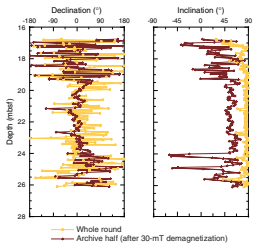

Two significant discoveries were made during this experiment: (1) core sediments were probably not disturbed strongly during APC drilling in this case and (2) the wire splitting method of cutting a whole-round core creates a magnetic overprint that can be removed by weak AF demagnetization.

INORGANIC GEOCHEMISTRY

Fifty-two interstitial water samples were squeezed from selected 10- to 50-cm-long whole-round samples for chemical and isotopic analyses at Site 1175. Sample depths ranged from 1.4 to 400.3 mbsf. Samples were collected from every section in Cores 190-1175A-1H and 2H, from four sections in Core 3H, from three sections in Core 4H, and from two sections in Core 5H. One sample per section was collected from the remainder of the site, except for Cores 190-1175A-24X, 34X, 35X, 36X, and 40X, because of poor recovery and/or the poor condition of these cores.

Elemental concentrations are reported in Table **T12** and plotted as a function of depth in Fig. **F20.** Eight major and minor dissolved anions and cations that sensitively reflect microbially mediated or inorganic water-rock (sediment and oceanic basement) reactions were determined for each sample. The former includes alkalinity and sulfate, and the latter are Cl, Ca, Mg, Na, K, and Si. Every second sample in the top 50 mbsf and every third sample in the remainder of the section were analyzed for ammonium. Salinity and pH were also determined.

The outstanding characteristics of the interstitial water concentration-depth profiles at Site 1175 are the intense microbially mediated reactions in the top ~200 m of the section. Only minor or no changes in chemical gradients occur throughout the section in the abiogenic components. Additionally, Cl concentration profiles can be potentially used to constrain the timing of sediment slumping events.

T12. Pore fluid compositions, Hole 1175A, p. 83.

F20. Pore fluid compositions as a function of depth, p. 46.

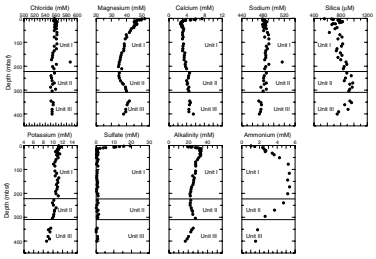

Geochemistry Controlled by Inorganic Reactions

Chloride

Cl concentrations were determined with a relative analytical uncertainty of 0.1% based on duplicate or triplicate titrations of all samples. Overall, Cl concentrations slightly decrease with depth from 562 to 551 mM and remain close to seawater concentrations. This is in contrast to most oceanic sites and Sites 1173 and 1174, where Cl decreases more rapidly with depth in the shallower part of the section (by ~3.2%) as a result of the diffusion of low-chlorinity interglacial seawater downward into the section. The lack of a shallow gradient at Site 1175 is interpreted to imply that sediment slumping has actively transported interglacial seawater into the section. It also implies that this slumping has occurred in the time interval since seawater has freshened as a result of glacial melting, approximately the last 10 k.y.

Additionally, in the top 100 mbsf and between 270 and 300 mbsf, there are small-scale fluctuations, on the order of 1–3 mM, over 10 m. Again, these fluctuations are most likely caused by the slumping of sediments that have pore fluids with Cl concentrations that reflect glacial and interglacial ocean chlorinities.

Sodium

Na concentrations are relatively constant, having small-scale fluctuations similar to chloride. Concentrations increase by ~2% between the shallowest samples and ~100 mbsf. This increase is mostly caused by Na release from clay as a result of ion exchange with ammonium. Concentrations then decrease with depth to 3% lower at 400 mbsf. This decrease is partially due to the decreasing ammonium concentrations and the net uptake of sodium into clay ion exchange sites, as well as to diffusion to greater depths where temperatures are higher and silicate reactions more intense.

Potassium

K concentrations decrease smoothly from 11.2 mM, which is slightly greater than the seawater concentrations (10.4 mM), through a small maximum of 11.5 mM at ~5 mbsf to 8.69 mM at the bottom of the section. The decrease is most pronounced in Unit III. The profile suggests diffusion into a silicate reaction zone at greater depth, located below the drilled section. The higher than seawater concentrations in the upper part of the section are mostly caused by the expulsion of K from clay minerals as a result of ion exchange by ammonium.

Silica

Dissolved Si concentrations increase from ~550 uM close to the sediment-seawater interface to ~1,000 uM at 300 mbsf. At the base of Unit II, the gradient reverses, and similar to K, Si concentrations decrease nearly linearly with depth to ~600 uM, suggesting a silicate reaction zone at greater depth, most likely the same phase(s) that control the uptake of K from the pore fluids. Diatom dissolution is the most likely candidate for the increase in Si concentrations with depth; the solubility of opal-A increases with temperature and thus with depth. The solubility of opal-A at 20°C is ~1000 µM. Diatoms are present throughout the section and diminish in abundance with depth (see **"Biostratigraphy,"** p. 10). The small-scale fluctuations in Si concentrations at all depths at this site reflect the great sensitivity of dissolved Si to local variations in lithology.

Magnesium and Calcium

Both Mg and Ca concentrations decrease rapidly with depth in the top 15–20 m of the section. Ca reaches its lowest concentration of 3.15 mM and Mg has a local minimum of 45.7 mM. These two minima coincide with the depth of an alkalinity minimum. Below the depth of this shallow Mg minimum, concentrations decrease to ~250 mbsf. These data suggest that in the upper 20 mbsf, authigenic dolomite is precipitating and both Mg and Ca are consumed from solution. Below this zone, dolomite formation proceeds as a result of dolomitization of preexisting calcite. This is evidenced by the inverse gradient of Mg and Ca; Mg is removed from the pore fluids, whereas Ca is added. In this section, abundant biogenic calcite is available for dolomitization. Calcite ranges from ~3 to >30 wt% (see **"Organic Geochemistry,"** p. 18). Deeper in Unit II, almost no change in Mg and Ca concentrations is observed. In Unit III, however, Mg concentrations decrease with depth but Ca concentrations remain constant, indicating that these cations are no

longer involved in carbonate diagenesis and that Mg is involved in silicate reactions at greater depth. The sink for Mg seems to be the same as for K and Si and probably Na, implying that a K-Mg silicate (±Na) is forming at greater depth. The alkalinity profile discussed below indicates that alkalinity is also consumed by the deeper reaction.

Geochemistry Controlled by Microbially Mediated Reactions

Sulfate

Sulfate concentrations rapidly decrease with depth and reach zero at ~15 mbsf. This sulfate reduction zone is present at 2.5 times greater depth than at Site 1173 and 3 times deeper than at Site 1174. Because the sulfate reduction zone was sampled at high resolution, it is possible to quantify the rate of sulfate reduction as a function of depth. Preliminary analysis, based on the curvature of the sulfate vs. depth profile, indicates that sulfate reduction rates decrease linearly with depth.

Ammonium

A broad ammonium maximum of ~5 mM is found between ~75 and 200 mbsf. The magnitude of the concentration maximum is similar to Site 1173 but spans an interval that is approximately five times larger. In contrast, maximum concentrations are about one-half of those at Site 1174 and, again, the interval is broader. Ammonium is produced during the microbially mediated decomposition of organic matter. At such high concentrations, ammonium occupies clay ion exchange sites, expelling mostly K and Mg and some Na into the pore fluid. As at Sites 1173 and 1174, the existence of a midsection maximum implies a deep sink for ammonium. However, no chemical or biochemical mechanism has been identified yet.

Alkalinity

Alkalinity increases rapidly and reaches a maximum of 33.1 mM at ~15 mbsf, where sulfate concentrations reach zero. This is expected because alkalinity is produced during sulfate reduction. The depth of the maximum coincides with the depth of Mg and Ca minima, driving authigenic carbonate formation. At greater depths, alkalinity decreases monotonically but remains high (~20 mM). The almost-constant concentration between ~100 and ~300 mbsf may be the equilibrium concentration for dolomitization of calcite at the low temperatures (<~22°C) at this site. Shore-based calculations will test this hypothesis. The reversal and decrease in alkalinity below ~300 mbsf (see **"Magnesium and Calcium,"** p. 16) suggests a hydrous K-Mg silicate forming at greater depth.

Summary

In summary, pore fluid chemical compositions at this site are less altered from seawater than at Sites 1173 and 1174. Four processes are principally responsible for the observed concentration variations: (1) opal-A and diatom dissolution, (2) carbonate diagenesis, primarily two dolomitization reactions, (3) silicate reaction at depths greater than the section drilled, and (4) microbially mediated reactions. In particular,

carbonate diagenesis is expected to influence the physical properties, such as porosity and grain density. Unlike at Sites 1173 and 1174, where ash alteration dominated the chemistry of the pore fluids, the volcanic ash layers at this site are unaltered and do not affect the chemistry of the pore fluids because of the much lower geothermal gradient of 54°C/km (see "Physical Properties," p. 21). Even the prominent ash layer at ~100 mbsf, clearly recognized in all physical properties data, does not affect the pore fluid chemistry. Lastly, a unique feature of this site compared to Sites 1173 and 1174 is the lack of a shallow chloride gradient, which implies that slumping has occurred in approximately the last 10 k.y.

ORGANIC GEOCHEMISTRY

As part of the routine geochemical analyses, monitoring of volatile hydrocarbons was conducted for safety considerations, and some organic, petrological, and geochemical studies were carried out to obtain additional information about the sources and formation mechanisms for the organic matter and hydrocarbons observed in the sediments at Site 1175.

At Site 1175, 44 sediment samples were collected at ~10-m intervals from 5.0 to 406.5 mbsf. Sediments were analyzed for methane concentrations and light hydrocarbon compositions during headspace analyses (Fig. **F21A;** Table **T13**) (see "Organic Geochemistry," p. 14, in the "Explanatory Notes" chapter for analytical procedures). In addition, inorganic carbon (carbonate), TOC, N, S, and H analyses were performed (Fig. **F21B;** Table **T14**).

In general, the sediments from Hole 1175A have low inorganic carbon values (0.11–4.59 wt%; average = 2.10 wt%) and carbonate concentrations up to 40 wt%. The very young age of the sediments (late Pliocene; ~2 Ma) and low temperatures encountered in Hole 1175A are responsible for the immature organic matter and low production of hydrocarbons observed at this site. The highest carbonate concentrations are found between 120 and 280 mbsf (~10%–40%) followed by a gradual decrease to <1 wt% at ~440 mbsf, the base of the hole (Fig. **F21B**). The high methane concentrations and weight percent carbonate profiles correlate between 100 and 300 mbsf, and both gradually decrease with depth to the bottom of the hole.

Hydrocarbon Gases

Headspace gas concentrations of methane through the first 11.7 mbsf in the sulfate reduction zone are low (2.1–4.3 ppm) (Fig. **F21**), increase sharply in concentration just below this interval at 18.2 mbsf (6018–558,612 ppm), and remain high through 307 mbsf. Methane concentrations decline over the remaining 99 m of depth, ranging from 3785 to 10.7 ppm near the bottom of the hole. Only trace amounts of ethane (0.5–2 ppm) were detected in a few samples, indicating that the sediments encountered at Hole 1175A are highly immature and that little, if any, generation of hydrocarbons can be attributed to thermal maturation processes. Thus, all of the methane throughout Hole 1175A sediments is bacterial in origin (Claypool and Kvenvolden, 1983).

F21. Molecular compositions and concentrations of headspace gases, p. 47.

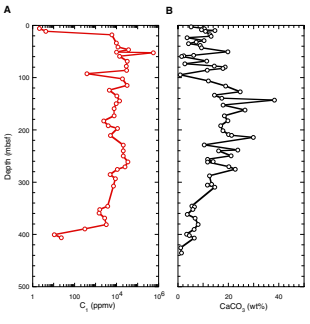

T13. Headspace and vacutainer gas analyses, Hole 1173A, p. 84.

T14. Carbon, nitrogen, sulfur, and hydrogen analyses, Hole 1173A, p. 85.

Conclusions

Organic geochemical analyses at Site 1175 lead to the following conclusions:

1. The sediments from Hole 1175A contain low inorganic carbon (~0.11–4.59 wt%) and carbonate contents up to 40 wt%, resulting in very immature organic matter and low hydrocarbon abundances.
2. The low methane concentrations in sediments below the sulfate reduction zone (~4.5 mbsf) and throughout Hole 1175A and high C_1/C_2 ratios are consistent with a bacterial origin.

MICROBIOLOGY

Eighteen samples for microbiological analysis were obtained from Hole 1175A for direct microscopic enumeration on board ship. Seventeen whole-round cores were taken for shipboard enrichment cultures, cell viability, and shore-based microbiological analysis to measure potential bacterial activities, culture microorganisms, characterize nucleic acids, and investigate fatty acid biomarkers.

Total Bacterial Enumeration

Bacteria are present in all 18 samples (Table **T15;** Fig. **F22**). The near-surface sample (Sample 190-1175A-1H-1, 116–117 cm) contains 6.97 × 10^7 cells/cm³, which follows a general trend observed at other Ocean Drilling Program (ODP) sites where near-surface bacterial populations decrease as overlying water depths increase (Table **T16**), although in this instance, the population is slightly smaller than expected.

The deepest sample is 399.99 mbsf (Sample 190-1175A-43X-2, 89–90 cm) with 3.59 × 10^5 cells/cm³, representing 0.5% of the near-surface population. Bacterial populations decline rapidly from the near surface, consistent with the decrease in sulfate concentrations (see **"Inorganic Geochemistry,"** p. 15), and then increase below 14.6 mbsf, consistent with increases in methane concentrations (see **"Organic Geochemistry,"** p. 18). The sample at 50.8 mbsf (Sample 190-1175A-6H-4, 112–113 cm) is notable in that it contains 7.28 × 10^7 cells/cm³ (i.e., slightly more bacteria than the near-surface sample). This is followed immediately with almost the lowest population enumerated of 3.71 × 10^5 cells/cm³ at 59 mbsf (Sample 190-1175A-7H-3, 134–135 cm).

The depth distribution of total bacterial numbers in sediments from Site 1175, apart from at the two depths noted in the above paragraph, conforms unusually well to the general model for bacterial populations in deep-sea sediments (Parkes et al., 1994) from the surface to 400 mbsf (Fig. **F22**). The unexpected uniformity of bacterial populations between 78 and 299 mbsf (Samples 190-1175A-9H-3, 134–135 cm, to 32X-5, 121–122 cm) may be due to lithostratigraphic factors, as there was significant chaotic stratification to ~220 mbsf and many turbidites between 220 and 300 mbsf (see **"Lithostratigraphy,"** p. 4). Uniform bacterial populations with depth, such as here, have been observed in the Amazon Fan (Cragg et al., 1997) where massive turbidites were cored (Flood, Piper, Klaus, et al., 1995).

There is a strong positive correlation between bacterial population size and methane concentration (R^2 = 0.68; *N* = 15; P = <0.005) on data

T15. Total bacterial populations in sediments, p. 86.

F22. Depth distribution of total bacterial populations in sediment samples, p. 48.

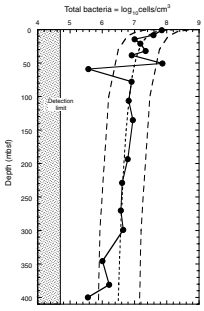

T16. Comparison of near-surface sediment bacterial populations at Site 1175 with data from nine other ODP sites, p. 87.

below the sulfate-reduction zone (below 14.5 mbsf). However, as the data for both bacterial numbers and methane concentration vary little with depth (Fig. F23), this correlation may not be particularly valid. Nevertheless, there are two pertinent observations of this relationship: (1) the two anomalous bacterial data in the upper part of the core at 50.8 and 59 mbsf (Samples 190-1175A-6H-4, 112–113 cm, and 7H-3, 134–135 cm) exactly match the maximum observed methane concentration and a low concentration trough, respectively, and (2) below 300 mbsf, both bacterial populations and methane concentrations decrease together.

F23. Depth profiles of total bacteria and methane concentrations, p. 49.

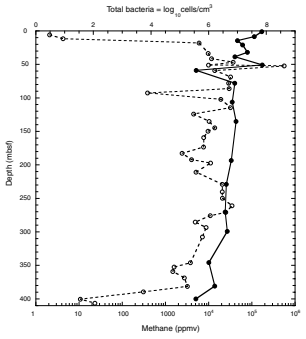

Contamination Tests

Tracer tests were conducted while coring with APC (Cores 190-1175A-5H and 6H) at this site. In order to estimate the amount of drilling fluid intrusion into the recovered cores, chemical and particulate tracers were deployed as previously described (Smith et al., 2000).

Chemical Tracer

Perfluoro(methylcyclohexane) was used as the perfluorocarbon tracer (PFT). Calibration of the gas chromatograph (HP 5890) with standard solutions yielded a slope of 9.2×10^{11} area units/gram of PFT. The detection limit for these samples is equivalent to 0.01 µL of drilling fluid. The tracer was detected on the outer edge of four of the six sections of core examined (Table T17). The PFT concentration in water collected on the catwalk from the top of the Core 190-1175A-6H was ~17 µg/L, confirming the delivery of the tracer to the drill bit. This value is 17-fold higher than the target concentration of 1 µg/L, possibly because of a mismatch between the tracer injection rate and the mud pump rate. The low concentration of the tracer in the samples from the outer edge of the core, despite the high concentration of PFT in the drill string, demonstrates that very little drilling fluid is entrained with the core liner when the APC is fired into the formation. Estimates of drilling fluid intrusion into the interior of the cores range from below detection to 0.02 µL/g (Table T18).

T17. Drilling fluid intrusion estimates based on PFT experiments, p. 88.

PFT content of aliquots of interstitial water collected in the chemistry laboratory from Sections 190-1175A-5H-2, 5H-5, and 6H-4 were all below the detection limit.

T18. Fluorescent microsphere tracer experiments, p. 89.

Particulate Tracer

Fluorescent microspheres were detected on the outside of four of the six sections examined in Core 190-1175A-5H (Table T18). Interestingly, no microspheres were observed in the first section of either core. This was observed in previous cores and suggests that the bag containing the microspheres may not rupture immediately as the core enters the liner. Microspheres were observed in samples collected midway between the core liner and the center of the core in Sections 190-1175A-5H-1 and 6H-3, which is consistent with the PFT data (Table T17). No microspheres were observed in the samples taken from the center of the cores examined at Site 1175.

PHYSICAL PROPERTIES

Introduction

At Site 1175, laboratory measurements were made to provide a downhole profile of physical properties within a basin located immediately upslope from an active OOST fault. With the exception of short sections (<50 cm), all cores were initially passed through the MST before being split. Gamma-ray attentuation (GRA) and magnetic susceptibility measurements were taken at 4-cm intervals with 2-s acquisition times for all cores. *P*-wave velocity logger (PWL) measurements were taken at 4-cm intervals with 2-s acquisition times for APC cores. No PWL measurements were taken on XCB cores. Natural gamma ray (NGR) was counted every 20 cm for 20-s intervals. Voids and cracking caused by gas expansion degraded MST measurements and were noted in cores between 14 and 200 mbsf. Biscuiting in XCB cores also degraded measurements.

Moisture and density samples were selected from undisturbed core at regularly spaced intervals of one per section. Measurements of dry volume and wet and dry mass were uploaded to the Janus database and were used to calculate water content, bulk density, grain density, porosity, void ratio, and dry bulk density. *P*-wave velocities were measured on split cores or discrete samples at a frequency of two to three per core. Measurements were taken in three directions when core conditions permitted.

Shear strength measurements were made near the *P*-wave core measurement locations from the mudline to 205 mbsf, at which point XCB coring began and the cores became too stiff for insertion of the vane shear device. Resistivity measurements were taken at least once per core. Raw data and calculated physical properties data are available from the Janus database for all MST, moisture and density, thermal conductivity, velocity, and shear strength measurements (see the **"Related Leg Data"** contents list). Because electrical conductivity data are not currently available from the database, they are included in Tables **T19** and **T20.**

T19. Formation factor obtained by the needle-probe method, p. 90.

T20. Electrical conductivity and formation factor for sample cubes, p. 91.

Density and Porosity

Sediment bulk density was determined by both the GRA method on unsplit cores and the mass/volume ("index properties") method on discrete samples (see **"Physical Properties,"** p. 19, in the "Explanatory Notes" chapter). The GRA density data and the bulk densities determined by the mass/volume method are generally in good agreement for APC cores (Fig. **F24A, F24B**). Below ~205 mbsf, the small diameter of XCB cores results in GRA bulk densities that are, on average, 0.1–0.2 g/cm³ lower than those determined from discrete samples. Both moisture and density measurements on discrete samples and GRA density measurements show similar downhole trends. Between the mudline and 100 mbsf, intervals of increasing and decreasing bulk density probably reflect lithologic variations.

Grain densities determined from dry mass and volume measurements are essentially constant downhole, with a mean value of 2.69 g/cm³ (Fig. **F24C**). Porosity decreases gradually with depth, from ~62%–70% at the mudline to 53%–60% at 225 mbsf. Between 225 and 435 mbsf, porosity decreases with depth more rapidly than in the upper 225

F24. Bulk density, grain density, and porosity, p. 50.

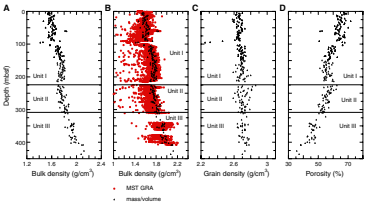

m to values of 38%–47% by 400 mbsf. The change in the porosity-depth gradient at 225 mbsf correlates with the lithostratigraphic boundary between the upper slope–basin facies at 224.75 mbsf (see "Lithostratigraphy," p. 4). There is no clear change in porosity, bulk density, or grain density at 301 mbsf, the boundary between the middle and lower slope–basin facies.

Shear Strength

Undrained shear strength measurements were made using a miniature automated vane shear (AVS) and were conducted exclusively in fine-grained silty clays. Shear strengths increase gradually downhole from <15 kPa at the seafloor to values approaching ~100 kPa at 205 mbsf (Fig. F25). Scatter in the data increases below ~145 mbsf as a result of fracturing of sediment and opening of fractures at the tips of the AVS vanes during some measurements. For this reason, actual sediment strength is probably best reflected by the highest measured values.

F25. Undrained peak shear strength, p. 51.

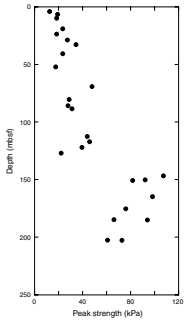

Thermal Conductivity and Projected Temperatures

Thermal conductivity was measured using one of two methods depending on core condition. For shallow, nonindurated samples, a needle probe was inserted into the unsplit core for a full-space conductivity measurement. For two samples from below 390 mbsf, insertion of the needle caused fracturing, so a half-space method was used on split cores. Because of poor core recovery and condition, no measurements were made below 397 mbsf. Thermal conductivities range from 0.67 to 1.51 W/(m·°C). (Fig. F26A). Between the mudline and ~300 mbsf, thermal conductivities remain near 1.0 W/(m·°C), ranging from 0.67 to 1.18 W/(m·°C) with no distinct trend. Apparent low thermal conductivities and scatter between 50 and 100 mbsf may be caused by gas expansion in the cores. Thermal conductivities increase below ~300 mbsf to a maximum of ~1.5 W/(m·°C) at 397 mbsf. Measurements are sparse below 350 mbsf.

A conductive heat flow of ~54 mW/m² was defined by shipboard thermal conductivities and downhole temperature measurements to 273 mbsf (see "In Situ Temperature and Pressure Measurements," p. 24). Using this estimated heat flow and measured shipboard thermal conductivities, projected downhole temperatures reach ~22°C at 400 mbsf (Fig. F26B).

F26. Thermal conductivity and temperature trends, p. 52.

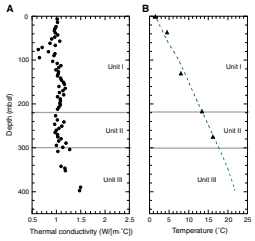

Acoustic Velocity

In APC cores, *P*-wave velocities were measured using the *P*-wave sensors 1 and 2 (PWS1 and PWS2) insertion probe system along the core axis (z-axis) and across the core axis (y-axis), respectively. The PWS3 contact probe system was used to measure *P*-wave velocities across the core liner (x-axis) (Fig. F27A). In XCB cores, sample cubes were cut and measurements in all three directions were performed using the PWS3 contact probe system. Acoustic impedance was computed as the product of bulk density and velocity along the z-axis. Bulk densities were obtained from moisture and density samples, and values were used only when acquired within 20 cm of *P*-wave velocity measurements. When cubes were cut, moisture and density samples were generally taken adjacent to *P*-wave velocity samples.

F27. *P*-wave velocity and impedance, p. 53.

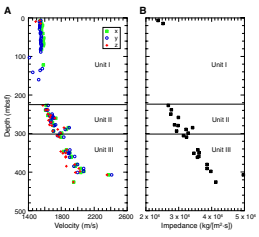

As at previous sites, few velocity measurements could be obtained along the axis of APC cores because of expansion cracks. Measurements along the x- and y-axes of APC cores cluster around 1550 m/s between the mudline and 90 mbsf (Fig. F27A). Attenuation was high along the x- and y-axes below 90 mbsf, and no reliable measurements could be obtained in the lower part of Unit I. Velocities measured on sample cubes in Units II and III follow a nearly constant velocity-depth gradient from 1600 m/s at 225 mbsf to ~2000 m/s at 400 mbsf. Two excursions from this constant gradient are observed at 285 mbsf and below 400 mbsf, respectively. The upper excursion corresponds to the first sandy layers that were sufficiently lithified to be cut with the saw. These layers also have a high acoustic impedance (Fig. F27B). The lower excursion is represented by only one data point and probably reflects the heterogeneity of the sediment in the lower part of Hole 1175A, where recovery was poor.

Electrical Conductivity

Measurements were made on APC cores with a four-needle 30-kHz frequency electrode array. On XCB cores, conductivity was measured on the same sample cubes used for *P*-wave measurements with a two-electrode 30-kHz frequency system.

Electrical conductivity and formation factor (see "Physical Properties," p. 19, in the "Explanatory Notes" chapter) measured on sample cubes are given in Table T20. For needle-probe measurements, only the apparent formation factor is given. As at other sites, the formation factor roughly follows the changes in porosity with depth. However, there is no marked discontinuity in the formation factor profile (Fig. F28); notably, the decrease in porosity below the thick ash layers at ~100 mbsf is not reflected clearly in the formation factor trend. The higher measurement scatter between 50 and 70 mbsf may be caused by sediment heterogeneity as it coincides with the presence of turbidites and thin ash layers. However, the scatter observed between 140 and 160 mbsf is probably an artifact as it corresponds to a zone where cores were affected by cracks. These cracks are preferentially oriented along the x-y plane and may contribute to the higher formation factor measured along the core with the needle probe. In Units II and III, the formation factor increases steadily with depth from an average of 4.5 at 225 mbsf to ~7 at 400 mbsf. The sediment displays only weak bedding-parallel parting but develops some anisotropy with burial. The vertical anisotropy averages <20% at the bottom of Hole 1175A.

Magnetic Susceptibility

Site 1175 volumetric magnetic susceptibilities were measured on unsplit cores by the MST (Fig. F29). Uncorrected values of magnetic susceptibility from the Janus database were used. Magnetic susceptibility values show no obvious downhole trend and generally fall between 10 and 50 × 10^{-5} SI. Several peaks of magnetic susceptibility have values as high as 300 × 10^{-5} SI. Magnetic susceptibility data increase slightly from 10 – 50 × 10^{-5} SI at 340 mbsf to 50 – 100 × 10^{-5} SI at 420 mbsf.

Natural Gamma Ray

NGR results are presented in counts per second (cps) (Fig. F30). The background scatter, produced by Compton scattering, photoelectric ab-

F28. Formation factor, p. 54.

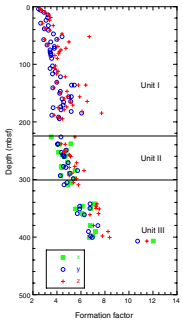

F29. Magnetic susceptibility, p. 55.

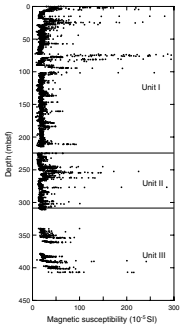

F30. Natural gamma ray, p. 56.

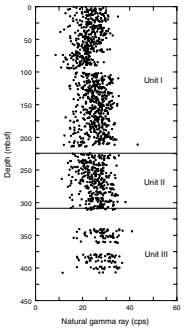

sorption, and pair production, was measured at the beginning (6.39 cps) and subtracted from the measured gamma-ray values. In general, NGR counts are low and are consequently likely to be affected by the short counting interval and by porosity variations. Overall, NGR data show considerable scatter between 15 and 40 cps. A slight decrease in NGR values is observed at 100 and 220 mbsf.

Summary and Discussion

Porosities within the upper slope–basin facies (Unit I) are characterized by high variability and decrease slightly with depth from 62%–70% at the mudline to 61%–68% at ~100 mbsf. This porosity profile may reflect a combination of the rapid deposition and disrupted nature of sediments deposited by slope-failure processes (see **"Lithostratigraphy,"** p. 4). Porosity decreases abruptly at ~100 mbsf to values of 57%–61% and then decreases gradually to 220 mbsf at the depth of the transition between the upper and middle slope–basin facies (Unit I/II boundary). Below 220 mbsf (within the middle and lower slope–basin facies), porosity decreases more rapidly with depth than in the upper slope–basin facies, reaching values of 38%–47% by 400 mbsf. The rapid decrease in porosity below 220 mbsf coincides with increasing *P*-wave velocity. There is no clear change in porosity, bulk density, or grain density at the depth of the middle slope–basin/lower slope–basin facies boundary (301 mbsf, Unit II/III boundary). A spike of high velocity and impedance values 20 m above this transition may correspond to a seismic reflector. The depth of this spike coincides with the depth of the upper unconformity on the depth-converted seismic profile.

IN SITU TEMPERATURE AND PRESSURE MEASUREMENTS

Four reliable determinations of downhole temperatures were made at Site 1175 using the Adara APC temperature tool and the Davis-Villinger temperature probe (DVTP). Table **T21** summarizes the deployments, and the temperature data are shown in Figures **F31** and **F32.**

In situ temperatures were estimated by extrapolation of the station data to correct for the frictional heating on penetration using an average thermal conductivity of 1.0 W/(m·°C). The estimated in situ temperatures from the mudline temperature and the four measurements define a linear gradient of 0.054°C/m in the upper 273.9 m (Fig. **F33**). For thermal conductivites of 1.0 W/(m·°C), vertical conductive heat flow at Hole 1175A would be 54 mW/m². Assuming purely vertical conductive and steady state heat flow, we project in situ temperatures of ~22°C for 400 mbsf, based on laboratory measurements of thermal conductivity (see **"Physical Properties,"** p. 21).

Pressures were also recorded during the DVTP-P deployments (Fig. **F34**). As noted in **"In Situ Temperature and Pressure Measurements,"** p. 26, in the "Explanatory Notes" chapter, postcruise modeling and processing is required to estimate in situ pressures.

SEISMIC STRATIGRAPHY

Reflections on 3-D seismic line 281 can be correlated with lithostratigraphic boundaries at Site 1175 (Fig. **F35**). Specific correlations should

T21. Summary of temperature measurements, p. 92.

F31. Temperatures measured with the Adara APC temperature tool, p. 57.

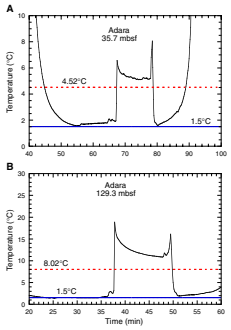

F32. Temperatures measured during the DVTP stations, p. 58.

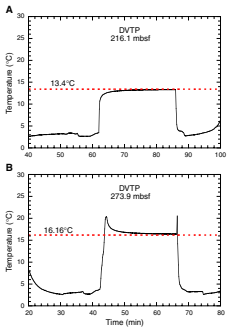

F33. Hole 1175A temperatures, p. 59.

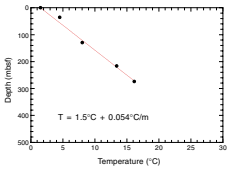

F34. Pressures measured during the DVTP-P stations, p. 60.

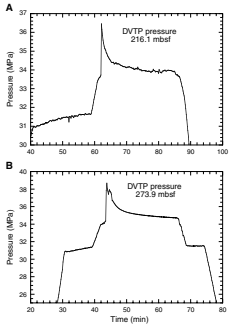

be considered preliminary at this time because the velocity structure at this site is not well known. Any inaccuracies in velocity will produce errors in depth conversion. Additional velocity work will be carried out postcruise to improve depth conversions and stratigraphic correlations.

Lithostratigraphic Unit I is recognized on the seismic line as a sequence bounded at the top by the seafloor and at the bottom by an angular unconformity (Fig. F35). Dips within the sequence increase from horizontal at the seafloor to 8°–10° at its base. The upper ~40 m of the sequence around Site 1175 has a somewhat irregular and discontinuous character that correlates with the slump deposits in the drill hole. The strong negative reflection at ~75 mbsf is likely to be caused by a major coarse ash bed encountered at ~90 mbsf in Hole 1175A, indicating that the depth conversion velocities may be ~10% too high in the shallow section.

Lithostratigraphic Unit II is interpreted to be the seismic stratigraphic unit that is onlapped by Unit I at its top and onlaps the underlying unit at its base. The shape of the unit is a northwest-thickening wedge that has relatively continuous and high-amplitude internal reflections.

The lowest identified seismic stratigraphic unit correlates with lithostratigraphic Unit III. It is defined by an angular unconformity at its top; the base of the unit is unclear, but it may be <100 m thick.

F35. Three-dimensional seismic reflection line 281, p. 61.

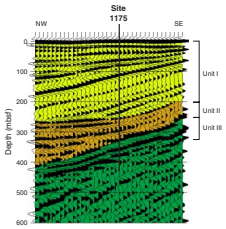

REFERENCES

Cande, S.C., and Kent, D.V., 1995. Revised calibration of the geomagnetic polarity timescale for the Late Cretaceous and Cenozoic. *J. Geophys. Res.,* 100:6093–6095.

Champion, D.E., Lanphere, M.A., and Kuntz, M.A., 1988. Evidence for a new geomagnetic reversal from lava flows in Idaho: discussion of short polarity reversals in the Brunhes and Late Matuyama polarity chrons. *J. Geophys. Res.,* 93:11667–11681.

Claypool, G.E., and Kvenvolden, K.A., 1983. Methane and other hydrocarbon gases in marine sediment. *Annu. Rev. Earth Planet. Sci.,* 11:299–327.

Cragg, B.A., Law, K.M., Cramp, A., and Parkes, R.J., 1997. Bacterial profiles in Amazon Fan sediments, Sites 934, 940. *In* Flood, R.D., Piper, D.J.W., Klaus, A.(Eds.), *Proc. ODP, Sci. Results,* 155: College Station, TX (Ocean Drilling Program), 565–571.

Flood, R.D., Piper, D.J.W., Klaus, A., et al., 1995. *Proc. ODP, Init. Repts.,* 155: College Station, TX (Ocean Drilling Program).

Gartner, S., 1977. Calcareous nannofossil biostratigraphy and revised zonation of the Pleistocene. *Mar. Micropaleontol.,* 2:1–25.

Martini, E., 1971. Standard Tertiary and Quaternary calcareous nannoplankton zonation. *In* Farinacci, A. (Ed.), *Proc. 2nd Int. Conf. Planktonic Microfossils Roma:* Rome (Ed. Tecnosci.), 2:739–785.

Martinsen, O., 1994. Mass movement. *In* Maltman, A. (Ed.), *The Geological Deformation of Sediments:* New York (Chapman and Hall), 127–165.

Moore, G.F., and Karig, D.E., 1976. Development of sedimentary basins on the lower trench slope. *Geology,* 4:501–504.

Parkes, R.J., Cragg, B.A., Bale, S.J., Getliff, J.M., Goodman, K., Rochelle, P.A., Fry, J.C., Weightman, A.J., and Harvey, S.M., 1994. A deep bacterial biosphere in Pacific Ocean sediments. *Nature,* 371:410–413.

Scholl, D.W., von Huene, R., Vallier, T.L., and Howell, D.G., 1980. Sedimentary masses and concepts about tectonic processes at underthrust ocean margins. *Geology,* 8:564–568.

Smith, D.C., Spivack, A.J., Fisk, M.R., Haveman, S.A., Staudigel, H., and ODP Leg 185 Scientific Party, 2000. Methods for quantifying potential microbial contamination during deep ocean coring. *ODP Tech. Note,* 28 [Online]. Available from World Wide Web: <http://www-odp.tamu.edu/publications/tnotes/tn28/INDEX.HTM>.

Taira, A., and Ashi, J., 1993. Sedimentary facies evolution of the Nankai forearc and its implications for the growth of the Shimanto accretionary prism. *In* Hill, I.A., Taira, A., Firth, J.V., et al., *Proc. ODP, Sci. Results,* 131: College Station, TX (Ocean Drilling Program), 331–341.

Underwood, M.B., and Bachman, S.G., 1982. Sedimentary facies associations within subduction complexes. *In* Leggett, J.K. (Ed.), *Trench-Forearc Geology: Sedimentation and Tectonics on Modern and Ancient Active Plate Margins*. Geol. Soc. Spec. Publ. London, 10:537–550.

Underwood, M.B., and Karig, D.E., 1980. Role of submarine canyons in trench and trench-slope sedimentation. *Geology,* 8:432–436.

Underwood, M.B., and Moore, G., 1996. Trenches and trench-slope basins. *In* Ingersoll, R., and Busby, C. (Eds.), *The Tectonics of Sedimentary Basins:* New York (Blackwell), 179–219.

Young, J.R., 1998. Neogene. *In* Bown, P.R. (Ed.), *Calcareous Nannofossil Biostratigraphy* (Vol. 8): Dordrecht (Kluwer Academic), 225–265.

Figure F1. Stratigraphic column for Site 1175, showing lithostratigraphic units, ages, and characteristic lithologies.

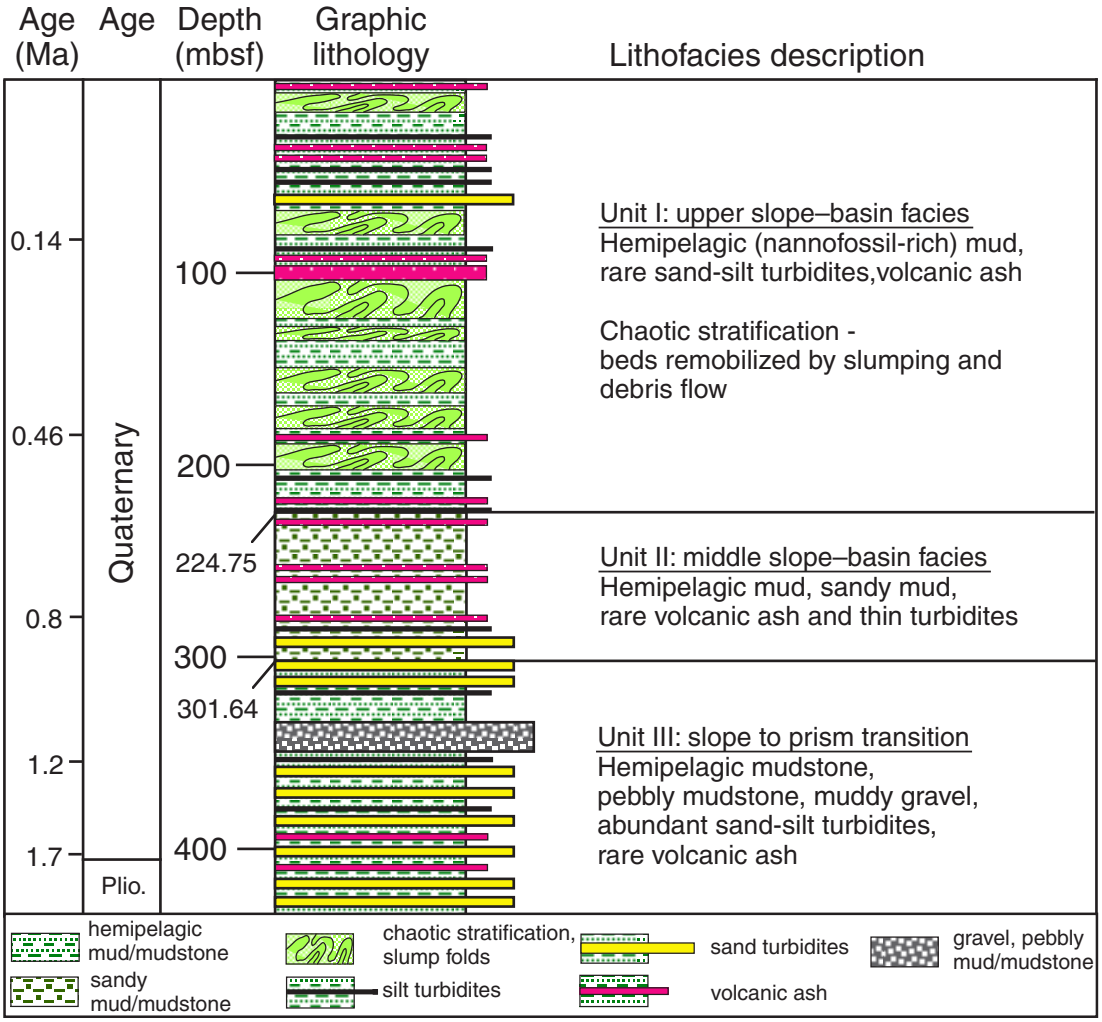

Figure F2. Distribution and thickness of volcanic ash layers.

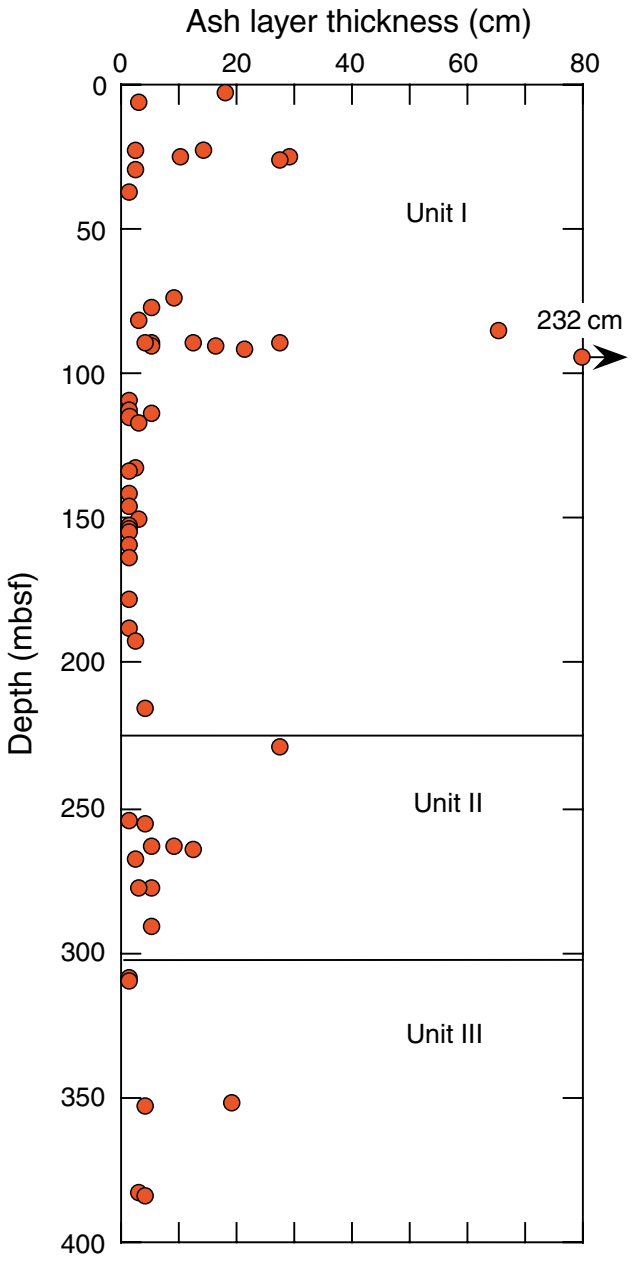

Figure F3. Volcanic ash from Unit I (interval 190-1175A-10H-5, 18–45 cm). The gray ash has a sharp base and diffuse top. Incorporated in the ash is greenish gray silty clay.

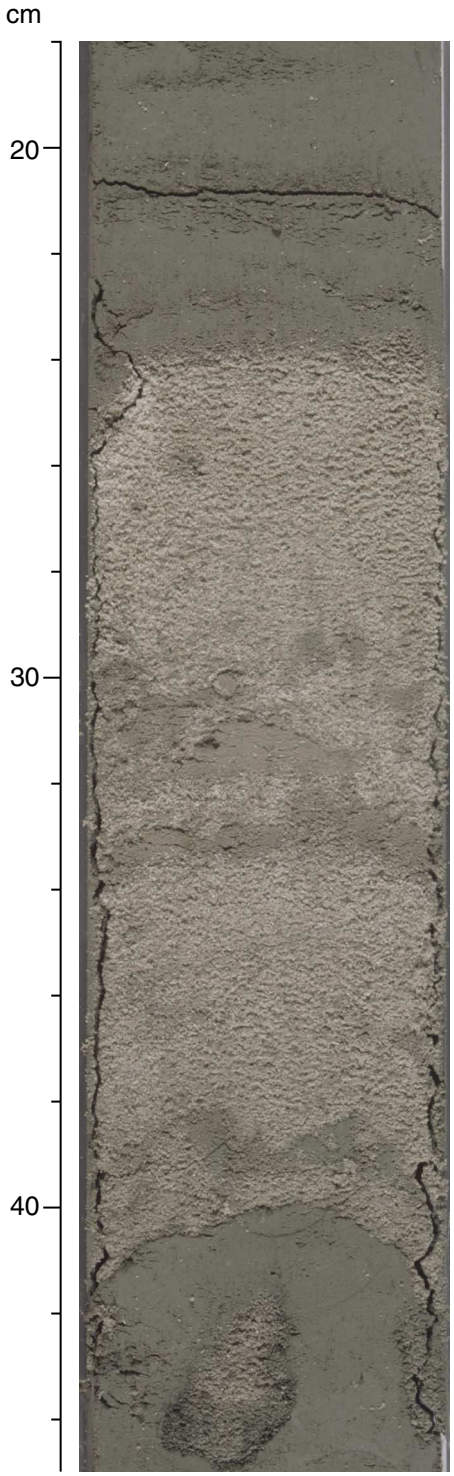

Figure F4. Dark brown sandy turbidite from Unit I with a sharp base, normal grading, and a diffuse top (interval 190-1175A-12H-1, 66–91 cm). Sandy patches are present in the silty clay.

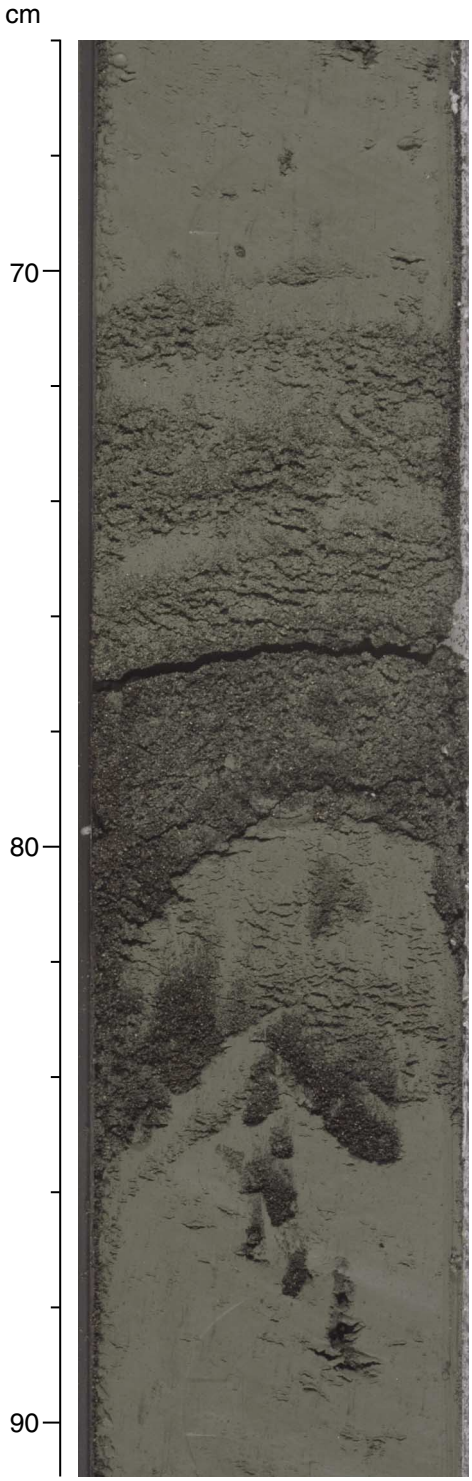

Figure F5. Overturned ash bed from Unit I (interval 190-1175A-21H-4, 60–70 cm).

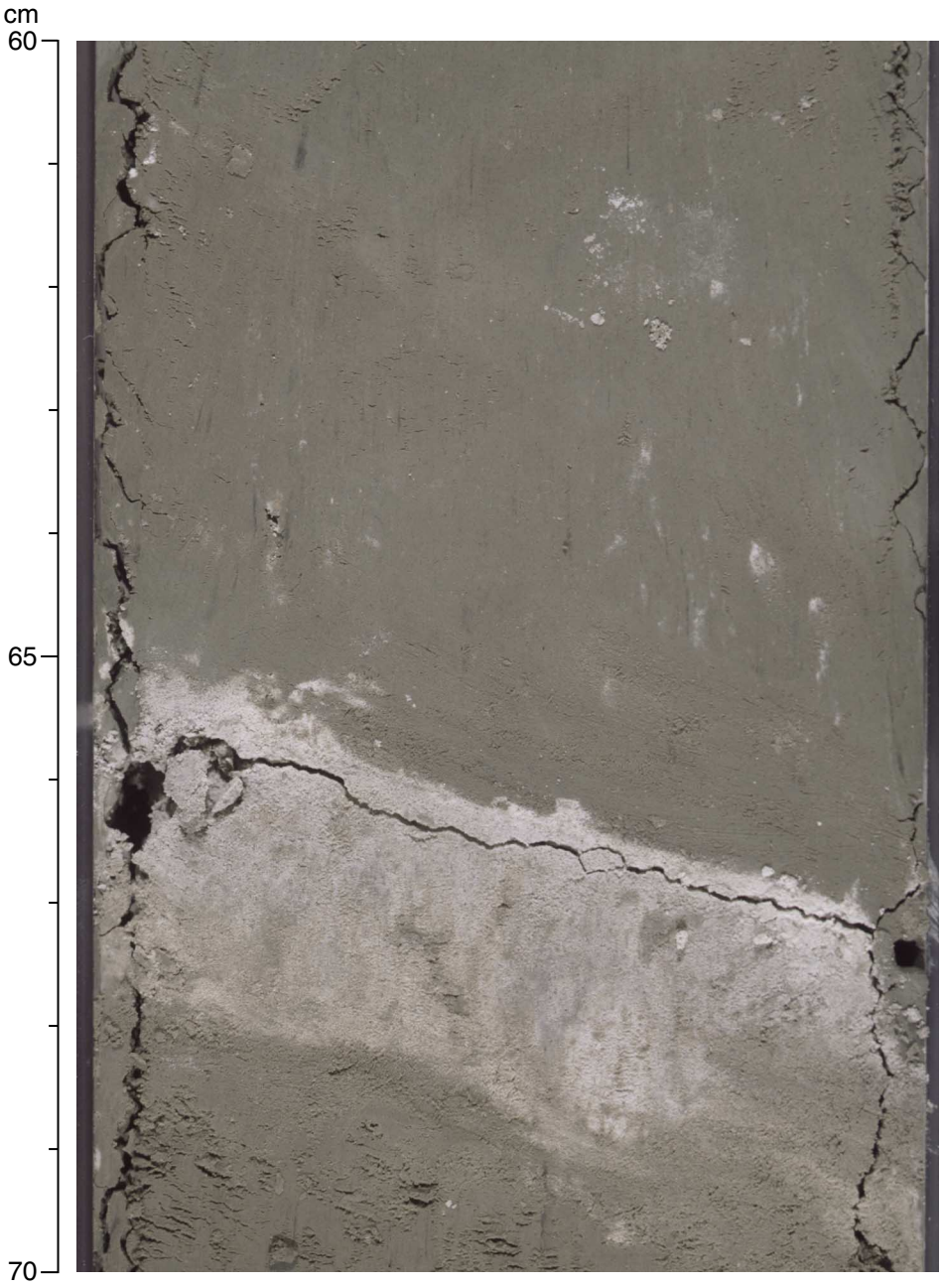

Figure F6. Chaotic bedding from Unit I with folded pink-brown ash and silty clay (interval 190-1175-9H-1, 65–110 cm).

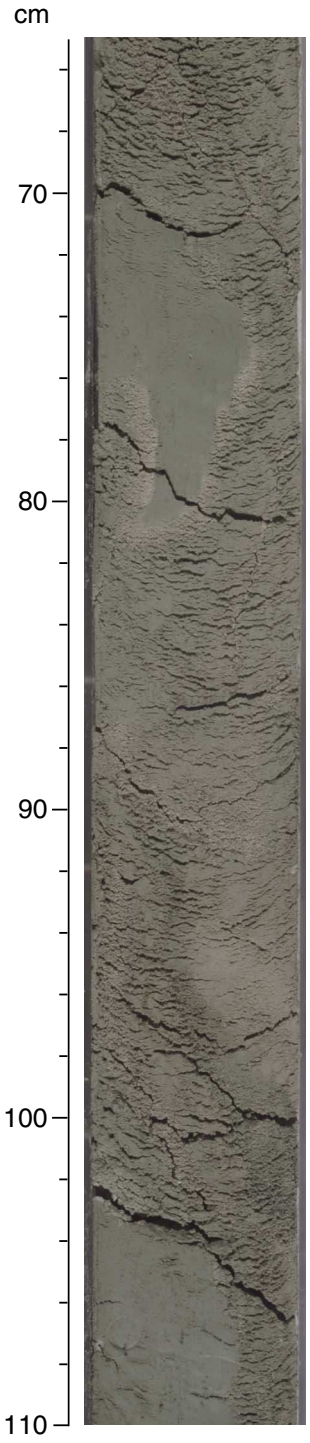

Figure F7. Pebbly mud from Unit III with abundant quartz and lithic clasts in a muddy matrix (interval 190-1175A-37X-4, 70–110 cm).

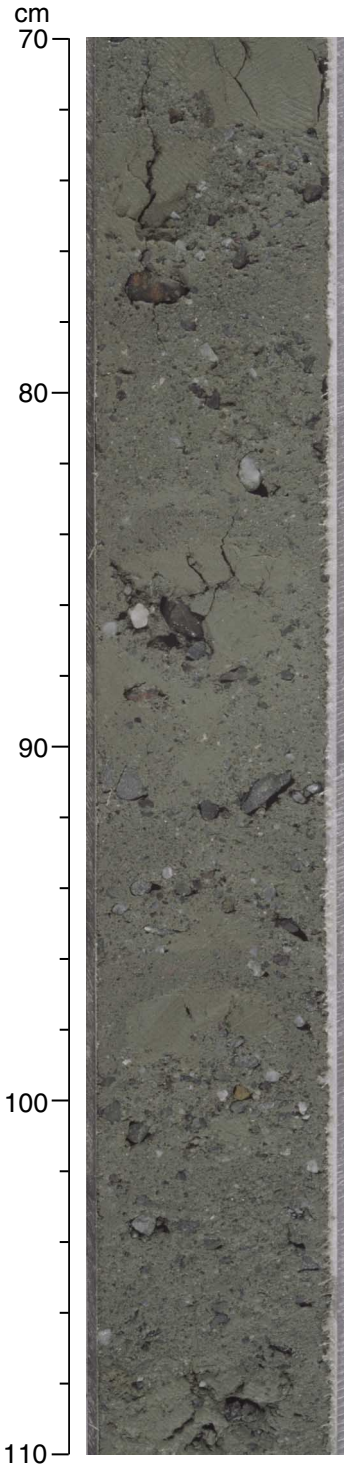

Figure F8. Normalized relative abundances of total clay minerals, quartz, plagioclase, and calcite at Site 1175 based on XRD analysis of random bulk-sediment powders.

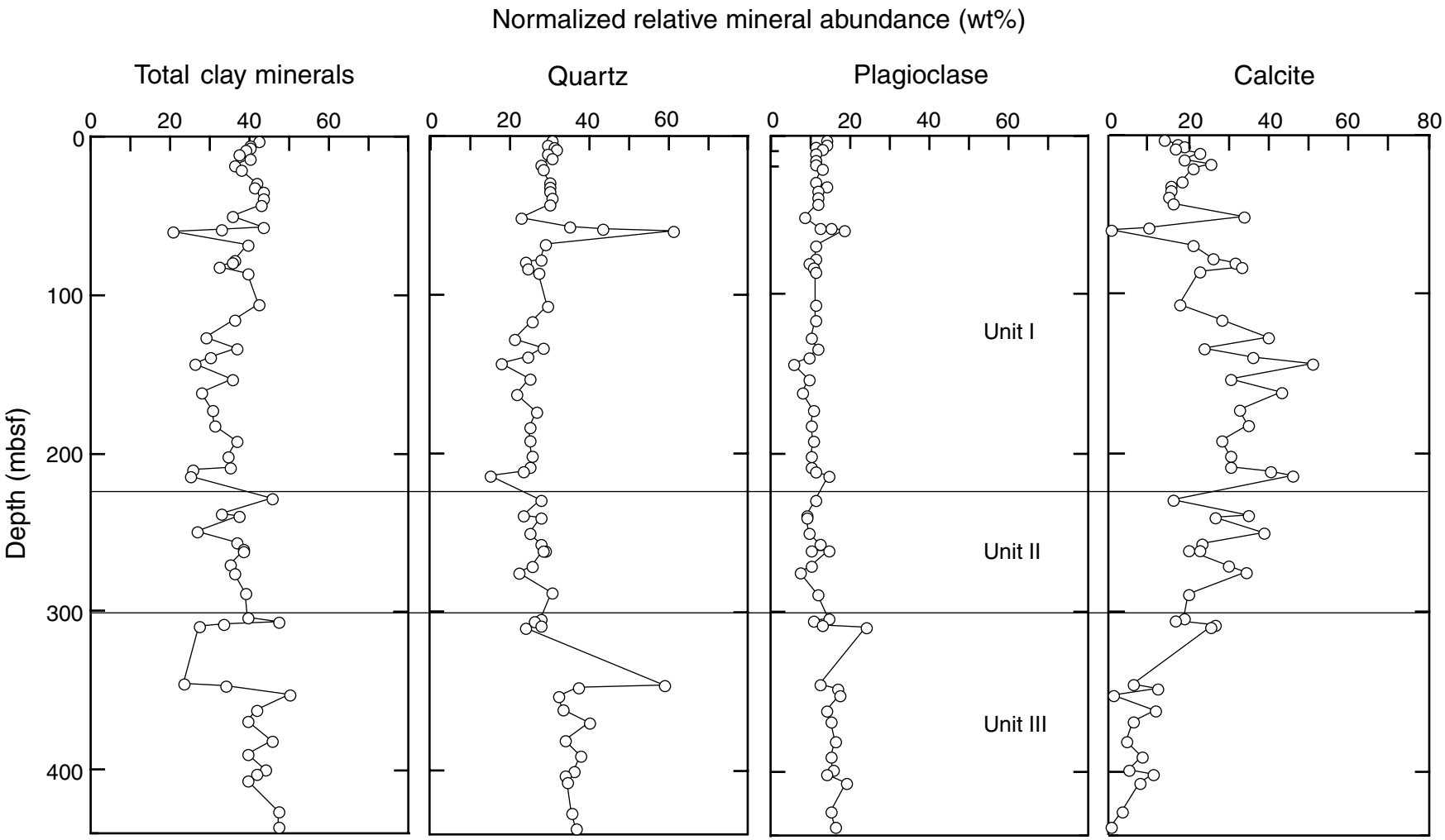

Figure F9. Bedding dips relative to the core liner plotted against depth. Dips <7.5° (shaded zone) are not thought to be significantly different from 0°. Bedding dips decrease abruptly below 220 mbsf. Generalized distribution of structural features (symbols are defined in Fig. F2, p. 34, in the "Explanatory Notes," chapter) is shown to the right along with observed displacements (in millimeters). The convolute lamination interval at 379 mbsf is also shown with a symbol.

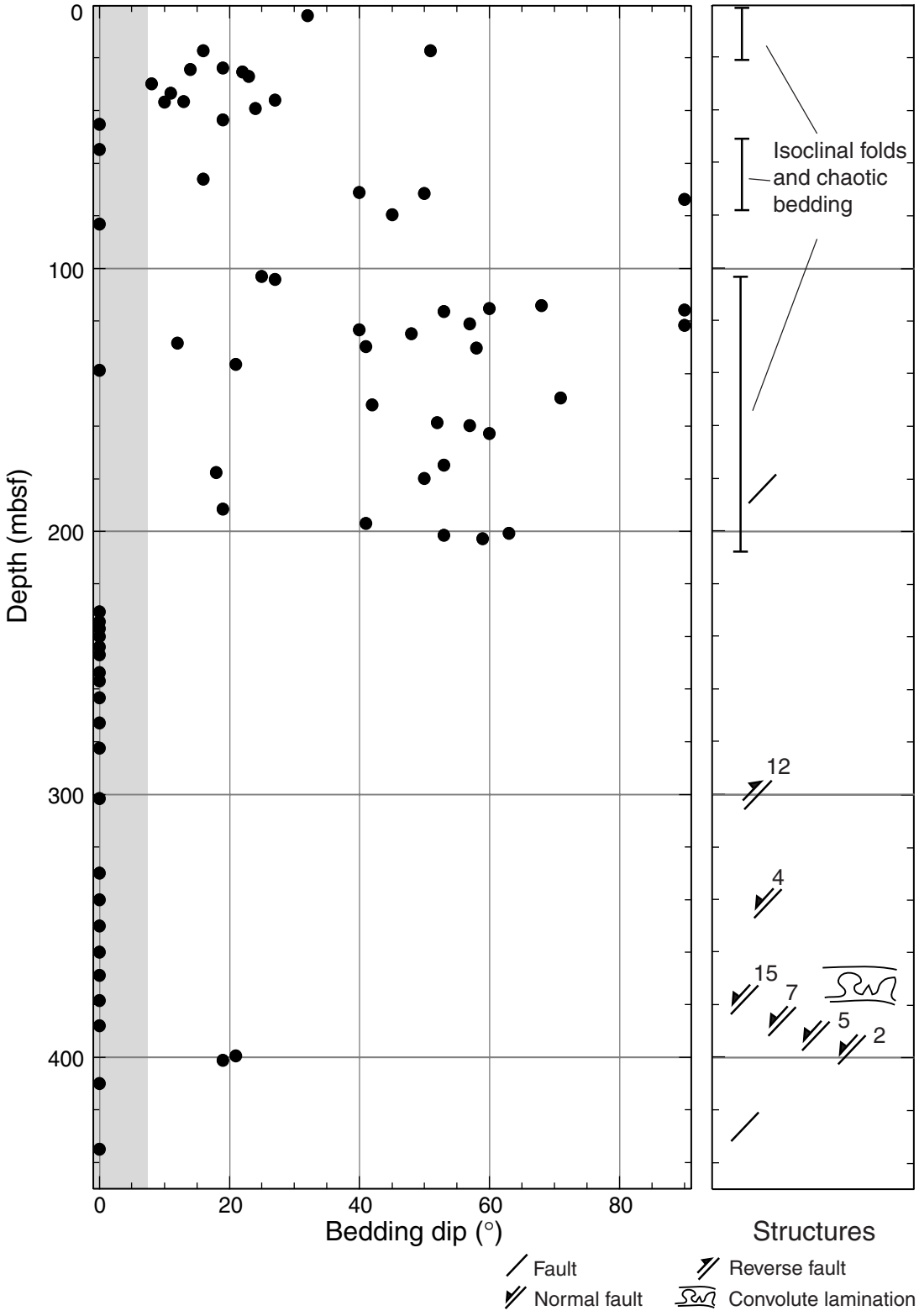

Figure F10. Example of a slump-fold hinge in Section 190-1175A-14H-5 (124.41 mbsf).

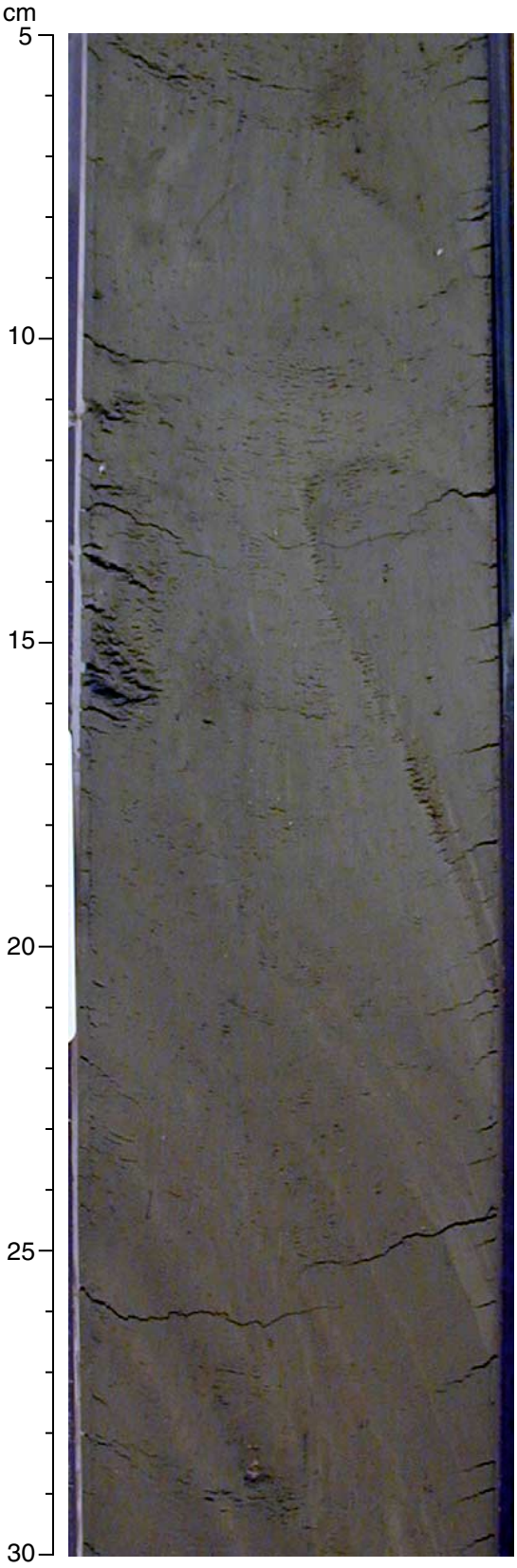

Figure F11. Equal-area lower-hemisphere stereographic projections in geographic coordinates (reoriented with Tensor tool compass data) of (**A**) poles to bedding and (**B**) fold axial planes (great circles) and fold axes (dots) measured on core-scale fold hinges. All are from the slumped intervals of Unit I (upper slope facies; 0–220 mbsf).

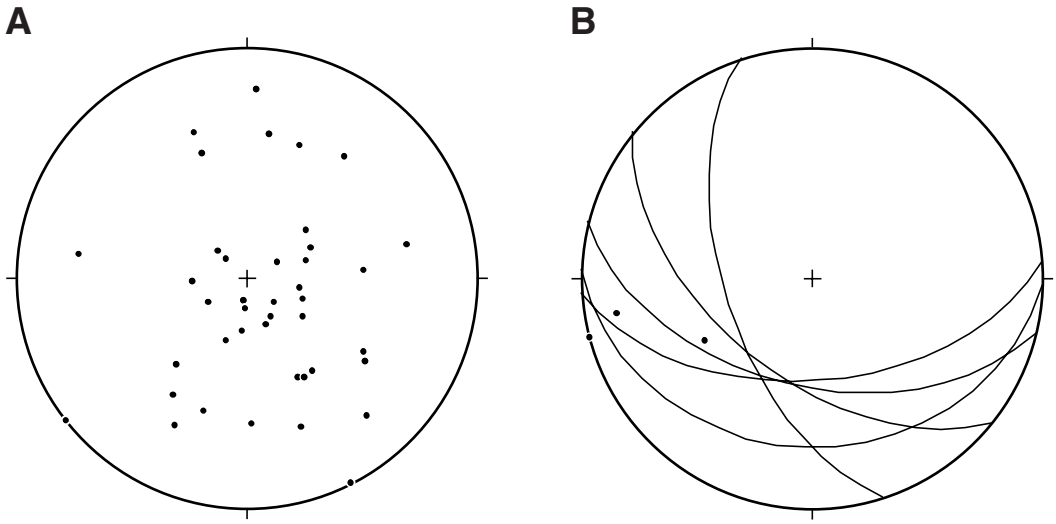

Figure F12. Equal-area lower-hemisphere stereographic projections in geographic coordinates (reoriented with NRM declination data) of the orientation of minor normal faults between 197 and 390 mbsf in Units II and III (middle and lower slope–basin facies).

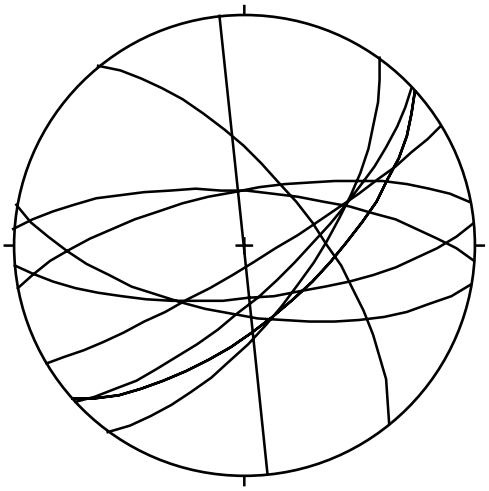

Figure F13. Poorly lithified coarse sand of Section 190-1175A-44X-1 (406.86 mbsf) exhibiting apparent web structure. Note, however, that the thick, convex-upward horizontal bands are interpreted as induced by XCB coring.

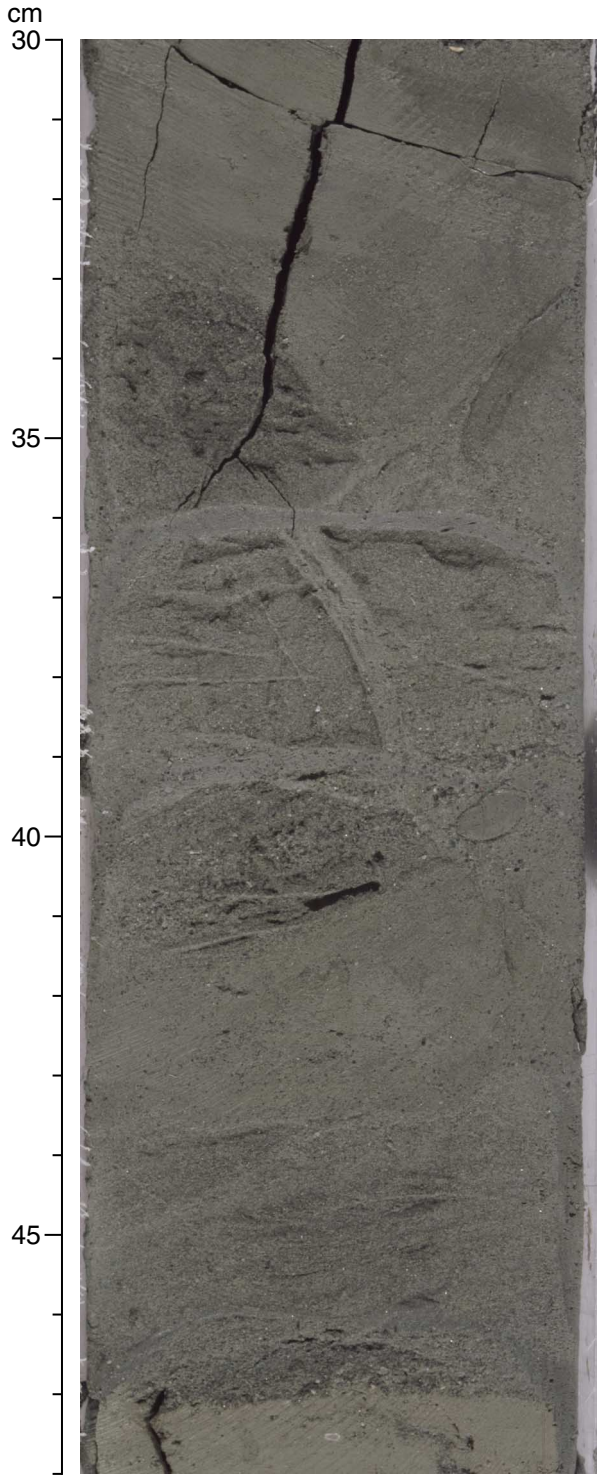

Figure F14. Uncalibrated gas-permeameter results from Site 1175.

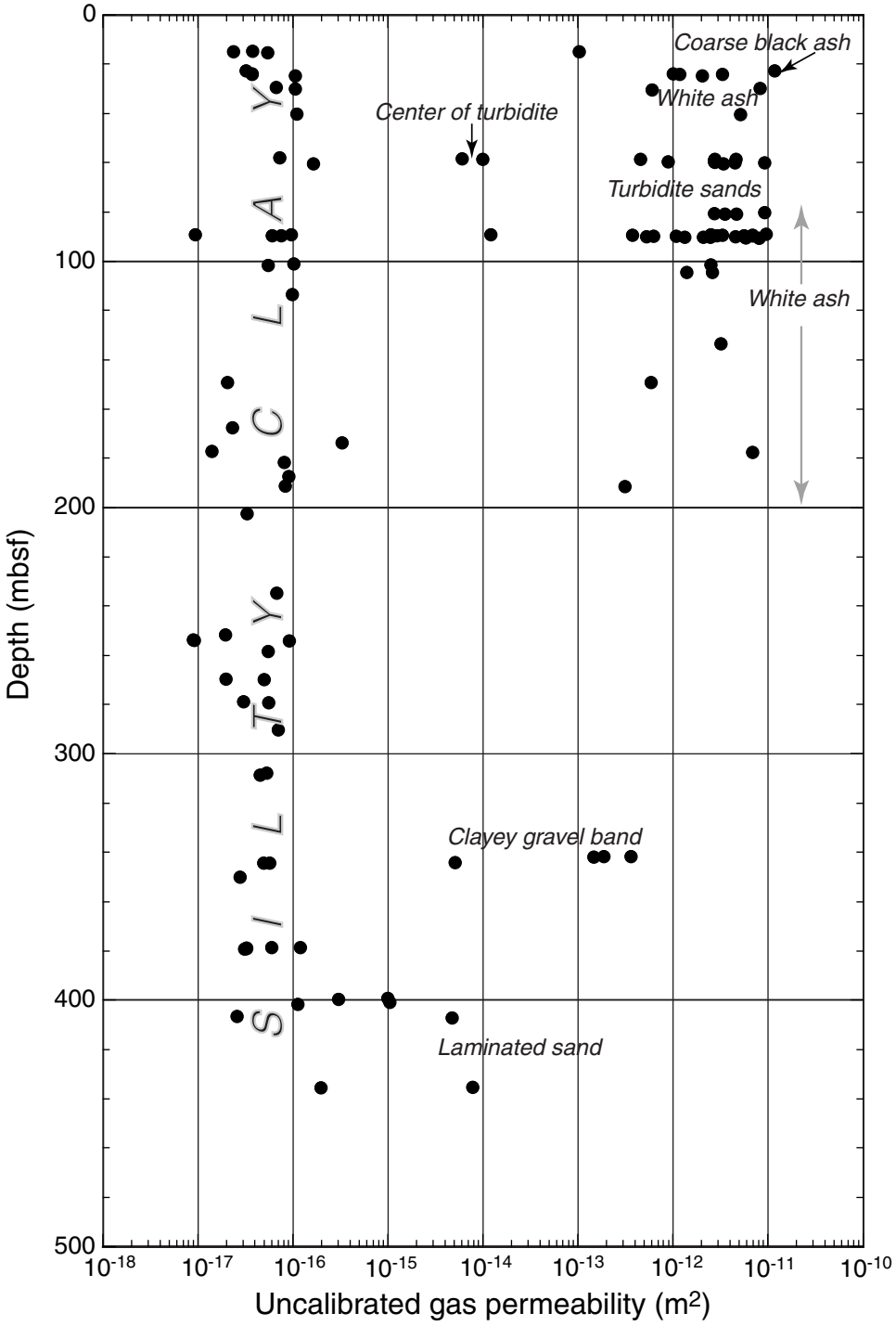

Figure F15. Paleomagnetic declination, inclination, and intensity after AF demagnetization at 30 mT at Hole 1175A. Declinations were corrected using Tensor tool orientation data.

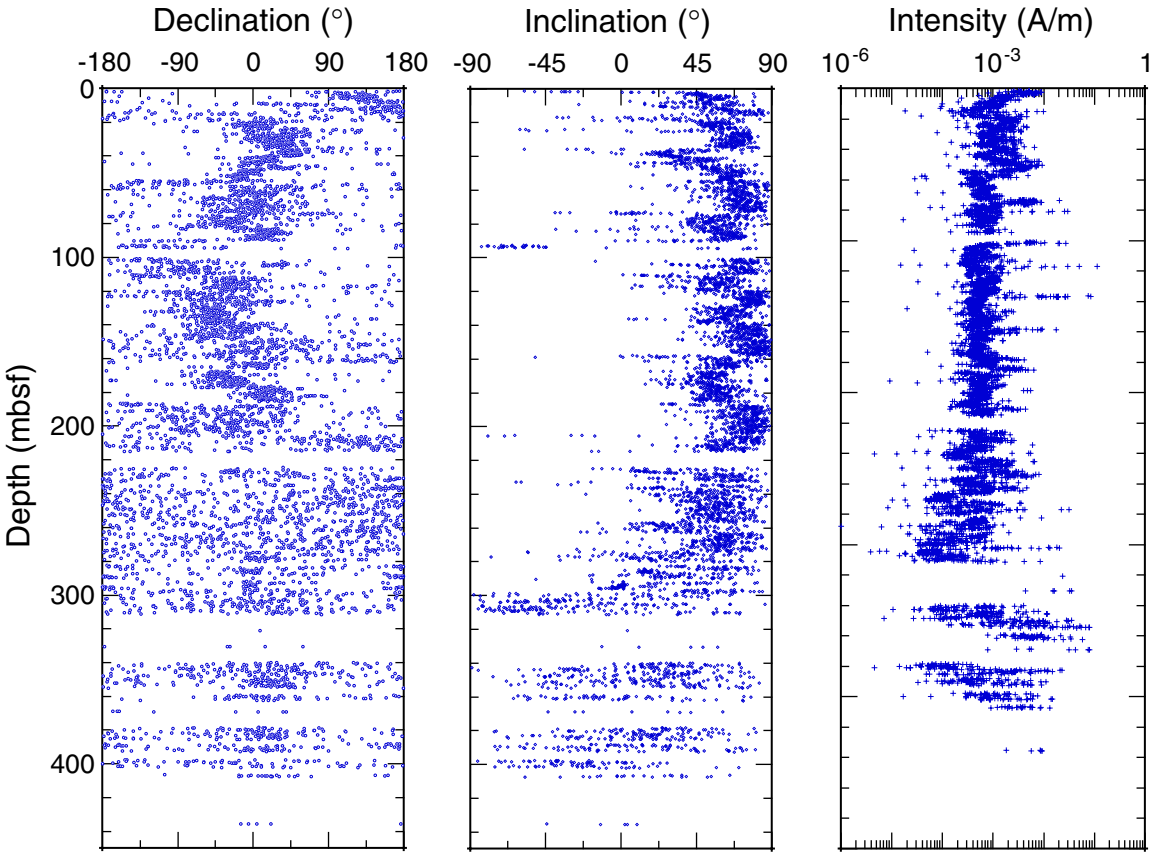

Figure F16. Site 1175 magnetostratigraphy. Black = normal polarity, white = reversed polarity, gray = unknown polarity, ? = questionable correlation.

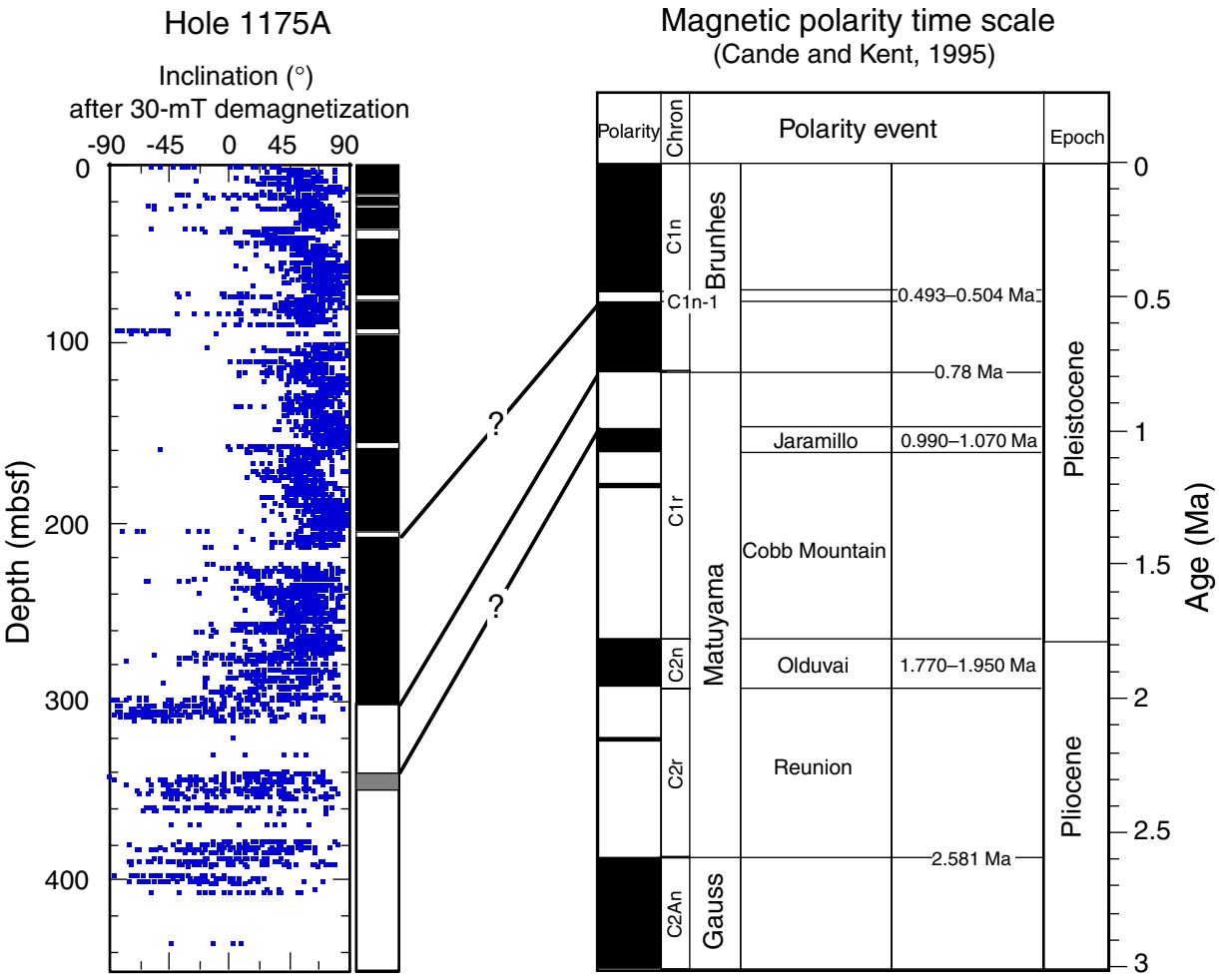

Figure F17. Site 1175 age-depth plot obtained from magnetostratigraphy and biostratigraphy. Black = normal polarity, white = reversed polarity, gray = unknown polarity, J = Jaramillo.

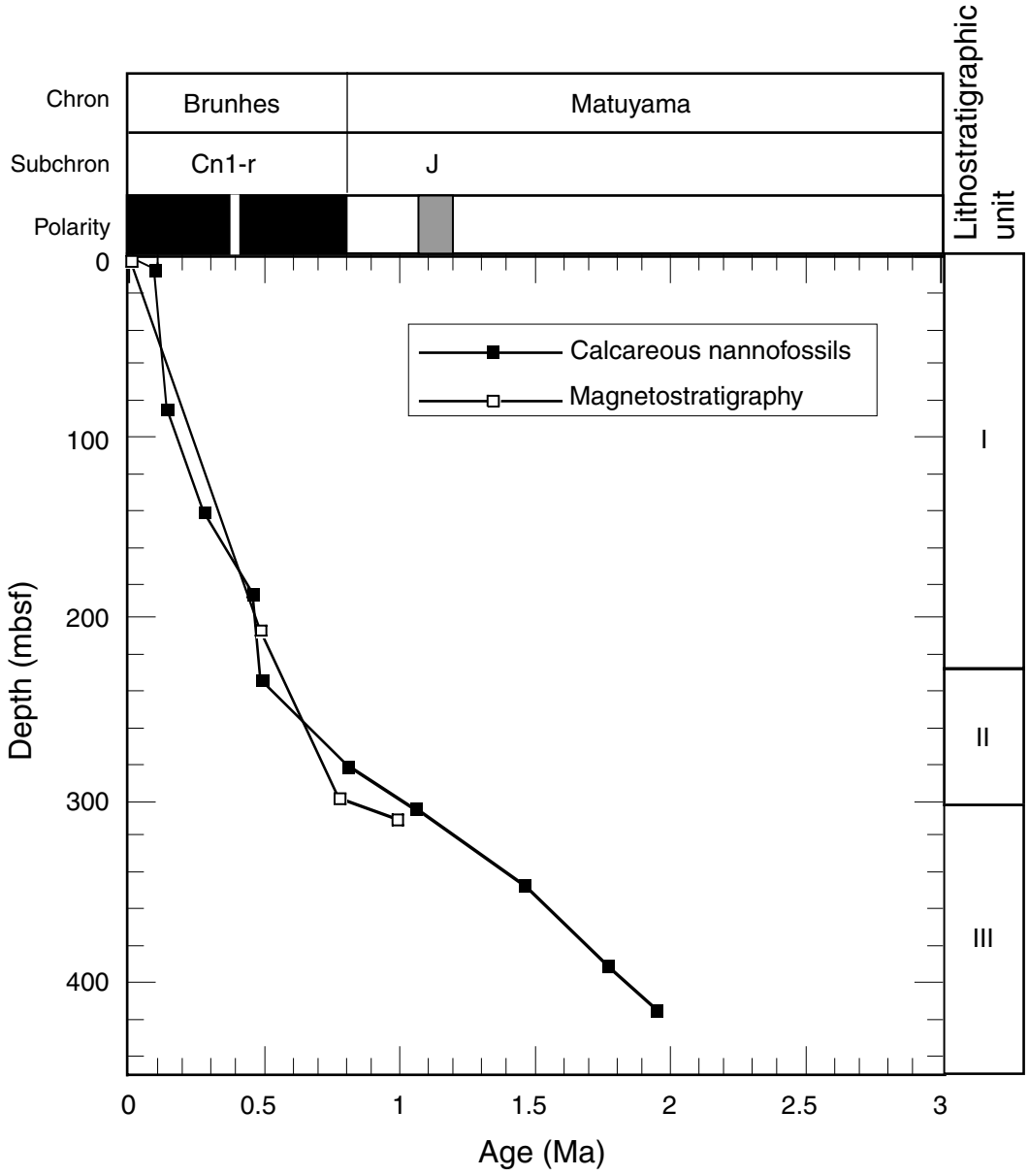

Figure F18. Magnetic disturbance experiment: a comparison of NRM from whole-round, working-half, and archive-half of Core 190-1175A-3H. Declinations were corrected using Tensor tool orientation data.

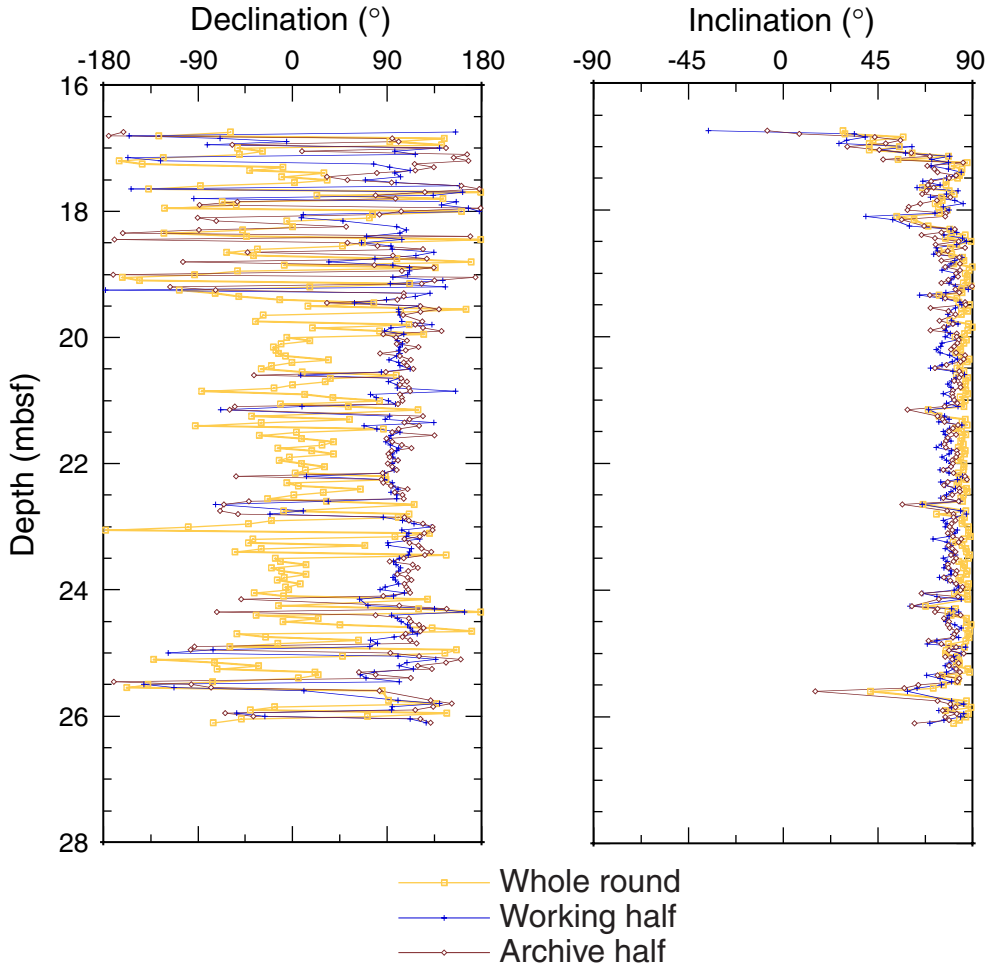

Figure F19. Overprint removal experiment: a comparison of whole-round Core 190-1175A-3H NRM to its archive-half magnetic remanence after AF magnetization at 30 mT.

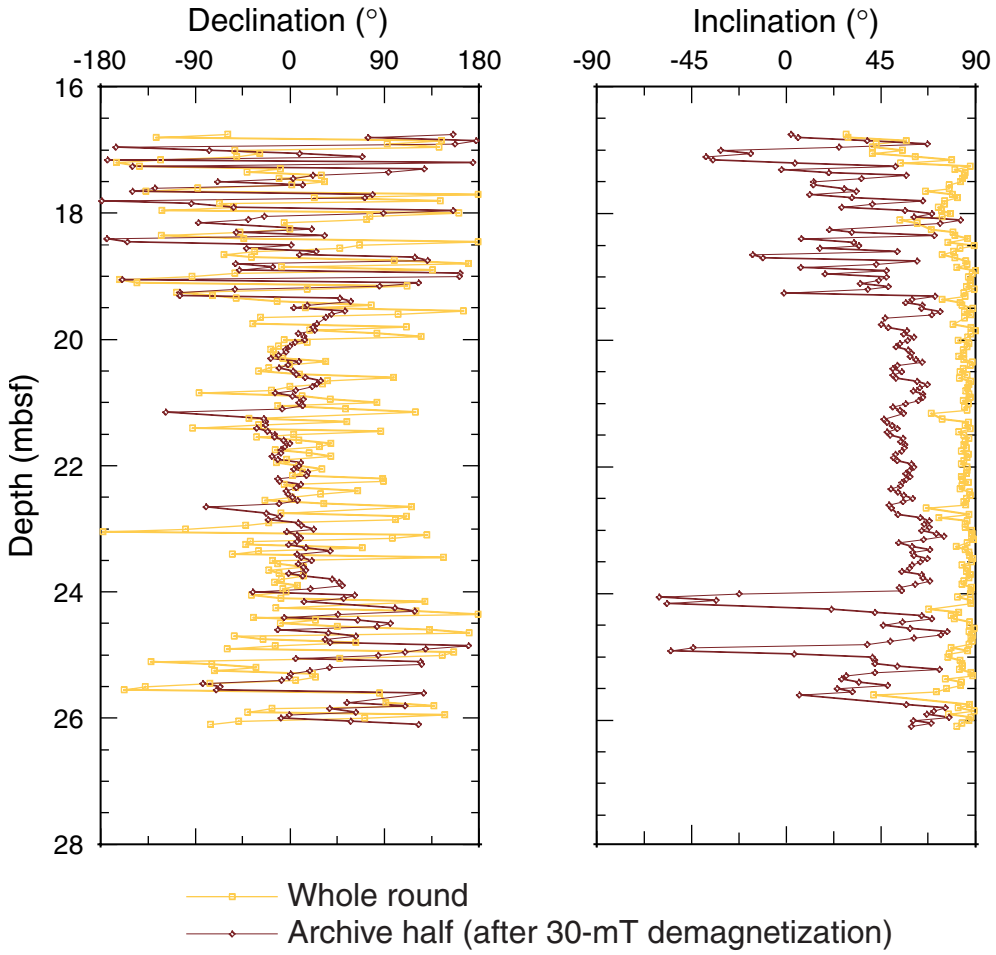

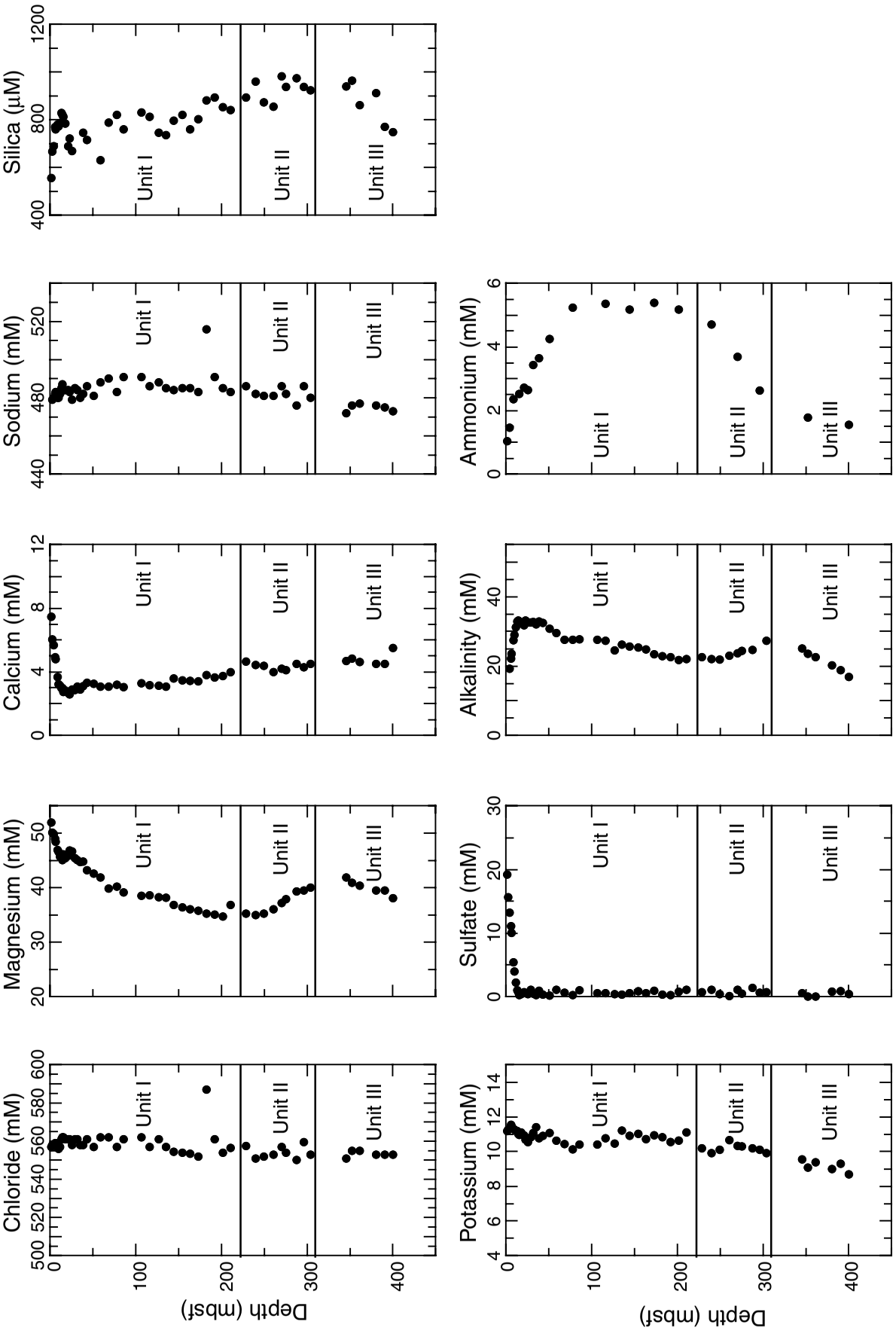

Figure F20. Pore fluid compositions as a function of depth in Hole 1175A. Solid horizontal lines indicate lithostratigraphic boundaries.

Figure F21. A. Molecular compositions and concentrations of headspace gases given in parts per million. **B.** Percentage of inorganic carbon (carbonate in weight percent) in the bulk sediments at Site 1175.

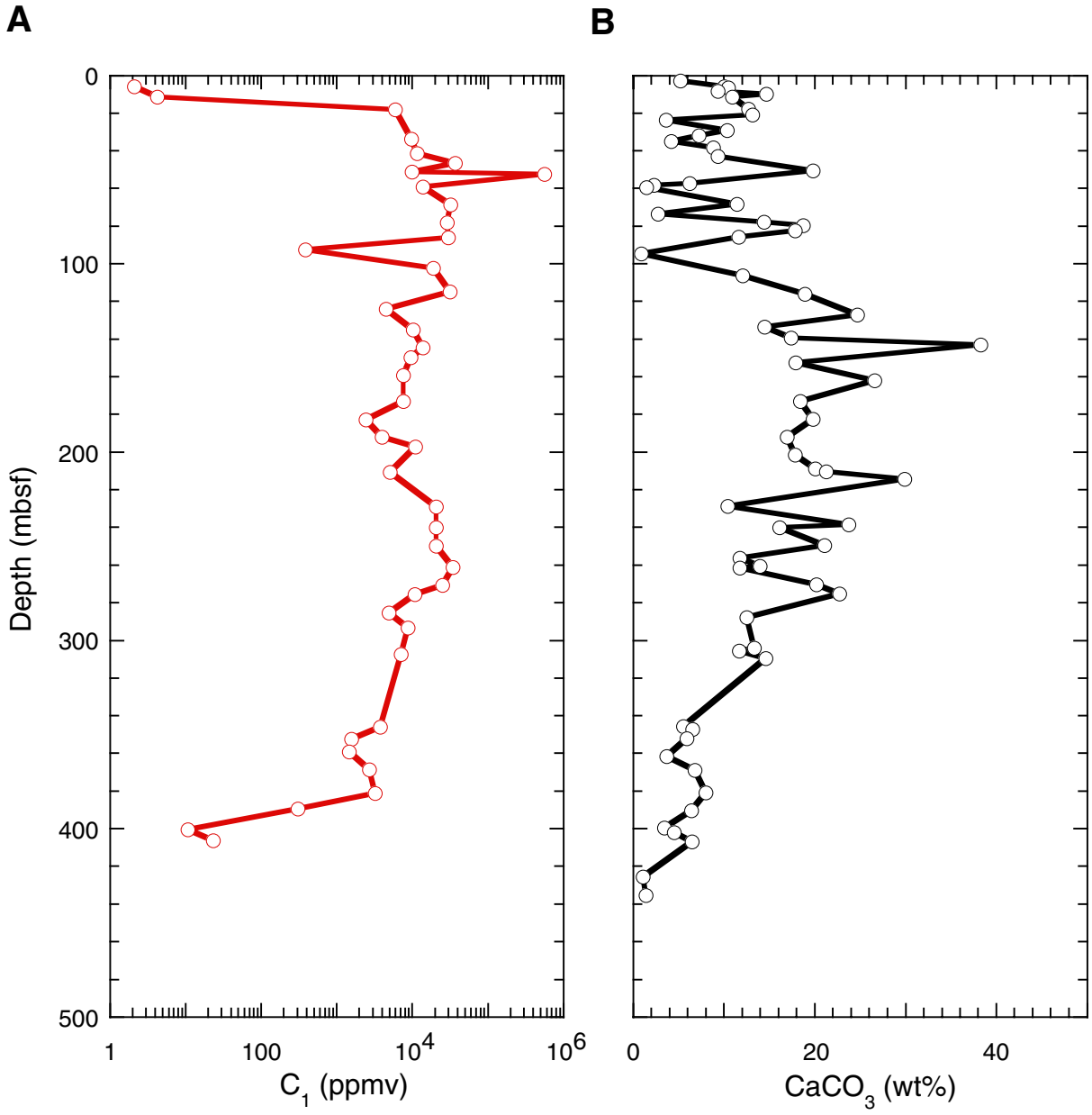

Figure F22. Depth distribution of total bacterial populations in sediment samples from Hole 1175A. The curved dashed line represents a general regression line of bacterial numbers vs. depth in deep-sea sediments (Parkes et al., 1994), with 95% upper and lower prediction limits shown by the curved lines of longer dashes. The shaded area to the left of the figure indicates levels where bacterial populations are too low to be detected with the acridine orange direct count technique. The detection limit was 6×10^4 cells/cm^3.

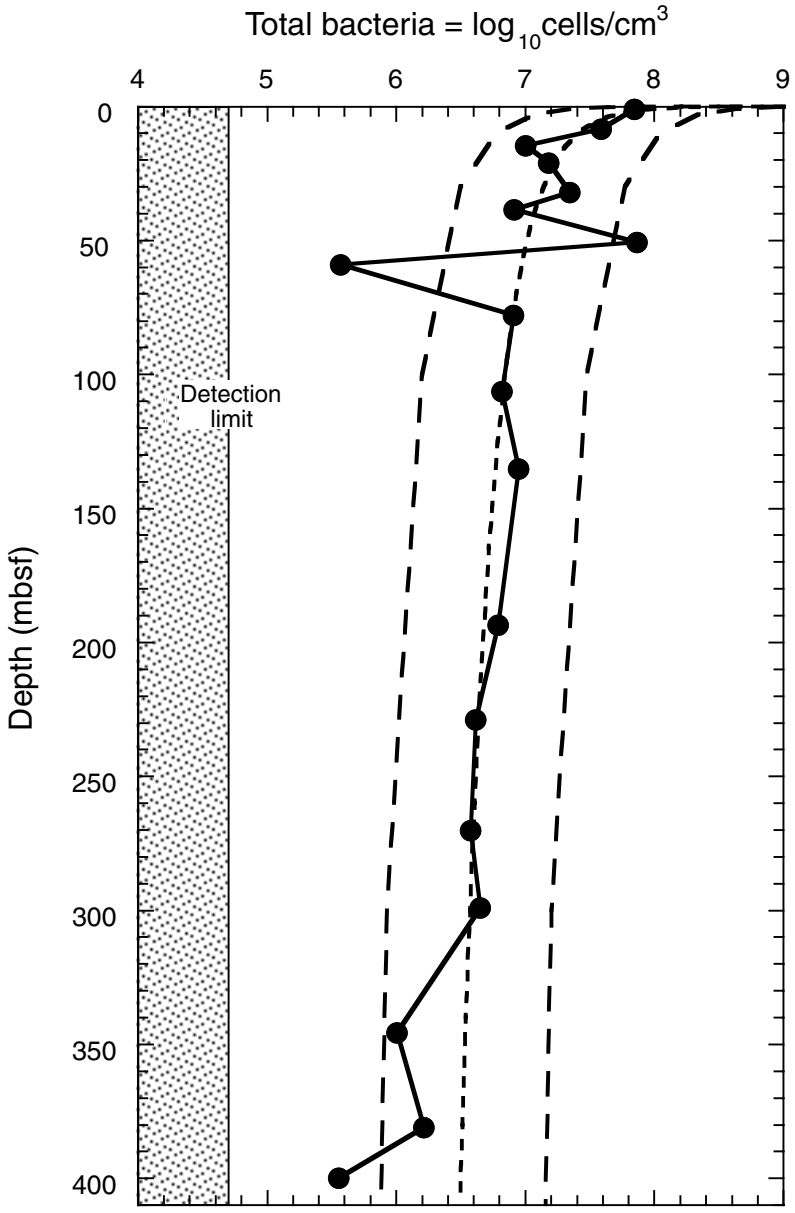

Figure F23. Depth profiles of total bacteria (solid circles) and methane concentrations (open circles).

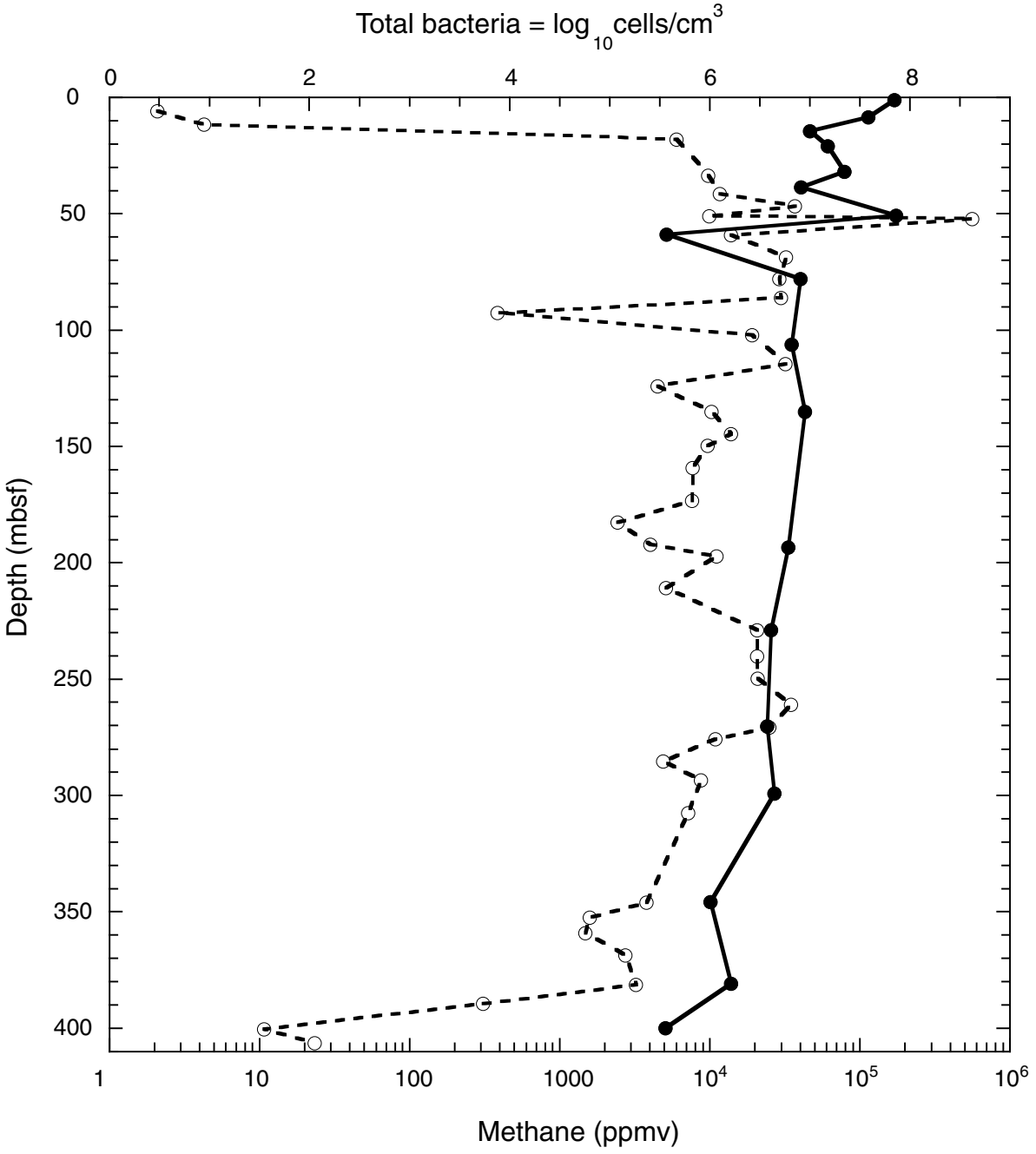

Figure F24. A. Site 1175 bulk-density measurements. Lithostratigraphic Units I (upper slope–basin facies), II (middle slope–basin facies), and III (lower slope–basin facies) are indicated. **B.** MST/GRA and mass/volume bulk density. **C.** Grain density. **D.** Porosity.

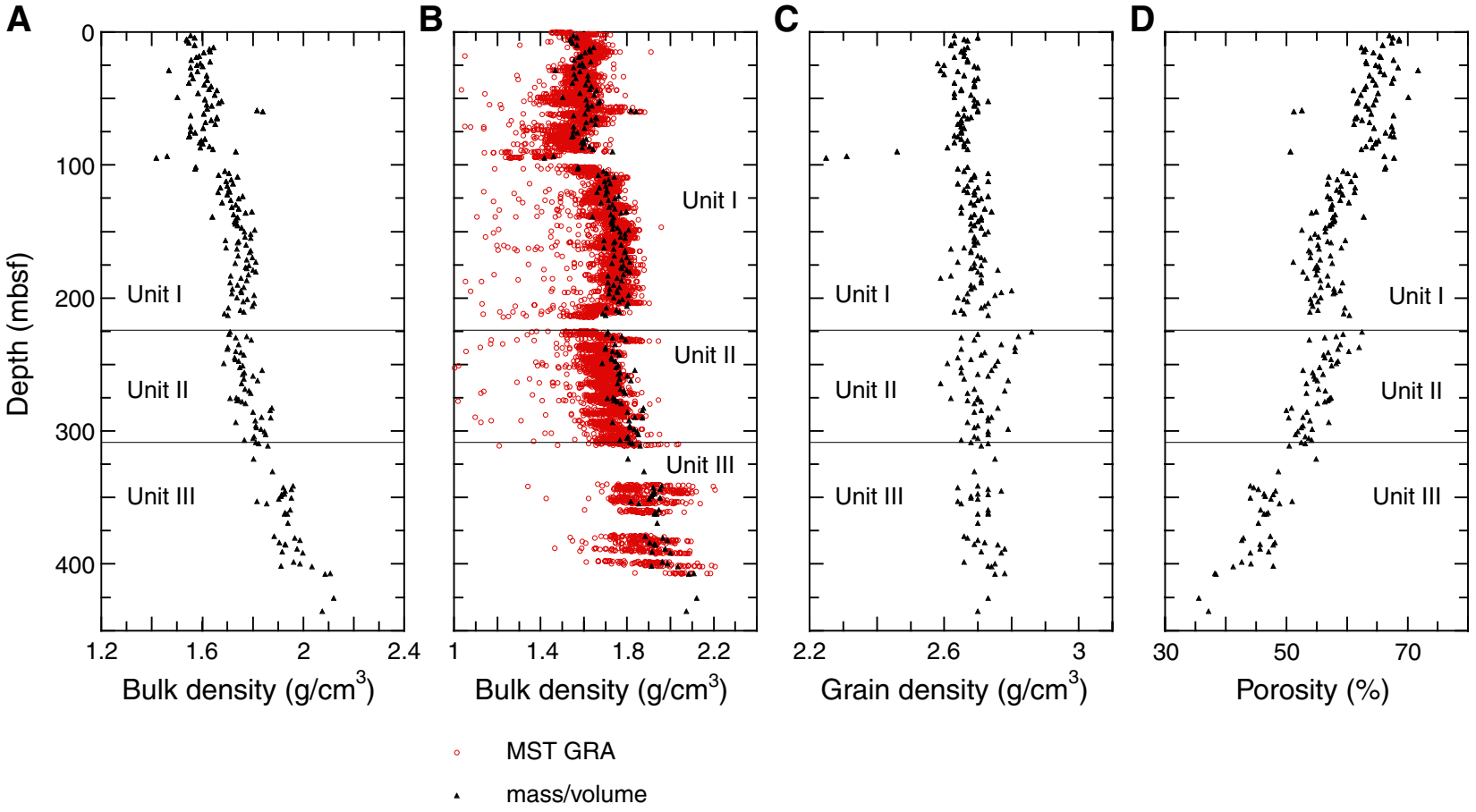

Figure F25. Site 1175 undrained peak shear strength.

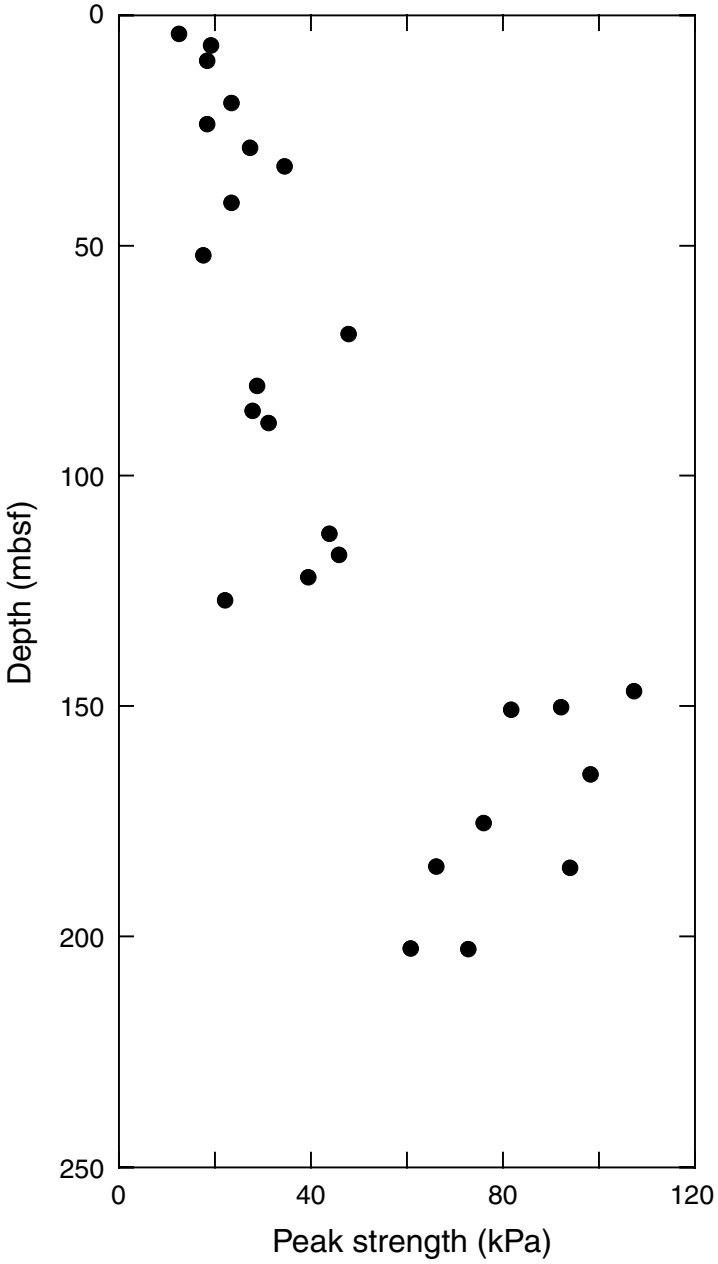

Figure F26. **A.** Site 1175 thermal conductivity. **B.** Observed (triangles) and projected (dashed line) temperatures.

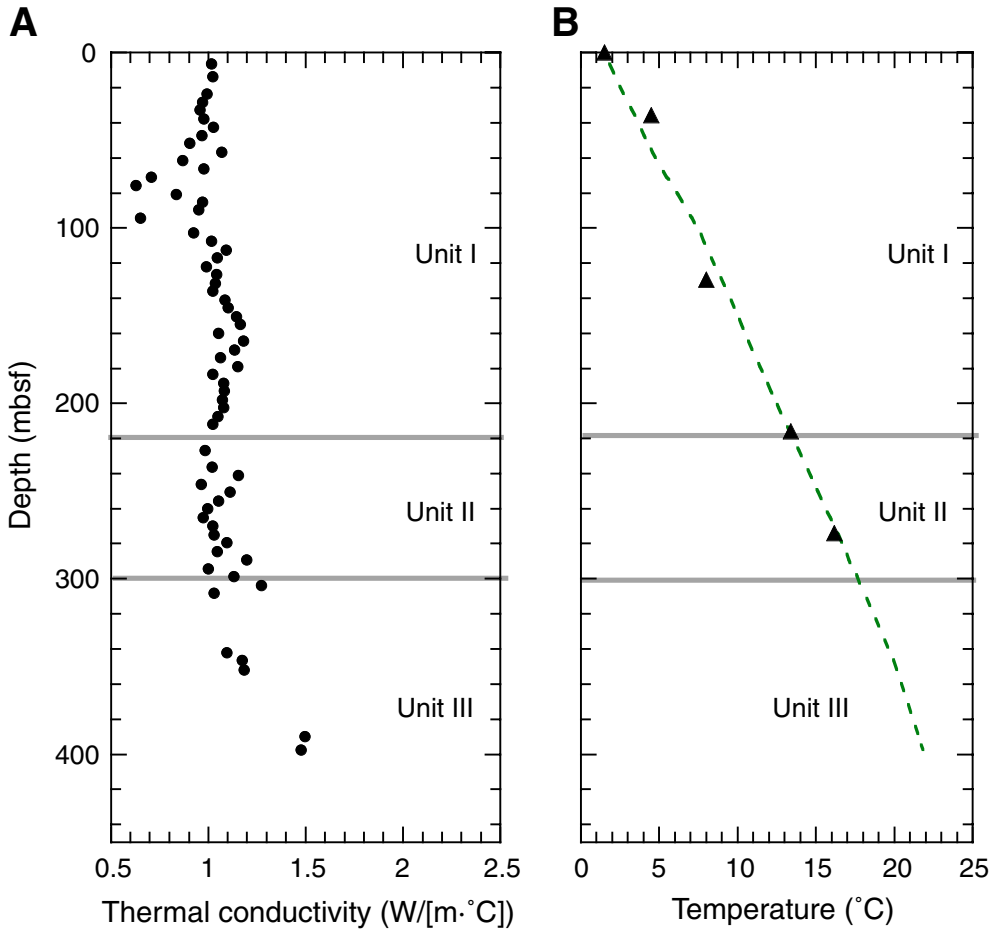

Figure F27. A. Site 1175 *P*-wave velocity. **B.** Impedance computed from velocity and bulk-density data.

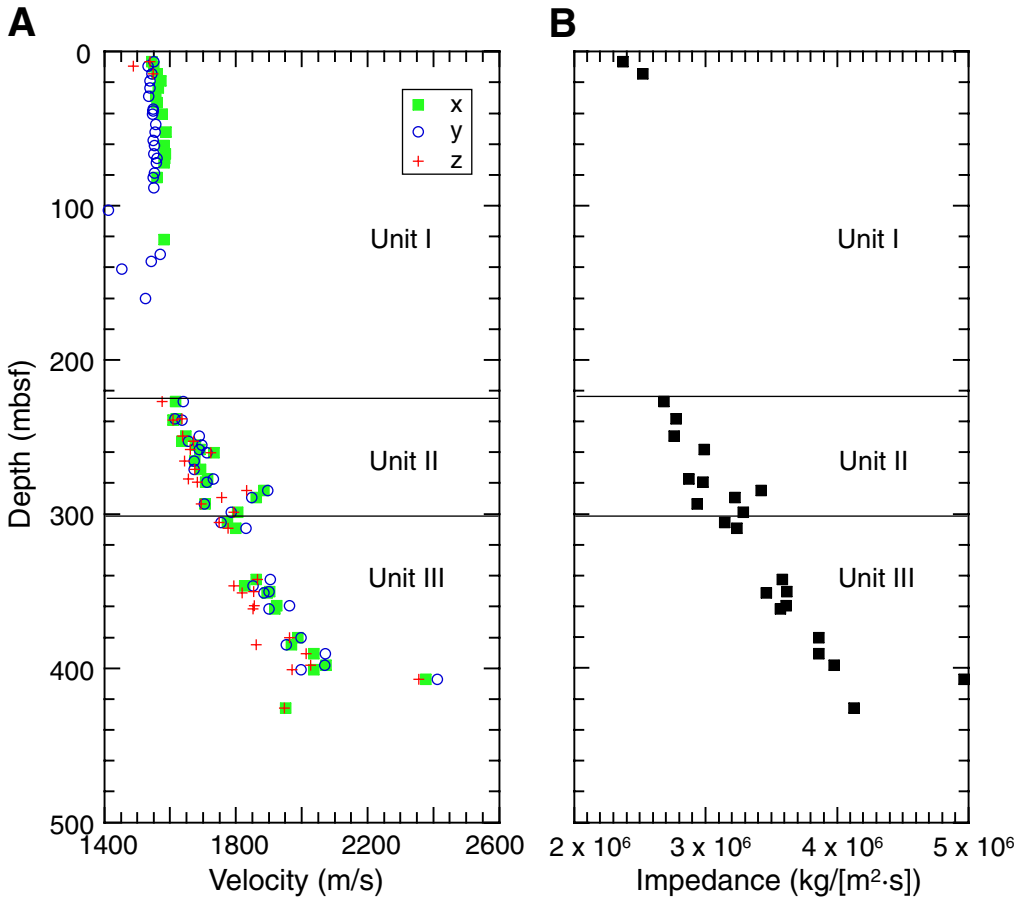

Figure F28. Site 1175 formation factor. Needle-probe measurements on APC cores were performed in the y- (across core) and z- (along core) directions. Measurements on cut samples were performed in the x- (orthogonal to core), y- (orthogonal to core), and z- (parallel to core) directions.

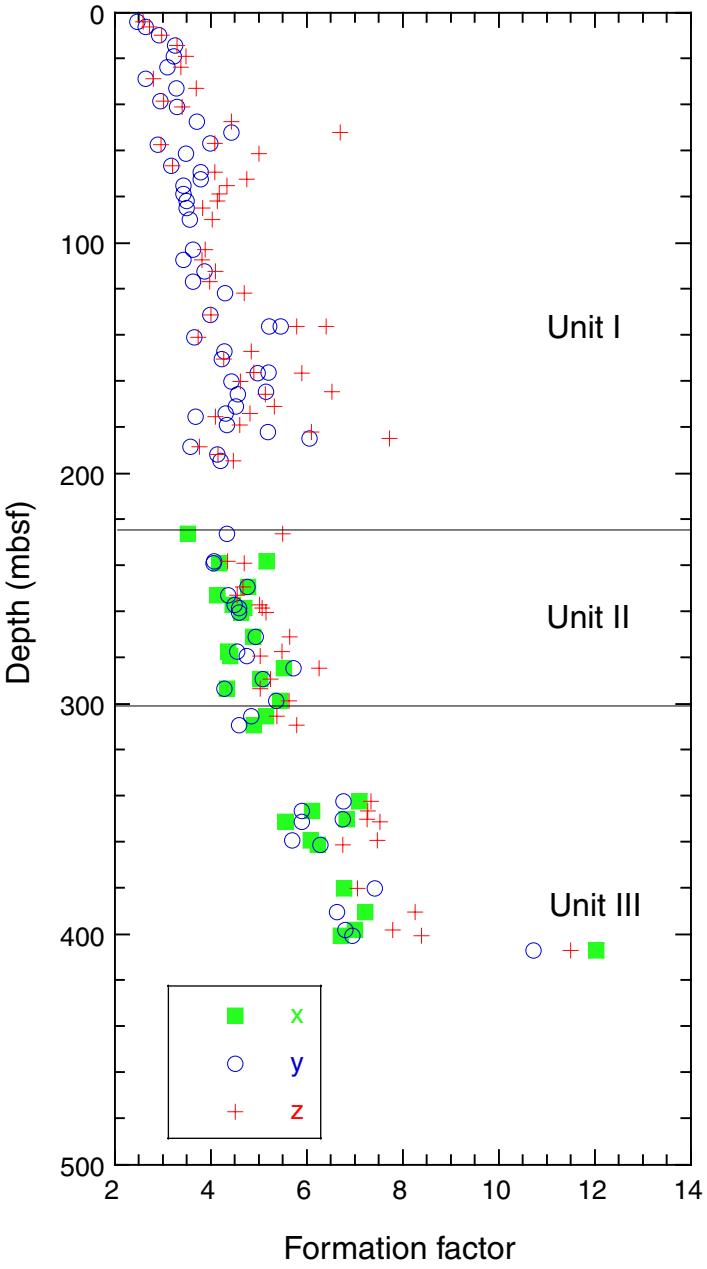

Figure F29. Site 1175 magnetic susceptibility.

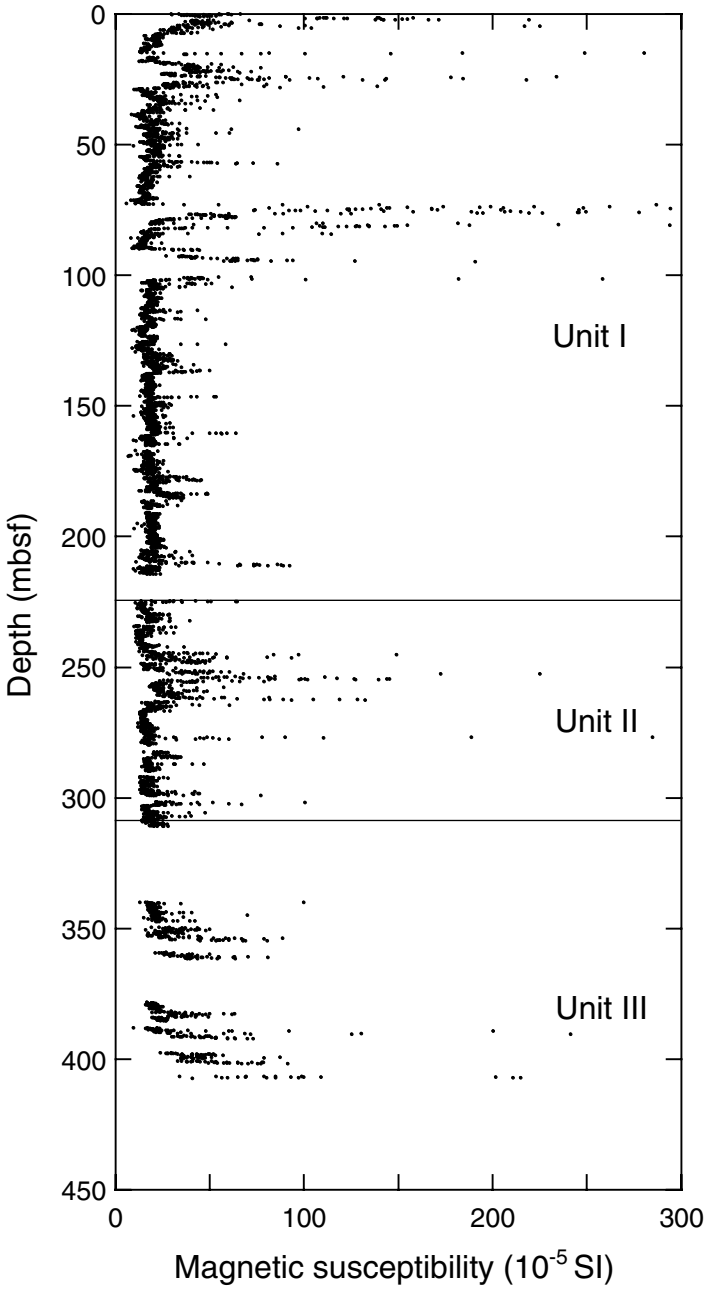

Figure F30. Site 1175 natural gamma ray.

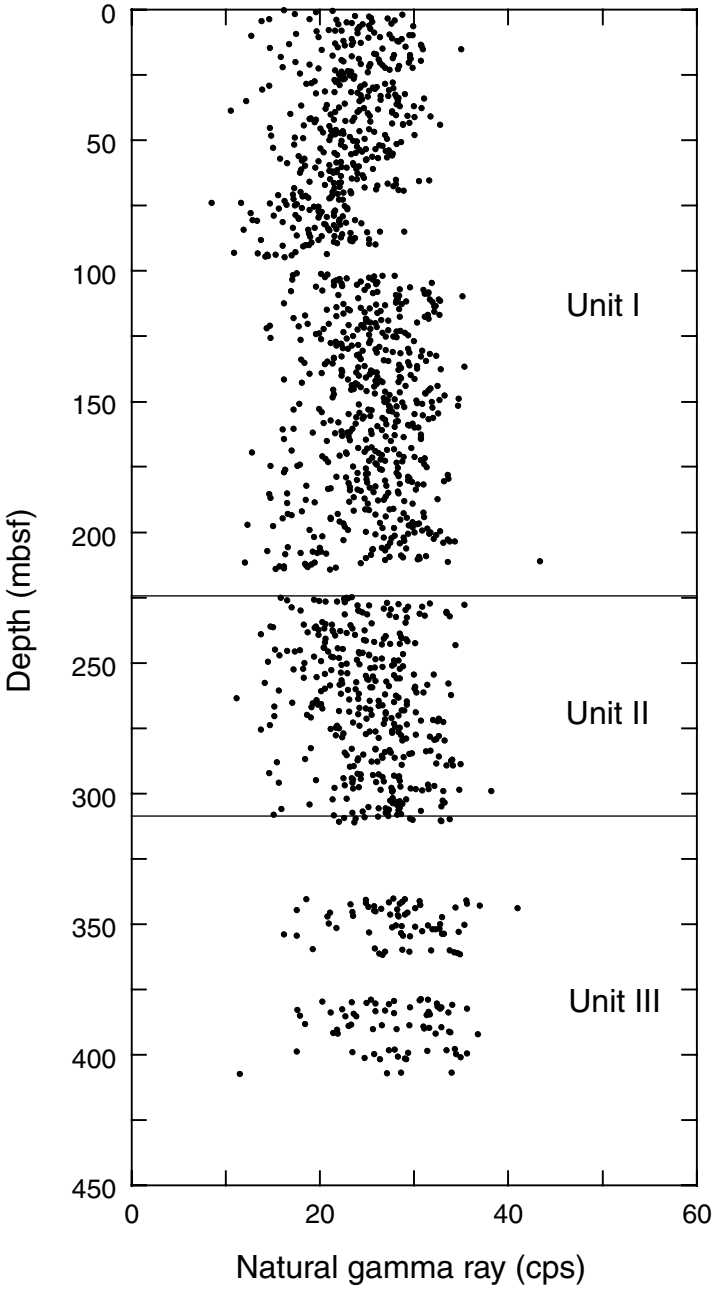

Figure F31. Temperatures measured during the deployment of the Adara APC temperature tool in Hole 1175A (**A**) at the bottom of Core 190-1175A-4H and (**B**) at the bottom of Core 14H. Dashed lines = extrapolated temperatures, solid line = mudline temperature.

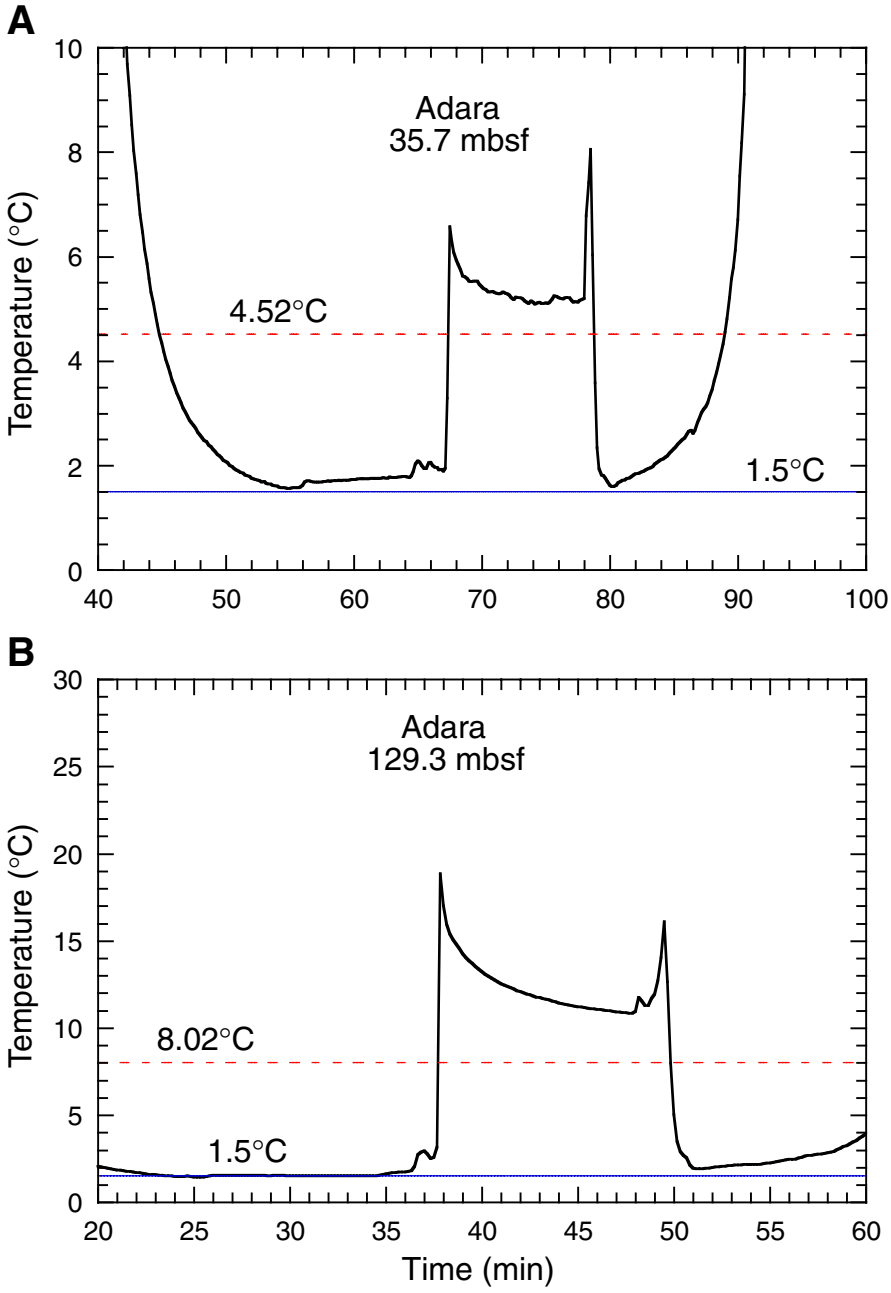

Figure F32. Temperatures measured in Hole 1175A during the DVTP stations (**A**) after Core 190-1175A-23X and (**B**) after Core 190-1175A-29X. Dashed lines = extrapolated in situ temperatures.

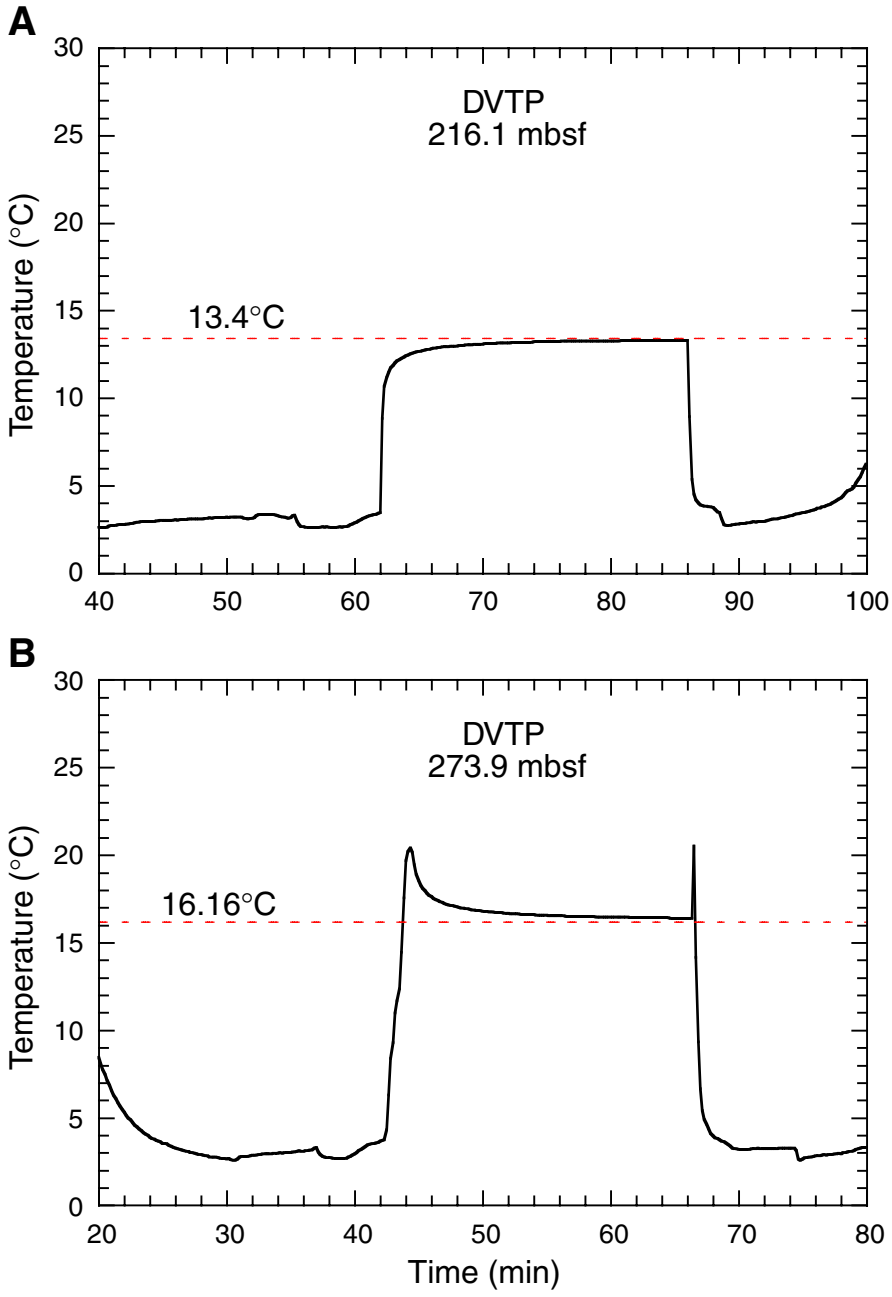

Figure F33. Hole 1175A temperatures. The equation shows linear best fit.

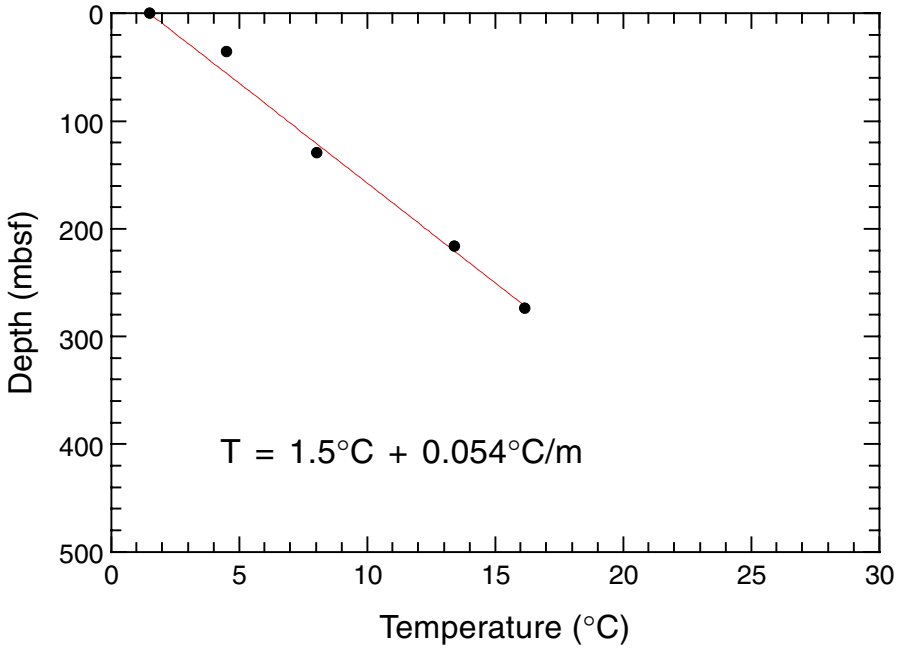

Figure F34. Pressures measured in Hole 1175A during the DVTP-P stations (**A**) after Core 190-1175A-23X and (**B**) after Core 190-1175A-29X.

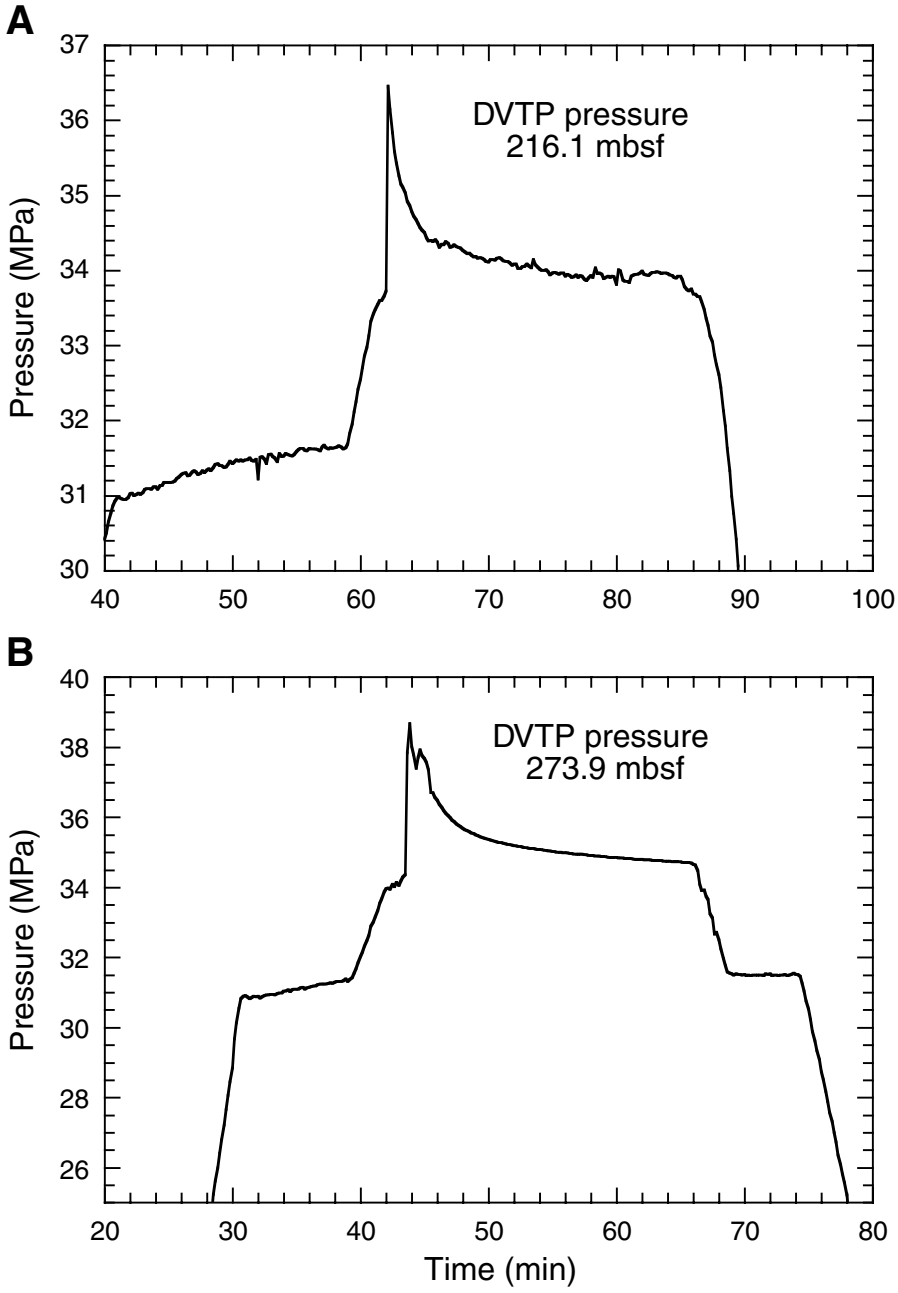

Figure F35. Three-dimensional seismic reflection line 281 across Site 1175. This line has been 3-D stacked and migrated.

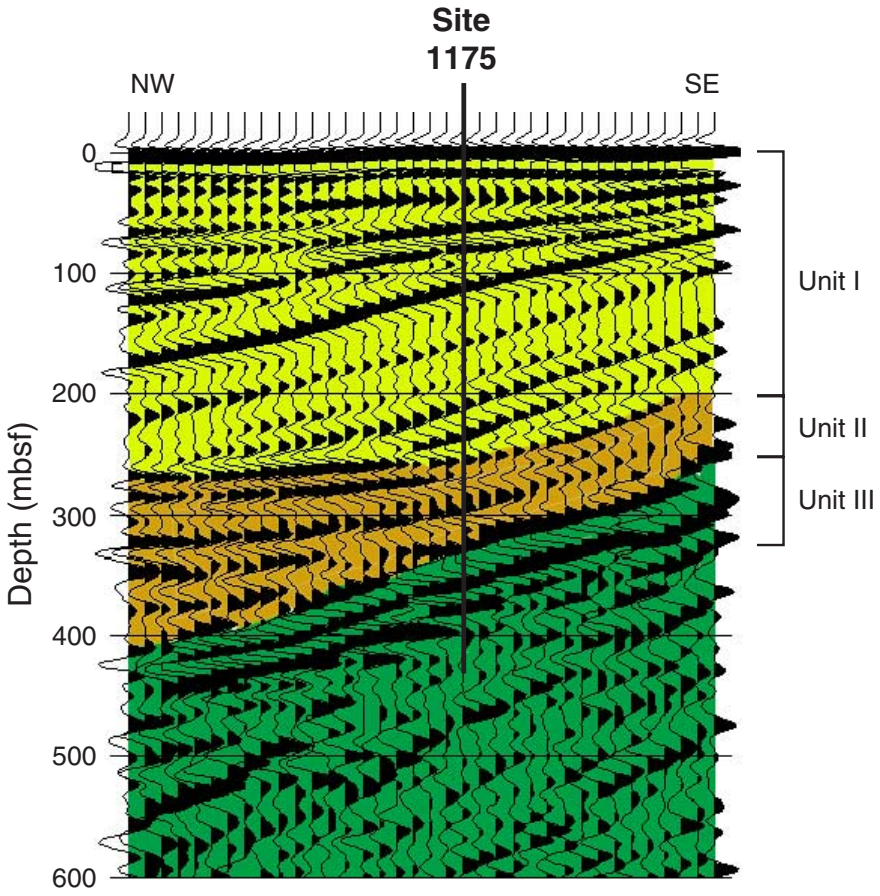

Table T1. Coring summary, Site 1175.

Core	Date (June 2000)	Time (local)	Depth (mbsf) Top	Depth (mbsf) Bottom	Length (m) Cored	Length (m) Recovered	Recovery (%)	Comments
190-1175A-								
1H	23	1105	0.0	7.2	7.2	7.12	98.9	WSTP at 3006.8 m
2H	23	1200	7.2	16.7	9.5	8.92	93.9	
3H	23	1320	16.7	26.2	9.5	9.70	102.1	Tensor started at 12:00
4H	23	1425	26.2	35.7	9.5	9.81	103.3	
5H	23	1515	35.7	45.2	9.5	9.34	98.3	Whirl-Pak, tracers
6H	23	1600	45.2	54.7	9.5	10.01	105.4	Whirl-Pak, tracers
7H	23	1655	54.7	64.2	9.5	9.57	100.7	
8H	23	1745	64.2	73.7	9.5	9.65	101.6	
9H	23	1845	73.7	83.2	9.5	9.62	101.3	
10H	23	1950	83.2	92.7	9.5	7.71	81.2	Tensor at 19:45
11H	23	2050	92.7	95.0	2.3	2.32	100.9	
120	23	2115	95.0	100.8	NA	NA	NA	Drilled without coring
12H	23	2200	100.8	110.3	9.5	9.58	100.8	
13H	23	2300	110.3	119.8	9.5	10.05	105.8	
14H	23	2355	119.8	129.3	9.5	9.77	102.8	Adara drill over 3 m
15H	24	0050	129.3	138.8	9.5	10.02	105.5	
16H	24	0145	138.8	148.3	9.5	9.50	100.0	
17H	24	0245	148.3	157.8	9.5	9.53	100.3	DVTP
18H	24	0535	157.8	167.3	9.5	8.33	87.7	Tensor in at 04:45
19H	24	0625	167.3	176.8	9.5	10.08	106.1	
20H	24	0715	176.8	186.3	9.5	8.73	91.9	
21H	24	0820	186.3	195.8	9.5	9.49	99.9	
22H	24	0935	195.8	205.3	9.5	8.83	92.9	Drill over 3 m
23X	24	1120	205.3	215.0	9.7	9.73	100.3	DVTP at 3224.1 m
24X	24	1410	215.0	224.6	9.6	0.00	0.0	
25X	24	1510	224.6	234.3	9.7	8.57	88.4	
26X	24	1640	234.3	243.9	9.6	9.81	102.2	
27X	24	1755	243.9	253.6	9.7	9.81	101.1	
28X	24	1915	253.6	263.2	9.6	9.61	100.1	
29X	24	2025	263.2	272.8	9.6	9.96	103.7	DVTP at 3281.9 m (272.8 mbsf)
30X	24	2320	272.8	282.4	9.6	7.50	78.1	
31X	25	0040	282.4	292.0	9.6	8.06	84.0	
32X	25	0145	292.0	301.6	9.6	8.99	93.6	
33X	25	0250	301.6	311.2	9.6	9.85	102.6	
34X	25	0400	311.2	320.8	9.6	0.01	0.1	
35X	25	0520	320.8	330.4	9.6	0.12	1.2	
36X	25	0645	330.4	340.0	9.6	0.30	3.1	
37X	25	0830	340.0	349.6	9.6	9.24	96.2	
38X	25	0950	349.6	359.2	9.6	5.49	57.2	
39X	25	1110	359.2	368.8	9.6	3.40	35.4	
40X	25	1250	368.8	378.4	9.6	0.45	4.7	
41X	25	1445	378.4	388.0	9.6	7.45	77.6	
42X	25	1600	388.0	397.6	9.6	4.71	49.1	
43X	25	1800	397.6	406.5	8.9	4.71	52.9	Hard at 405.3 mbsf
44X	25	1955	406.5	416.2	9.7	1.24	12.8	Sinker bars out
45X	25	2145	416.2	425.8	9.6	0.00	0.0	No recovery
46X	25	2335	425.8	435.4	9.6	0.02	0.2	
47X	26	0115	435.4	435.7	9.6	0.30	3.1	
				Totals:	439.2	327.01	74.5	

Notes: DVTP = Davis-Villinger temperature probe, WSTP = water-sampling temperature probe. NA = not applicable.

Table T2. Coring summary by section, Site 1175. (**See table notes.** Continued on next five pages.)

Core	Date (June 2000)	Time (local)	Core depth (mbsf) Top	Core depth (mbsf) Bottom	Length (m) Cored	Length (m) Recovered	Recovery (%)	Section	Length (m) Liner	Length (m) Curated	Section depth (mbsf) Top	Section depth (mbsf) Bottom	Catwalk samples
190-1175A-													
1H	23	1105	0.0	7.2	7.2	7.12	98.9						
								1	1.5	1.5	0.0	1.5	IW, BACT, WRS, WRY
								2	1.5	1.5	1.5	3.0	IW
								3	1.5	1.5	3.0	4.5	IW
								4	1.5	1.5	4.5	6.0	IW
								5	0.78	0.78	6.0	6.78	IW, HS, BGAS, BGAS
								6	0.12	0.12	6.78	6.9	
								CC(w/6)	0.22	0.22	6.9	7.12	PAL
								Totals:	7.12	7.12			
2H	23	1200	7.2	16.7	9.5	8.92	93.9						
								1	1.5	1.5	7.2	8.7	BACT, IW
								2	1.5	1.5	8.7	10.2	WRS, IW, HS
								3	1.5	1.5	10.2	11.7	IW
								4	1.5	1.5	11.7	13.2	IW, HS, BGAS
								5	1.5	1.5	13.2	14.7	BACT, IW
								6	1.0	1.0	14.7	15.7	IW
								7	0.15	0.15	15.7	15.85	
								CC(w/7)	0.27	0.27	15.85	16.12	PAL
								Totals:	8.92	8.92			
3H	23	1320	16.7	26.2	9.5	9.70	102.1						
								1	1.5	1.5	16.7	18.2	IW
								2	1.5	1.5	18.2	19.7	HS, BGAS
								3	1.5	1.5	19.7	21.2	BACT, IW
								4	1.5	1.5	21.2	22.7	IW, BGAS
								5	1.5	1.5	22.7	24.2	
								6	1.5	1.5	24.2	25.7	BGAS, IW
								7	0.47	0.47	25.7	26.17	
								CC(w/7)	0.23	0.23	26.17	26.4	PAL
								Totals:	9.7	9.7			
4H	23	1425	26.2	35.7	9.5	9.81	103.3						
								1	1.5	1.5	26.2	27.7	
								2	1.5	1.5	27.7	29.2	BGAS, IW
								3	1.5	1.5	29.2	30.7	
								4	1.5	1.5	30.7	32.2	BACT, IW
								5	1.5	1.5	32.2	33.7	BGAS
								6	1.5	1.5	33.7	35.2	HS, IW
								7	0.48	0.48	35.2	35.68	
								CC(w/7)	0.33	0.33	35.68	36.01	PAL
								Totals:	9.81	9.81			
5H	23	1515	35.7	45.2	9.5	9.34	98.3						
								1	1.5	1.5	35.7	37.2	
								2	1.5	1.5	37.2	38.7	BACT, IW
								3	1.5	1.5	38.7	40.2	
								4	1.5	1.5	40.2	41.7	BGAS
								5	1.5	1.5	41.7	43.2	HS, IW
								6	1.5	1.5	43.2	44.7	
								CC(w/CC)	0.34	0.34	44.7	45.04	PAL
								Totals:	9.34	9.34			
6H	23	1600	45.2	54.7	9.5	10.01	105.4						
								1	1.5	1.5	45.2	46.7	WRS
								2	1.5	1.5	46.7	48.2	HS
								3	1.5	1.5	48.2	49.7	WRS
								4	1.5	1.5	49.7	51.2	WRY, WRS, IW, BACT
								5	1.5	1.5	51.2	52.7	WRS, HS, BGAS, VAC
								6	1.5	1.5	52.7	54.2	
								7	0.69	0.69	54.2	54.89	
								CC(w/7)	0.32	0.32	54.89	55.21	PAL
								Totals:	10.01	10.01			
7H	23	1655	54.7	64.2	9.5	9.57	100.7						
								1	1.5	1.5	54.7	56.2	
								2	1.5	1.5	56.2	57.7	WRSR
								3	1.5	1.5	57.7	59.2	BACT, IW
								4	1.5	1.5	59.2	60.7	HS
								5	1.5	1.5	60.7	62.2	
								6	1.5	1.5	62.2	63.7	
								7	0.43	0.43	63.7	64.13	
								CC(w/7)	0.14	0.14	64.13	64.27	PAL
								Totals:	9.57	9.57			

Table T2 (continued).

Core	Date (June 2000)	Time (local)	Core depth (mbsf) Top	Core depth (mbsf) Bottom	Length (m) Cored	Length (m) Recovered	Recovery (%)	Section	Length (m) Liner	Length (m) Curated	Section depth (mbsf) Top	Section depth (mbsf) Bottom	Catwalk samples
8H	23	1745	64.2	73.7	9.5	9.65	101.6						
								1	1.5	1.5	64.2	65.7	
								2	1.5	1.5	65.7	67.2	
								3	1.5	1.5	67.2	68.7	IW
								4	1.5	1.5	68.7	70.2	HS
								5	1.5	1.5	70.2	71.7	
								6	1.5	1.5	71.7	73.2	
								7	0.49	0.49	73.2	73.69	
								CC(w/7)	0.16	0.16	73.69	73.85	PAL
								Totals:	9.65	9.65			
9H	23	1845	73.7	83.2	9.5	9.62	101.3						
								1	1.5	1.5	73.7	75.2	
								2	1.5	1.5	75.2	76.7	
								3	1.5	1.5	76.7	78.2	IW, BACT, IW
								4	1.5	1.5	78.2	79.7	HS, HS
								5	1.5	1.5	79.7	81.2	
								6	1.5	1.5	81.2	82.7	
								7	0.24	0.24	82.7	82.94	
								CC(w/7)	0.38	0.38	82.94	83.32	PAL
								Totals:	9.62	9.62			
10H	23	1950	83.2	92.7	9.5	7.71	81.2						
								1	1.5	1.5	83.2	84.7	
								2	1.5	1.5	84.7	86.2	IW
								3	1.5	1.5	86.2	87.7	HS
								4	1.5	1.5	87.7	89.2	
								5	1.5	1.5	89.2	90.7	PAL
								6	0.12	0.12	90.7	90.82	
								CC(w/6)	0.09	0.09	90.82	90.91	PAL
								Totals:	7.71	7.71			
11H	23	2050	92.7	95.0	2.3	2.32	100.9						
								1	1.5	1.5	92.7	94.2	HS
								2	0.64	0.64	94.2	94.84	
								CC(w/2)	0.18	0.18	94.84	95.02	PAL
								Totals:	2.32	2.32			
120	23	2115	95.0	100.8	NA	NA	NA	**** Drilled without coring ****					
12H	23	2200	100.8	110.3	9.5	9.58	100.8						
								1	1.5	1.5	100.8	102.3	
								2	1.5	1.5	102.3	103.8	HS
								3	1.5	1.5	103.8	105.3	
								4	1.5	1.5	105.3	106.8	IW, WRY, WRS, BACT
								5	1.5	1.5	106.8	108.3	
								6	1.5	1.5	108.3	109.8	
								7	0.34	0.34	109.8	110.14	
								CC(w/7)	0.24	0.24	110.14	110.38	PAL
								Totals:	9.58	9.58			
13H	23	2300	110.3	119.8	9.5	10.05	105.8						
								1	1.5	1.5	110.3	111.8	
								2	1.5	1.5	111.8	113.3	
								3	1.5	1.5	113.3	114.8	
								4	1.5	1.5	114.8	116.3	HS, IW
								5	1.5	1.5	116.3	117.8	
								6	1.5	1.5	117.8	119.3	
								7	0.75	0.75	119.3	120.05	
								CC(w/7)	0.3	0.3	120.05	120.35	PAL
								Totals:	10.05	10.05			
14H	23	2355	119.8	129.3	9.5	9.77	102.8						
								1	1.5	1.5	119.8	121.3	
								2	1.5	1.5	121.3	122.8	
								3	1.5	1.5	122.8	124.3	
								4	1.5	1.5	124.3	125.8	HS, BGAS
								5	1.5	1.5	125.8	127.3	IW
								6	1.5	1.5	127.3	128.8	
								7	0.37	0.37	128.8	129.17	
								CC(w/7)	0.4	0.4	129.17	129.57	PAL
								Totals:	9.77	9.77			
15H	24	0050	129.3	138.8	9.5	10.02	105.5						
								1	1.5	1.5	129.3	130.8	

Table T2 (continued).

Core	Date (June 2000)	Time (local)	Core depth (mbsf) Top	Core depth (mbsf) Bottom	Length (m) Cored	Length (m) Recovered	Recovery (%)	Section	Length (m) Liner	Length (m) Curated	Section depth (mbsf) Top	Section depth (mbsf) Bottom	Catwalk samples
								2	1.5	1.5	130.8	132.3	
								3	1.5	1.5	132.3	133.8	
								4	1.5	1.5	133.8	135.3	IW, BACT
								5	1.5	1.5	135.3	136.8	HS
								6	1.5	1.5	136.8	138.3	
								7	0.75	0.75	138.3	139.05	
								CC(w/7)	0.27	0.27	139.05	139.32	PAL
								Totals:	10.02	10.02			
16H	24	0145	138.8	148.3	9.5	9.50	100						
								1	1.5	1.5	138.8	140.3	
								2	1.5	1.5	140.3	141.8	
								3	1.5	1.5	141.8	143.3	
								4	1.5	1.5	143.3	144.8	IW
								5	1.5	1.5	144.8	146.3	HS
								6	1.5	1.5	146.3	147.8	
								7	0.5	0.5	147.8	148.3	PAL
								Totals:	9.5	9.5			
17H	24	0245	148.3	157.8	9.5	9.53	100.3						
								1	1.5	1.5	148.3	149.8	
								2	1.5	1.5	149.8	151.3	HS, BGAS
								3	1.5	1.5	151.3	152.8	
								4	1.5	1.5	152.8	154.3	IW
								5	1.5	1.5	154.3	155.8	
								6	1.5	1.5	155.8	157.3	
								7	0.52	0.52	157.3	157.82	
								CC(NS)	0.01	0.01	157.82	157.83	All to PAL
								Totals:	9.53	9.53			
18H	24	0535	157.8	167.3	9.5	8.33	87.7						
								1	1.5	1.5	157.8	159.3	
								2	1.5	1.5	159.3	160.8	HS
								3	1.5	1.5	160.8	162.3	
								4	1.5	1.5	162.3	163.8	IW
								5	1.5	1.5	163.8	165.3	
								6	0.57	0.57	165.3	165.87	
								CC(w/6)	0.26	0.26	165.87	166.13	PAL
								Totals:	8.33	8.33			
19H	24	0625	167.3	176.8	9.5	10.08	106.1						
								1	1.5	1.5	167.3	168.8	
								2	1.5	1.5	168.8	170.3	
								3	1.5	1.5	170.3	171.8	
								4	1.5	1.5	171.8	173.3	IW
								5	1.5	1.5	173.3	174.8	HS
								6	1.5	1.5	174.8	176.3	
								7	0.88	0.88	176.3	177.18	
								CC(w/CC)	0.2	0.2	177.18	177.38	PAL
								Totals:	10.08	10.08			
20H	24	0715	176.8	186.3	9.5	8.73	91.9						
								1	1.5	1.5	176.8	178.3	
								2	1.5	1.5	178.3	179.8	
								3	1.5	1.5	179.8	181.3	
								4	1.5	1.5	181.3	182.8	IW
								5	1.5	1.5	182.8	184.3	HS, BGAS
								6	1.22	1.22	184.3	185.52	
								CC(w/6)	0.01	0.01	185.52	185.53	All to PAL
								Totals:	8.73	8.73			
21H	24	0820	186.3	195.8	9.5	9.49	99.9						
								1	1.5	1.5	186.3	187.8	
								2	1.5	1.5	187.8	189.3	
								3	1.5	1.5	189.3	190.8	
								4	1.5	1.5	190.8	192.3	IW
								5	1.5	1.5	192.3	193.8	HS, WRY, WRS, BACT
								6	1.5	1.5	193.8	195.3	
								7	0.48	0.48	195.3	195.78	
								CC(w/7)	0.01	0.01	195.78	195.79	All to PAL
								Totals:	9.49	9.49			
22H	24	0935	195.8	205.3	9.5	8.83	92.9						
								1	1.5	1.5	195.8	197.3	
								2	1.5	1.5	197.3	198.8	HS

Table T2 (continued).

Core	Date (June 2000)	Time (local)	Core depth (mbsf) Top	Core depth (mbsf) Bottom	Length (m) Cored	Length (m) Recovered	Recovery (%)	Section	Length (m) Liner	Length (m) Curated	Section depth (mbsf) Top	Section depth (mbsf) Bottom	Catwalk samples
								3	1.5	1.5	198.8	200.3	
								4	1.5	1.5	200.3	201.8	IW
								5	1.5	1.5	201.8	203.3	
								6	1.14	1.14	203.3	204.44	
								CC(w/6)	0.19	0.19	204.44	204.63	PAL
								Totals:	8.83	8.83			
23X	24	1120	205.3	215.0	9.7	9.73	100.3						
								1	1.5	1.5	205.3	206.8	
								2	1.5	1.5	206.8	208.3	
								3	1.5	1.5	208.3	209.8	
								4	1.13	1.13	209.8	210.93	IW
								5	1.5	1.5	210.93	212.43	HS, BGAS
								6	1.5	1.5	212.43	213.93	
								7	0.58	0.58	213.93	214.51	
								CC(w/7)	0.52	0.52	214.51	215.03	PAL
								Totals:	9.73	9.73			
24X	24	1410	215.0	224.6	9.6	0.00	0						
								1	0.0	0.0			
								Totals:	0.0	0.0			
25X	24	1510	224.6	234.3	9.7	8.57	88.4						
								1	1.5	1.5	224.6	226.1	
								2	1.5	1.5	226.1	227.6	BGAS
								3	1.5	1.5	227.6	229.1	BACT, IW
								4	1.5	1.5	229.1	230.6	HS
								5	1.5	1.5	230.6	232.1	
								6	0.68	0.68	232.1	232.78	
								CC(w/6)	0.39	0.39	232.78	233.17	PAL
								Totals:	8.57	8.57			
26X	24	1640	234.3	243.9	9.6	9.81	102.2						
								1	1.5	1.5	234.3	235.8	
								2	1.5	1.5	235.8	237.3	
								3	1.5	1.5	237.3	238.8	WRSR
								4	1.5	1.5	238.8	240.3	IW
								5	1.5	1.5	240.3	241.8	HS
								6	1.5	1.5	241.8	243.3	
								7	0.46	0.46	243.3	243.76	
								CC(w/7)	0.35	0.35	243.76	244.11	PAL
								Totals:	9.81	9.81			
27X	24	1755	243.9	253.6	9.7	9.81	101.1						
								1	1.5	1.5	243.9	245.4	
								2	1.5	1.5	245.4	246.9	
								3	1.5	1.5	246.9	248.4	
								4	1.5	1.5	248.4	249.9	IW
								5	1.5	1.5	249.9	251.4	HS
								6	1.5	1.5	251.4	252.9	
								7	0.39	0.39	252.9	253.29	
								CC(w/7)	0.42	0.42	253.29	253.71	PAL
								Totals:	9.81	9.81			
28X	24	1915	253.6	263.2	9.6	9.61	100.1						
								1	1.5	1.5	253.6	255.1	
								2	1.5	1.5	255.1	256.6	
								3	1.5	1.5	256.6	258.1	
								4	1.5	1.5	258.1	259.6	
								5	1.5	1.5	259.6	261.1	IW
								6	1.5	1.5	261.1	262.6	HS
								7	0.26	0.26	262.6	262.86	
								CC(w/7)	0.35	0.35	262.86	263.21	PAL
								Totals:	9.61	9.61			
29X	24	2025	263.2	272.8	9.6	9.96	103.8						
								1	1.5	1.5	263.2	264.7	
								2	1.5	1.5	264.7	266.2	
								3	1.5	1.5	266.2	267.7	
								4	1.5	1.5	267.7	269.2	
								5	1.5	1.5	269.2	270.7	BACT, IW
								6	1.5	1.5	270.7	272.2	HS
								7	0.5	0.5	272.2	272.7	
								CC(w/7)	0.46	0.46	272.7	273.16	PAL
								Totals:	9.96	9.96			

Table T2 (continued).

Core	Date (June 2000)	Time (local)	Core depth (mbsf) Top	Core depth (mbsf) Bottom	Length (m) Cored	Length (m) Recovered	Recovery (%)	Section	Length (m) Liner	Length (m) Curated	Section depth (mbsf) Top	Section depth (mbsf) Bottom	Catwalk samples
30X	24	2320	272.8	282.4	9.6	7.50	78.1						
								1	1.5	1.5	272.8	274.3	
								2	1.5	1.5	274.3	275.8	IW, BGAS
								3	1.5	1.5	275.8	277.3	HS
								4	1.5	1.5	277.3	278.8	
								5	1.12	1.12	278.8	279.92	
								CC(w/CC)	0.38	0.38	279.92	280.3	PAL
								Totals:	7.5	7.5			
31X	25	0040	282.4	292.0	9.6	8.06	84						
								1	1.5	1.5	282.4	283.9	
								2	1.5	1.5	283.9	285.4	
								3	1.5	1.5	285.4	286.9	HS
								4	1.5	1.5	286.9	288.4	IW
								5	1.5	1.5	288.4	289.9	
								6	0.23	0.23	289.9	290.13	
								CC(w/6)	0.33	0.33	290.13	290.46	PAL
								Totals:	8.06	8.06			
32X	25	0145	292.0	301.6	9.6	8.99	93.6						
								1	1.5	1.5	292	293.5	
								2	1.5	1.5	293.5	295	HS, BGAS
								3	1.5	1.5	295	296.5	IW
								4	1.5	1.5	296.5	298	
								5	1.5	1.5	298	299.5	WRY, WRS, BACT
								6	1.16	1.16	299.5	300.66	
								CC(w/CC)	0.33	0.33	300.66	300.99	PAL
								Totals:	8.99	8.99			
33X	25	0250	301.6	311.2	9.6	9.85	102.6						
								1	1.5	1.5	301.6	303.1	
								2	1.5	1.5	303.1	304.6	IW
								3	1.5	1.5	304.6	306.1	
								4	1.5	1.5	306.1	307.6	
								5	1.5	1.5	307.6	309.1	HS
								6	1.5	1.5	309.1	310.6	
								7	0.48	0.48	310.6	311.08	
								CC(w/7)	0.37	0.37	311.08	311.45	PAL
								Totals:	9.85	9.85			
34X	25	0400	311.2	320.8	9.6	0.01	0.1						
								CC(w/CC)	0.01	0.01	311.2	311.21	PAL
								Totals:	0.01	0.01			
35X	25	0520	320.8	330.4	9.6	0.12	1.3						
								CC(w/CC)	0.12	0.12	320.8	320.92	
								Totals:	0.12	0.12			
36X	25	0645	330.4	340.0	9.6	0.30	3.1						
								CC(w/CC)	0.3	0.3	330.4	330.7	PAL
								Totals:	0.3	0.3			
37X	25	0830	340.0	349.6	9.6	9.24	96.3						
								1	1.5	1.5	340.0	341.5	
								2	1.5	1.5	341.5	343.0	
								3	1.5	1.5	343.0	344.5	
								4	1.5	1.5	344.5	346.0	BACT, IW
								5	1.5	1.5	346.0	347.5	HS, BGAS
								6	1.22	1.22	347.5	348.72	
								CC(w/CC)	0.52	0.52	348.72	349.24	PAL
								Totals:	9.24	9.24			
38X	25	0950	349.6	359.2	9.6	5.49	57.2						
								1	1.5	1.5	349.6	351.1	
								2	1.5	1.5	351.1	352.6	IW
								3	1.5	1.5	352.6	354.1	HS, BGAS
								4	0.76	0.76	354.1	354.86	
								CC(w/4)	0.23	0.23	354.86	355.09	PAL
								Totals:	5.49	5.49			
39X	25	1110	359.2	368.8	9.6	3.40	35.4						
								1	1.5	1.5	359.2	360.7	HS, BGAS
								2	1.5	1.5	360.7	362.2	IW
								3	0.22	0.22	362.2	362.42	
								CC(w/3)	0.18	0.18	362.42	362.6	
								Totals:	3.4	3.4			

Table T2 (continued).

Core	Date (June 2000)	Time (local)	Core depth (mbsf) Top	Core depth (mbsf) Bottom	Length (m) Cored	Length (m) Recovered	Recovery (%)	Section	Length (m) Liner	Length (m) Curated	Section depth (mbsf) Top	Section depth (mbsf) Bottom	Catwalk samples
40X	25	1250	368.8	378.4	9.6	0.45	4.7						
								CC(w/CC)	0.45	0.45	368.8	369.25	HS, PAL
								Totals:	0.45	0.45			
41X	25	1445	378.4	388.0	9.6	7.45	77.6						
								1	1.5	1.5	378.4	379.9	
								2	1.5	1.5	379.9	381.4	BACT, IW
								3	1.5	1.5	381.4	382.9	HS
								4	1.5	1.5	382.9	384.4	
								5	1.03	1.03	384.4	385.43	
								CC(w/5)	0.42	0.42	385.43	385.85	PAL
								Totals:	7.45	7.45			
42X	25	1600	388.0	397.6	9.6	4.71	49.1						
								1	1.5	1.5	388	389.5	
								2	1.5	1.5	389.5	391	HS, IW, BGAS
								3	1.3	1.3	391	392.3	
								CC(w/CC)	0.41	0.41	392.3	392.71	
								Totals:	4.71	4.71			
43X	25	1800	397.6	406.5	8.9	4.71	52.9						
								1	1.5	1.5	397.6	399.1	
								2	1.5	1.5	399.1	400.6	WRY, BACT, WRS, IW
								3	1.31	1.31	400.6	401.91	HS
								CC(w/CC)	0.4	0.4	401.91	402.31	PAL
								Totals:	4.71	4.71			
44X	25	1955	406.5	416.2	9.7	1.24	12.8						
								1	0.87	0.87	406.5	407.37	HS
								CC(w/1)	0.37	0.37	407.37	407.74	
								Totals:	1.24	1.24			
45X	25	2145	416.2	425.8	9.6	0.00	0						
								1	0.0	0.0			
	25							Totals:	0.0	0.0			
46X		2335	425.8	435.4	9.6	0.02	0.2						
								CC(w/CC)	0.02	0.02	425.8	425.82	
								Totals:	0.02	0.02			
47X	26	115	435.4	435.7	9.6	0.30	3.1						
								CC(w/CC)	0.3	0.3	435.4	435.7	PAL
								Totals:	0.3	0.3			
				Totals:	439.2	327.01	74.5						

Notes: Catwalk samples: IW = interstitial water, HS = headspace, PAL = paleontology, VAC = vacutainer. All other abbreviations are sample codes for postcruise research (see the "Sample Codes" database query). CC = core catcher (number in parenthesis indicates which section the core catcher is stored with). NA = not applicable. This table is also available in ASCII format.

Table T3. Summary of stratigraphic relations, Hole 1175A.

Unit	Facies name	Interval (cm) Top	Interval (cm) Bottom	Depth (mbsf) Top	Depth (mbsf) Bottom	Thickness (m)	Stratigraphic age	Lithologic description	Processes of formation
I	Upper slope basin	190-1175A-1H-1, 0	190-1175A-25X-1, 15	0.00	224.75	224.75	Quaternary	Hemipelagic (nannofossil-rich) mud, volcanic ash, sand to silt turbidites, soft-sediment folding disruption	Hemipelagic settling, volcanic ash falls, turbidity currents, submarine slumps
II	Middle slope basin	25X-1, 15	33X-1, 4	224.75	301.64	76.89	Quaternary	Hemipelagic mud, muddy sand to sandy mud, sporadic silt turbidites, volcanic ash	Hemipelagic settling, sandy mudflows, volcanic ash falls, infrequent turbidity currents
III	Slope to prism transition	33X-1, 4	147X-CC, 30	301.64	435.70	134.06	Quaternary	Hemipelagic mudstone, pebbly mudstone, abundant sand to silt turbidites, rare volcanic ash	Hemipelagic settling, debris flows, frequent turbidity currents, volcanic ash falls

Table T4. Peak intensities and peak areas from X-ray diffraction analysis of bulk-powder sediment samples, Hole 1175A. (Continued on next page.)

Core, section, interval (cm)	Depth (mbsf)	X-ray diffraction peak intensity (cps)								X-ray diffraction peak area (total counts)							
		Smectite + chlorite	Illite	Chlorite + kaolinite	(101) Quartz	Plagioclase	Calcite	(100) Quartz	(101) Cristobalite	Smectite + chlorite	Illite	Chlorite + kaolinite	(101) Quartz	Plagioclase	Calcite	(100) Quartz	(101) Cristobalite
190-1175A-																	
1H-2, 139-140	2.89	35	88	80	1,069	233	286	192	100	1,050	1,463	1,165	14,292	5,579	3,612	2,918	1,439
1H-4, 137-138	5.87	50	114	120	1,740	426	584	316	88	2,308	2,317	2,189	23,548	10,288	7,951	4,239	1,231
1H-5, 69-70	6.69	52	101	112	1,833	334	630	283	95	2,343	2,098	1,903	23,642	8,289	8,248	3,750	1,240
2H-1, 136-137	8.56	39	88	86	1,925	333	499	314	98	1,670	2,187	1,797	24,282	8,706	6,873	4,019	1,290
2H-3, 137-138	11.57	43	82	94	1,708	293	709	293	88	1,867	2,019	1,698	22,820	7,748	9,655	3,730	1,158
2H-5, 137-138	14.57	55	99	103	1,793	292	610	291	92	2,296	2,146	2,055	23,739	8,205	8,258	3,793	1,111
3H-1, 136-137	18.06	43	85	93	1,468	291	740	270	93	1,781	1,809	1,843	19,568	7,058	9,816	3,495	1,370
3H-3, 136-137	21.06	49	98	118	1,729	385	690	282	85	1,996	2,118	2,042	22,474	9,176	9,205	3,799	1,257
4H-2, 138-139	29.08	45	96	110	1,819	315	587	292	86	2,314	2,315	2,081	23,647	8,005	8,111	3,795	1,193
4H-4, 137-138	32.07	45	98	106	1,625	335	421	295	85	1,857	2,101	1,995	21,492	8,795	6,242	3,652	1,282
4H-6, 139-140	35.09	55	104	111	1,867	338	536	278	80	2,156	2,592	2,054	24,519	8,577	7,108	3,947	956
5H-2, 138-139	38.58	54	105	113	1,812	286	488	333	83	1,987	2,510	2,222	24,057	8,063	6,615	4,235	1,151
5H-5, 138-139	43.08	69	107	127	1,771	299	552	311	91	2,672	2,408	2,099	23,656	8,821	7,673	4,098	1,191
6H-4, 110-111	50.80	54	96	98	1,537	258	1,283	263	61	2,316	2,258	1,718	19,943	6,739	16,809	3,410	906
7H-2, 128-129	57.48	55	106	105	1,957	341	337	305	83	2,229	2,328	2,130	26,845	8,667	4,830	4,046	1,072
7H-3, 78-79	58.48	25	29	25	1,532	185	170	141	70	1,329	603	562	16,877	5,801	2,542	2,376	2,220
7H-4, 30-31	59.50	25	45	73	6,066	711	66	1,023	129	1,112	1,008	1,144	68,754	17,980	1,051	11,279	1,546
8H-3, 122-123	68.42	53	115	113	1,669	350	653	297	76	2,057	2,260	2,090	23,177	8,017	9,311	3,837	1,113
9H-3, 132-133	78.02	36	78	81	1,560	323	808	256	89	1,784	1,943	1,571	20,954	7,554	10,733	3,314	1,178
9H-5, 10-11	79.80	54	82	89	1,476	259	1,077	272	106	1,979	2,094	1,647	19,508	7,055	14,010	3,313	1,278
9H-6, 146-147	82.66	41	66	78	1,323	317	973	227	78	1,504	1,717	1,519	17,918	6,888	12,999	3,060	959
10H-2, 133-134	86.03	54	105	106	1,583	263	695	273	87	1,773	2,259	2,092	21,055	7,334	9,322	3,510	1,192
12H-4, 105-106	106.35	50	115	108	1,915	318	611	300	80	1,950	2,685	2,131	25,044	8,297	8,161	3,886	1,080
13H-4, 131-132	116.11	42	97	101	1,547	295	954	263	88	1,845	2,139	2,035	20,649	7,812	12,141	3,314	1,091
14H-5, 135-136	127.15	46	76	87	1,311	297	1,426	226	73	1,889	1,599	1,575	17,273	7,470	18,319	3,000	1,005
15H-3, 136-137	133.66	42	84	89	1,667	297	781	272	96	2,017	1,976	1,802	21,867	8,324	10,074	3,463	1,235
16H-1, 78-79	139.58	38	73	85	1,484	244	1,204	281	78	1,563	1,701	1,684	20,325	6,929	15,670	3,513	1,038
16H-3, 132-133	143.12	31	57	65	1,171	175	2,025	175	61	1,964	1,416	1,384	14,541	4,495	25,624	2,366	782
17H-3, 142-143	152.72	44	91	95	1,575	295	1,102	285	72	2,420	2,050	1,784	20,486	7,369	14,507	3,639	918
18H-3, 142-143	162.22	40	61	69	1,344	245	1,531	234	65	1,775	1,433	1,369	17,535	5,889	19,475	3,123	825
19H-4, 133-134	173.13	43	76	87	1,637	278	1,063	301	79	1,597	1,654	1,763	20,965	7,506	13,642	3,812	1,011
20H-4, 135-136	182.65	40	75	90	1,570	273	1,147	295	78	1,649	1,771	1,932	20,302	6,990	14,954	3,711	1,082
21H-4, 135-136	192.15	47	88	88	1,559	281	950	245	72	1,848	2,174	1,635	20,296	7,794	12,305	3,346	912
22H-4, 142-143	201.72	36	101	99	1,496	287	985	315	77	1,877	1,898	1,975	19,819	7,079	12,690	3,985	1,027
23X-3, 67-68	208.97	44	90	100	1,696	340	1,165	273	88	2,325	2,203	1,960	22,289	8,365	15,178	3,549	1,141
23X-4, 91-92	210.71	41	69	81	1,306	235	1,229	254	84	1,332	1,198	1,531	16,970	7,172	15,704	3,264	1,294
23X-7, 52-53	214.45	24	68	64	887	204	1,702	176	59	1,838	1,406	1,181	11,960	11,509	22,114	2,376	1,018
25X-3, 126-127	228.86	54	90	104	1,550	264	550	275	80	2,155	2,645	1,867	21,148	7,820	7,094	3,571	1,170
26X-3, 127-128	238.57	45	80	78	1,388	275	1,290	244	72	2,421	1,787	1,527	18,759	7,318	16,735	3,369	1,029
26X-4, 128-129	240.08	50	75	97	1,837	260	964	267	78	2,350	2,158	1,811	23,092	7,263	12,575	3,353	1,117
27X-4, 120-121	249.60	37	64	82	1,479	236	1,245	254	167	1,555	1,299	1,952	19,436	6,446	16,087	3,529	2,053
28X-2, 116-117	256.26	48	86	97	1,552	347	706	306	79	1,840	1,924	1,836	20,715	8,365	9,462	3,890	1,354
28X-5, 119-120	260.79	53	85	85	1,714	264	816	261	72	3,057	1,792	1,838	21,829	8,191	10,715	3,467	1,255
28X-6, 48-49	261.58	64	129	133	1,983	407	728	304	94	1,978	2,540	2,601	25,716	11,067	9,550	4,046	1,038
29X-5, 119-120	270.39	56	107	108	1,601	308	1,125	298	86	2,428	2,034	1,953	21,283	7,874	14,425	3,681	1,073
30X-2, 113-114	275.43	56	90	95	1,392	245	1,279	279	66	2,642	2,179	1,874	18,724	6,202	16,911	3,447	1,246
31X-4, 119-120	288.09	48	92	103	1,751	293	640	301	81	2,260	2,024	2,064	23,146	8,237	8,734	4,160	1,074

Table T4 (continued).

Core, section, interval (cm)	Depth (mbsf)	X-ray diffraction peak intensity (cps)								X-ray diffraction peak area (total counts)							
		Smectite + chlorite	Illite	Chlorite + kaolinite	(101) Quartz	Plagioclase	Calcite	(100) Quartz	(101) Cristobalite	Smectite + chlorite	Illite	Chlorite + kaolinite	(101) Quartz	Plagioclase	Calcite	(100) Quartz	(101) Cristobalite
33X-2, 114-115	304.24	64	107	103	1,654	403	603	285	88	2,385	2,182	1,945	21,680	10,720	8,441	3,862	1,233
33X-3, 117-118	305.77	82	148	143	1,849	408	765	309	108	3,753	3,309	2,523	24,363	10,379	9,905	3,948	1,400
33X-5, 49-50	308.09	55	83	78	1,765	369	978	324	82	1,995	1,770	1,504	22,161	9,417	11,642	4,159	1,083
33X-6, 57-58	309.67	50	63	74	1,448	1,296	854	262	99	2,193	1,250	1,636	18,427	18,295	11,658	3,674	1,349
37X-4, 118-119	345.68	24	28	29	4,193	310	145	705	86	1,315	827	604	51,057	9,707	3,421	8,866	1,151
37X-5, 140-141	347.40	50	87	95	2,375	617	451	466	89	2,214	1,689	1,847	30,328	12,784	6,034	5,941	1,336
38X-2, 115-116	352.25	90	196	174	2,275	569	148	389	114	3,580	3,558	3,188	31,293	16,164	2,065	5,048	1,474
39X-2, 102-103	361.72	73	124	132	1,880	441	418	330	131	2,924	2,138	2,604	26,058	10,914	5,794	4,451	1,497
40X-CC, 20-21	369.00	56	100	115	2,341	443	195	379	271	2,368	1,865	2,917	30,433	10,498	3,138	5,053	2,757
41X-2, 106-107	380.96	71	101	119	1,899	479	210	337	107	3,112	2,266	2,257	24,953	12,056	2,938	4,537	1,679
42X-2, 111-112	390.61	64	113	125	2,855	504	356	506	91	2,859	2,232	2,669	33,787	12,636	5,007	6,128	1,104
43X-2, 69-70	399.79	54	99	114	2,139	423	200	415	98	2,645	2,246	2,142	27,263	11,158	2,967	5,169	1,395
43X-CC, 23-24	402.14	61	109	115	2,078	433	397	348	93	2,732	2,275	2,285	27,522	10,726	5,662	4,638	1,305
44X-1, 46-47	406.96	43	53	75	1,379	311	104	288	91	1,776	1,340	1,132	17,950	9,591	2,802	4,676	1,052
46X-CC, 1-2	425.81	69	161	212	2,129	485	127	382	87	2,406	2,795	3,640	29,231	10,917	2,289	5,168	1,239
47X-CC, 10-11	435.50	92	226	235	2,968	694	0	529	146	2,837	3,681	3,973	38,826	14,814	0	5,979	1,667

Table T5. Normalized relative mineral abundances based on X-ray diffraction analysis of random bulk-sediment powders, Hole 1175A. (Continued on next page.)

Unit	Core, section, interval (cm)	Depth (mbsf)	Normalized relative mineral abundance (wt%)				Peak area ratio: (101) Cristobalite/ (100) Quartz
			Total clay minerals	Quartz	Plagioclase	Calcite	
	190-1175A-						
	1H-2, 139-140	2.89	42	31	14	13	0.49
	1H-4, 137-138	5.87	40	29	14	17	0.29
	1H-5, 69-70	6.69	40	31	11	18	0.33
	2H-1, 136-137	8.56	39	32	13	16	0.32
	2H-3, 137-138	11.57	37	30	11	22	0.31
	2H-5, 137-138	14.57	40	31	11	18	0.29
	3H-1, 136-137	18.06	36	28	11	25	0.39
	3H-3, 136-137	21.06	38	29	13	21	0.33
	4H-2, 138-139	29.08	41	30	11	18	0.31
	4H-4, 137-138	32.07	41	30	14	15	0.35
	4H-6, 139-140	35.09	43	30	12	15	0.24
	5H-2, 138-139	38.58	43	31	12	15	0.27
	5H-5, 138-139	43.08	43	30	11	16	0.29
	6H-4, 110-111	50.80	35	23	8	34	0.27
	7H-2, 128-129	57.48	43	35	12	10	0.26
	7H-3, 78-79	58.48	33	43	15	9	0.93
	7H-4, 30-31	59.50	20	61	19	0	0.14
	8H-3, 122-123	68.42	39	29	11	21	0.29
I	9H-3, 132-133	78.02	36	28	11	26	0.36
	9H-5, 10-11	79.80	35	24	9	31	0.39
	9H-6, 146-147	82.66	32	24	11	33	0.31
	10H-2, 133-134	86.03	40	27	11	22	0.34
	12H-4, 105-106	106.35	42	30	11	17	0.28
	13H-4, 131-132	116.11	36	25	11	28	0.33
	14H-5, 135-136	127.15	29	21	10	40	0.34
	15H-3, 136-137	133.66	37	28	12	23	0.36
	16H-1, 78-79	139.58	30	25	10	36	0.30
	16H-3, 132-133	143.12	26	18	6	51	0.33
	17H-3, 142-143	152.72	36	25	9	30	0.25
	18H-3, 142-143	162.22	28	22	8	43	0.26
	19H-4, 133-134	173.13	31	26	11	32	0.27
	20H-4, 135-136	182.65	31	25	10	34	0.29
	21H-4, 135-136	192.15	36	25	11	28	0.27
	22H-4, 142-143	201.72	35	25	10	30	0.26
	23X-3, 67-68	208.97	35	25	10	30	0.32
	23X-4, 91-92	210.71	26	23	11	40	0.40
	23X-7, 52-53	214.45	25	15	14	46	0.43
	Mean Unit I:		36	28	11	25	0.33
	25X-3, 126-127	228.86	45	28	11	16	0.33
	26X-3, 127-128	238.57	33	23	9	35	0.31
	26X-4, 128-129	240.08	37	28	9	26	0.33
	27X-4, 120-121	249.60	27	25	10	39	0.58
	28X-2, 116-117	256.26	37	28	12	23	0.35
II	28X-5, 119-120	260.79	38	29	10	22	0.36
	28X-6, 48-49	261.58	38	28	14	19	0.26
	29X-5, 119-120	270.39	35	25	10	30	0.29
	30X-2, 113-114	275.43	36	22	7	34	0.36
	31X-4, 119-120	288.09	39	30	11	20	0.26
	Mean Unit II:		37	27	10	26	0.34
	33X-2, 114-115	304.24	40	28	14	18	0.32
	33X-3, 117-118	305.77	47	26	11	16	0.35
	33X-5, 49-50	308.09	33	28	13	26	0.26
	33X-6, 57-58	309.67	27	24	24	25	0.37
	37X-4, 118-119	345.68	24	59	12	5	0.13
	37X-5, 140-141	347.40	34	37	17	12	0.22
III	38X-2, 115-116	352.25	50	32	17	1	0.29
	39X-2, 102-103	361.72	42	33	14	11	0.34
	40X-CC, 20-21	369.00	39	40	15	5	0.55
	41X-2, 106-107	380.96	46	34	16	4	0.37
	42X-2, 111-112	390.61	39	38	15	8	0.18
	43X-2, 69-70	399.79	44	36	15	4	0.27
	43X-CC, 23-24	402.14	42	34	14	11	0.28

Table T5 (continued).

Unit	Core, section, interval (cm)	Depth (mbsf)	Normalized relative mineral abundance (wt%)				Peak area ratio: (101) Cristobalite/ (100) Quartz
			Total clay minerals	Quartz	Plagioclase	Calcite	
III	44X-1, 46-47	406.96	39	35	19	7	0.22
	46X-CC, 1-2	425.81	47	35	15	3	0.24
	47X-CC, 10-11	435.50	47	37	16	0	0.28
	Mean Unit III:		40	35	16	10	0

Table T6. Results of X-ray diffraction analysis of bulk-powder volcanic ash samples, Hole 1175A.

Core, section, interval (cm)	Depth (mbsf)	X-ray diffraction peak intensity (cps)												X-ray diffraction peak area (total counts)											
		Smectite	Illite	Chlorite	Clinoptilolite	Hornblende	Cristobalite	Quartz	Plagioclase	Calcite	Pyroxene	Halite	Pyrite	Smectite	Illite	Chlorite	Clinoptilolite	Hornblende	Cristobalite	Quartz	Plagioclase	Calcite	Pyroxene	Halite	Pyrite
190-1175A-																									
1H-2, 46-47	1.97	0	0	0	0	0	39	279	123	61	0	196	0	0	0	0	0	0	524	3468	2755	881	0	2619	0
3H-5, 127-128	23.98	27	24	21	0	0	30	439	104	189	21	226	28	1343	463	339	0	0	639	5626	3176	2582	426	3150	336
8H-7, 33-34	74.03	0	0	0	0	0	0	401	468	232	88	162	54	0	0	0	0	0	0	4849	12711	3315	1576	2807	677
11H-2, 41-42	95.26	0	0	0	0	0	24	146	278	24	16	309	0	0	0	0	0	0	497	1716	4409	354	323	4367	0
23X-CC, 16-17	214.68	19	17	24	0	0	45	304	76	515	0	79	0	1041	554	496	0	0	716	4010	1715	6560	0	1431	0
41X-4, 52-53	383.43	20	31	24	0	142	255	569	249	161	42	116	0	1348	487	475	0	1363	3470	7000	6236	1923	697	2327	0

Table T7. Structural data, Hole 1175A. (See table note. Continued on next two pages.)

Core, section, interval (cm)	Depth (mbsf)	Cr az. (°)	Cr dip (°)	Cr line	Cr l.plunge	Pm az.	Pm plunge	Pm line	Pm l.plunge	Identifier	Notes
190-1175A-											
1H-3, 94-101	3.94	160	32							Bed	
2H-4, 58-59	12.28									Fold	S-fold in archive half, 1-cm wavelength
3H-1, 43-47	17.13	166	51			288	51			Bed	
3H-1, 51-52	17.21	115	16			237	16			Bed	
3H-1, 87-94	17.57	342	51			104	51			Fold axial plane	Z-fold in archive half, 6-cm amplitude
3H-2, 92-98	19.12	7	55			129	55			Fold axial plane	
3H-5, 113-114	23.83	153	19			275	19			Bed	
3H-6, 8-9	24.28	282	14			44	14			Bed	
3H-6, 117-118	25.37	41	22			163	22			Bed	
4H-1, 84-86	27.04	348	23			288	23			Bed	
4H-3, 76-77	29.96	337	8			277	8			Bed	
4H-5, 117-118	33.37	334	11			274	11			Bed	
5H-1, 32-37	36.02	100	27			141	27			Bed	
5H-1, 87-89	36.57	180	13			221	13			Bed	
5H-1, 109-111	36.79	0	10			41	10			Bed	
5H-3, 59-61	39.29	173	24			214	24			Bed	
5H-6, 35-40	43.55	150	19			191	19			Bed	
6H	45.21	0	0			196	0			Bed	
7H	54.71	0	0			147	0			Bed	
7H-5, 6-10	60.76					147				Dipping laminae	Slump?
7H-5, 60-71	61.30					147				Dipping laminae	Slump?
8H-5, 95-100	71.15	160	40			309	40			Bed	
8H-5, 135-142	71.55	153	50			302	50			Bed	
8H-2, 48-50	66.18	180	16			329	16			Bed	
9H-1, 2	73.71					245				Bedding	Curviplanar vertical bedding
9H-5, 6	79.71					245				Bedding	Moderately inclined curviplanar bedding
10H	83.21	0	0			358	0			Bedding	
11H	92.71					96					Only two sections full of white ash
12H-2, 83-84	103.13	293	25			155	25			Bed	
12H-3, 38-40	104.18	230	27			92	27			Axial plane	Slump?
13H-3, 80-90	114.10	284	68			229	68			Bed	Ash layer
13H-5, 122-123	117.52			130	0			75	0	Fold axis	
13H-6	117.81			315	15			260	15	Fold axis	
13H-4, 100-135	115.80	17	90			322	90			Bed	
13H-4, 48-65	115.28	351	60			296	60			Bed	
13H-5, 16-20	116.46	154	53			99	53			Bed	
14H-1, 125-127	121.05	246	57			129	57			Bed	
14H-2, 40-41	121.70	0	90			243	90			Bed	
14H-3, 62-63	123.42	0	40			243	40			Bed	
14H-4, 60-60	124.90	187	48			70	48			Bed	
14H-6, 119-119	128.49	270	12			153	12			Bed	
14H-4, 11-15	124.41	203	53			86	53			Fold axial plane	
14H-4, 11-15	124.41	357	45			240	45			Fold axis	
15H-1, 50-54	129.80	324	41			240	41			Bed	
15H-1, 98-105	130.28	334	58			250	58			Bed	
15H-5, 116-118	136.46	284	21			200	21			Bed	
16H	138.81	0	0			234	0			Bed	Curviplanar aspect due to drilling
17H-1, 89-91	149.19	277	71			93	71			Bed	

Table T7 (continued).

Core, section, interval (cm)	Depth (mbsf)	Cr az. (°)	Cr dip (°)	Cr line	Cr l.plunge	Pm az.	Pm plunge	Pm line	Pm l.plunge	Identifier	Notes
17H-3, 70-77	152.00	0	42			176	42			Bed	
18H-1, 88-90	158.68	94	52			112	52			Bed	
18H-2, 40-48	159.70	52	57			70	57			Bed	
18H-4, 58-66	162.88	150	60			168	60			Bed	
19H-6, 15-22	174.95	337	53			268	53			Bed	
20H-1, 84-85	177.64	237	18			247	18			Bed	
20H-3, 11-17	179.91	202	50			212	50			Bed	
21H-4, 66-68	191.46	148	19			357	19			Bed	
22H-1, 116-145	196.96	36	41			235	41			Bed	
22H-2, 30-43	197.60	197	66			36	66			Fault	Displaces slump-fold closure
22H-3	198.81					199				Bed	Wholly disaggregated beds
22H-4, 42-59	200.72	169	63			8	63			Bed	
22H-4, 120-133	201.50	16	53			215	53			Bed	
22H-5, 97-106	202.77	323	59			162	59			Axial plane	Isoclinal fold, two in the section
22H-6, 66-105	203.96	20	47			219	47				
23X	205.31										Highly disturbed hemipelagites by XCB coring
23X-2,3,CC	206.81	0	0				0				Evidence of subhorizontal bedding
24X										No recovery	
25X-5,6,CC	230.61	0	0				0			Bed	Subhorizontal bedding
26X	234.31	0	0				0			Bed	Subhorizontal bedding when observed
27X	243.91	0	0				0			Bed	
28X	253.61	0	0				0			Bed	
29X	263.21	0	0				0			Bed	
30X	272.81	0	0				0			Bed	
31X	282.41	0	0				0			Bed	
32X-2, 99-103	294.49	180	5				5			Fissility	Biscuit interval 94-104 cm
32X-5, 85-88	298.85	210	71			259	71			Fault	12-mm reverse displacement, biscuit 81-88 cm
33X	301.61	0	0				0			Bed	
34X										No recovery	
35X										Poor recovery	
36X-CC	330.41	0	0				0			Poor recovery	
37X-6, 4-11	347.54	185	71			85	71			Fault	4-mm normal displacement, biscuit 4-11 cm
38X-1, 57-62	350.17	140	65			100	65			Fault	Anastomosing fault surface
38X-3, 111-119	353.71									Soft sediment deformation	
39X	359.21									Subhorizontal bedding	
39X-1, 112-119	360.32									Small folds	
39X-1, 92-98	360.12									Small folds	
39X-1, 78-83	359.98									Small folds	
40X-CC	368.81									Bed	
41X	378.41									Bed	Horizontal bedding where not convoluted
41X-2, 8-14	379.98									Fold	Convoluted lamination
41X-5, 67-76	385.07	40	64			48	64			Fault	Two normal faults, 10-mm offset
41X-2, 83-91	380.73	186	90			354	90			Fault	Vertical
42X	388.01									Bed	Subhorizontal bedding
42X-1, 55-60	388.55	339	83			59	83			Fault, normal	15-mm offset, not a good biscuit
42X-2, 17-24	389.67	346	71			274	71			Fault, normal	7-mm offset
42X-2, 34-40	389.84	153	66			321	66			Fault, normal	5-mm offset

Table T7 (continued).

Core, section, interval (cm)	Depth (mbsf)	Cr az. (°)	Cr dip (°)	Cr line	Cr l.plunge	Pm az.	Pm plunge	Pm line	Pm l.plunge	Identifier	Notes
42X-2, 65-70	390.15	79	51				51			Fault	Downdip slickenlines on surface
42X-3, 120-123	392.20									Fault	2-mm offset, orientation only apparent (270,72)
43X-1, 36-43	397.96	12	73			47	73			Fault	2 mm wide, no visible displacement
43X-1, 86-102	398.46	151	64			48	64			Fault	Downdip slickenlines
43X-2, 36-37	399.46	254	21			149	21			Bed	
43X-3, 51-52	401.11	221	19			201	19			Bed	
44X-1, 36-41	406.86	204	63			58	63			Web structure	In sandy material
44X-1, 36-41	406.86										Bed, deformation bands or drilling feature
45X											No recovery
46X										Poor recovery	
46X											Small piece with deformation bands
47X										Bed	Subhorizontal bedding

Note: cr az. = azimuth of plane in core reference frame, cr dip = dip of plane in core reference frame, cr line = azimuth of line in core reference frame, cr l.plunge = plunge of line in core reference frame, cr sense = sense of movement in core reference frame, pm az. = azimuth of plane in paleomagnetic reference frame, pm plunge = plunge of plane in paleomagnetic reference frame, pm line = azimuth of line in paleomagnetic reference frame, pm l.plunge = plunge of line in paleomagnetic reference frame, pm. decl.= paleomagnetic declination, pm. inc = paleomagnetic inclination (only, or nothing).This table is also available in **ASCII** format.

Table T8. Nannofossil events recognized, Site 1175.

Nannofossil zones	Datum events	Age (Ma)	Depth (mbsf)	Average sedimentation rate† (m/m.y.)
NN21b	FAD *Emiliania huxleyi* acme*	0.085	23.42	222.5
	LAD *Helicosphaera inversa*	0.14	86.86	
NN21a	FAD *Emiliania huxleyi**	0.26	132.05	
NN20	LAD *Pseudoemiliania lacunosa**	0.46	183.05	
	FAD *Helicosphaera inversa*	0.48	230.73	
	LAD *Reticulofenestra asanoi**	0.8	278.42	
	FAD *Reticulofenestra asanoi**	1.06	303.90	137.6
	LAD *Helicosphaera sellii*	1.46	346.43	
	FAD *Gephyrocapsa oceanica*	1.77	391.47	
NN19	LAD *Discoaster brouweri**	1.95	416.77	

Notes: FAD = first appearance datum, LAD = last appearance datum. * = events used in calculating average sedimentation rate. † = uncorrected for compaction.

Table T9. Interval and depth constraints of calcareous nannofossil events, Hole 1175A.

Event		Interval (cm)		Depth (mbsf)	
		Top	Bottom	Top	Bottom
		190-1175A-	190-1175A-		
B	*Emiliania huxleyi* acme	3H-3, 75-76	3H-CC	20.45	26.39
T	*Helicosphaera inversa*	8H-CC	9H-CC	73.84	83.31
B	*Emiliania huxleyi*	14H-CC	15H-4, 75-76	129.56	134.55
T	*Pseudoemiliania lacunosa*	20H-3, 78-79	20H-CC	180.58	185.52
B	*Helicosphaera inversa*	25H-3, 71-72	26H-CC	228.31	233.16
T	*Reticulofenestra asanoi*	30X-3, 75-76	30X-CC	276.55	280.29
B	*Reticulofenestra asanoi*	32X-CC	33X-4, 73-74	300.98	306.83
T	*Helicosphaera sellii*	37X-3, 64-65	37X-CC	343.64	349.23
B	*Gephyrocapsa oceanica*	42X-2, 75-76	42X-CC	390.25	392.70
T	*Discoaster brouweri*	44X-CC	46X-CC	407.73	425.81

Note: B = bottom occurrence, T = top occurrence.

Table T10. Calcareous nannofossil range chart, Site 1175. (See table notes. Continued on the next page.)

Epoch	Zone	Core, section, interval (cm)	Depth (mbsf)	Preservation	Abundance	*Braarudosphaera bigelowii*	*Calcidiscus leptoporus*	*Calcidiscus macintyrei*	*Ceratolithus cristatus*	*Ceratolithus cristatus* var. *telesmus*	*Coccolithus pelagicus*	*Coccolithus pelagicus* (with bar)	*Cyclolithus annulus*	*Discoaster brouweri*	*Discoaster quinqueramus*	*Discoaster* spp.	*Discoaster variabilis*	*Discosphaera tubifera*	*Emiliania huxleyi*	*Florisphaera profunda*	*Gephyrocapsa muellerae*	*Gephyrocapsa oceanica*	*Gephyrocapsa* spp. (<2 µm)	*Helicosphaera carteri*	*Helicosphaera carteri* var. *wallichii*	*Helicosphaera inversa*	*Helicosphaera sellii*	*Neosphaera coccolithomorpha*	*Oolithotus fragilis*	*Pontosphaera discopora*	*Pontosphaera japonica*	*Pontosphaera multipora*	*Pseudoemiliania lacunosa*	*Pseudoemiliania ovata*	*Reticulofenestra asanoi*	*Reticulofenestra minuta*	*Reticulofenestra minutula*	*Reticulofenestra pseudoumbilicus* (>7 µm)	*Reticulofenestra pseudoumbilicus* (5–7 µm)	*Reticulofenestra* spp.	*Rhabdosphaera clavigera*	*Rhabdosphaera clavigera* var. *stylifera*	*Scapholithus fossilis*	*Scyphosphaera apsteinii*	*Scyphosphaera* spp.	*Sphenolithus* spp.	*Syracosphaera pulchra*	*Syracosphaera* spp.	*Umbellosphaera tenuis*	*Umbilicosphaera hulburtiana*	*Umbilicosphaera rotula*	*Umbilicosphaera sibogae* var. *foliosa*	*Umbilicosphaera sibogae* var. *sibogae*
		190-1175A-																																																			
Pleistocene	NN21b	1H-CC		G	C		C		R				R						D	A	C	A	F	C							F		F								F						F	R	F			C	C
		2H-CC		G	C	F	F					F							A	C	C	A	A	C	F				F		F									F	F		F				F	F	F	F		C	F
		3H-3, 75-77	20.45	P	A		F		R				F						A	A	A	C		F							F																F		F				F
	NN21a	3H-CC		G	C		F					R							A	A	C	A	A	F	R															F							F	F		F		C	C
		4H-CC		G	C		C		R		R	F							C	A	C	A	D	F	R							R									R		F				R	F				F	C
		5H-CC		G	C		C		R	R			R						A	C	C	C	D	F	F				F		F															F	C	F	F			F	F
		6H-CC		G	C		C			R	R	R							C	C	C	A	A	F	F						R																F	F				C	F
		7H-CC		G	C		C												C	A	C	A	D		F																								F				
		8H-CC		G	C		R				R								C	A	C	A	D	R	R						R	R															F					R	F
		9H-CC		G	C		C						F						C	A	F	A	D	F																							F		F			C	F
		10H-CC		G	C		C		R		R								C	C	C	A	D	F	F						R										F						R	R	F			C	F
		11H-CC		G	R														C	A	C	A	A										C																			C	
		12H-CC		G	C		F		R	R	R	R				R			F	C	C	A	D								F		R							R	R	R	R		F	R			F				R
		13H-CC		G	C		F		R			R	F						F	A	C	A	A	F		R		R						F			F			R							F						F
		14H-CC		G	C		F				R								F	C	A	A	D	F		R				F	R																F	F				F	F
	NN20	15H-4, 75-76	134.55	G	C		F					R					R			C	A	A	A	F		F						F					C										F						F
		15H-CC		G	C		F													C	A	A	A	R	R																												
		16H-CC		G	C		F				R									C	A	A	A	F		F					R																					F	
		17H-CC		G	C		C			R										C	A	A	A										F	F																			F
		18H-CC		G	C		F													A	A	A	A																				F				F	F		F		F	
		19H-CC		G	C				R		R	R								C	D	C	A	R	R	R				F											F		R				F	F					
		20H-3, 78-79	180.58	G	C		F									F				A	D	C	A	F		R							R																			F	C
	NN19	20H-CC		VG	C		F													C	D	C	A			R				F			C	C						F	R						R					F	C
		21H-CC		M	C		C	R	R		R									C	A	A	A	F										C							R		R				F					F	F
		22H-CC		G	C		C				F									A	A	A	A		R	R							R																			F	F
		23X-CC		G	C		C		R							R				A	A	A	A	F	F						R		F								R						F		F			F	F
		25X-3, 71-72	228.31	G	C							F								A	A	A	A	F		R							F	F															F			C	
		25X-CC		G	C		C													A	A	A	A	F		R							F							F			F									F	
		26X-CC		G	C		F													F	D	C	A	F						R	R		F	F						F								C					F
		27X-CC		G	C		F													A	A	A	A	F						R		R	C	C								R		R			R					F	F
		28X-CC		G	C		C		R		F	R								A	A	C	A										C	C																		C	
		29X-CC		M	C		F		R	R		R	R							A	C	F	D	F	R					R	R		C	F			C										F						F
		30X-3, 75-76	276.55	M	C		C		R		R	R									A	A	D	R	R								C	F			C										F		F			F	R
		30X-CC		G	C		C													A	A	C	D	C							F		C	C	F						F										F	F	
		31X-CC		M	C		C													A	A	A											A	C																			
		32X-CC		G	C		C	F	R		F									A			A	F							F		A	C		C	A	R										F				R	F

Table T10 (continued).

Epoch	Zone	Core, section, interval (cm)	Depth (mbsf)	Preservation	Abundance	*Braarudosphaera bigelowii*	*Calcidiscus leptoporus*	*Calcidiscus macintyrei*	*Ceratolithus cristatus*	*Ceratolithus cristatus* var. *telesmus*	*Coccolithus pelagicus*	*Coccolithus pelagicus* (with bar)	*Cyclolithus annulus*	*Discoaster brouweri*	*Discoaster quinqueramus*	*Discoaster* spp.	*Discoaster variabilis*	*Discosphaera tubifera*	*Emiliania huxleyi*	*Florisphaera profunda*	*Gephyrocapsa muellerae*	*Gephyrocapsa oceanica*	*Gephyrocapsa* spp. (<2 µm)	*Helicosphaera carteri*	*Helicosphaera carteri* var. *wallichii*	*Helicosphaera inversa*	*Helicosphaera sellii*	*Neosphaera coccolithomorpha*	*Oolithotus fragilis*	*Pontosphaera discopora*	*Pontosphaera japonica*	*Pontosphaera multipora*	*Pseudoemiliania lacunosa*	*Pseudoemiliania ovata*	*Reticulofenestra asanoi*	*Reticulofenestra minuta*	*Reticulofenestra minutula*	*Reticulofenestra pseudoumbilicus* (>7 µm)	*Reticulofenestra pseudoumbilicus* (5–7 µm)	*Reticulofenestra* spp.	*Rhabdosphaera clavigera*	*Rhabdosphaera clavigera* var. *stylifera*	*Scapholithus fossilis*	*Scyphosphaera apsteinii*	*Scyphosphaera* spp.	*Sphenolithus* spp.	*Syracosphaera pulchra*	*Syracosphaera* spp.	*Umbellosphaera tenuis*	*Umbilicosphaera hulburtiana*	*Umbilicosphaera rotula*	*Umbilicosphaera sibogae* var. *foliosa*	*Umbilicosphaera sibogae* var. *sibogae*
Pleistocene	NN19	33X-4, 73-74	306.83	G	C		F									R				C	C	A	D	F	F								F	F																F
		33X-CC		G	C		C						F							A	C	A	D									F	C	C																
		34X-CC		M	F		C		R		F				R					A	A	A	D	F							F	F	F	C															F
		35X-CC		M	F		C													A	A	C	A										C	C							C									
		36X-CC		P	R																A	A	A																		C									
		37X-3, 64-65	343.64	G	C		C													A	C	A	A	F									C	F																
		37X-CC		M	C		C				R									A	C	A	D				R					R	C	C																C
		38X-CC		M	R		C													C	A	A	A	C			F						C	C		C														
		39X-CC		P	R		F													A	A	C	A											C		C	C													
		40X-CC		P	R											F				C	A	A	A										C		C															
		41X-CC		P	R		R					F								A	A	A	A	F								F	F									F								
		42X-2, 75-76	390.25	G	C		C				F									A	A	A	A										C	F			C													
		42X-CC		G	C		C					F				R				A	C	C	A	F										F	A		C													
		43X-CC		G	C		C	C	F							F				A	A	C		C										A	A		C													
		44X-CC		M	R			A			A			C		C							A											C	C								C								
Pliocene	NN18	46X-CC		M	C		C				F			C		C				A			A		C								C	C			C	A		C									
		47X-CC		M	R																																	A	D											

Notes: Abundance: C = common, F = few, R = rare. Preservation: P = poor, M = moderate, G = good. See **"Biostratigraphy,"** p. 9, in the "Explanatory Notes" chapter. This table is also available in **ASCII** format.

Table T11. Depths and ages of magnetic chrons identified, Site 1175.

Depth (mbsf)				Age
Top	Bottom	Polarity	Chron boundary	(Ma)
0.00	298.80	N	Brunhes (start)	
17.00	17.30	R		
24.00	24.15	R		
35.73	35.93	R		
73.00	74.30	R		
92.75	94.25	R		
158.00	159.35	R		
205.35	205.65	R		
298.80		R	Brunhes/Matuyama	0.78

Note: N = normal, R = reversed.

Table T12. Pore fluid compositions, Hole 1175A.

Hole, core, section, interval (cm)	Depth (mbsf)	pH (ISE)	Alk(T) (mM)	Sal (R)	Cl (T) (mM)	SO_4 (I) (mM)	Na (I) (mM)	Mg (I) (mM)	Ca (I) (mM)	K (I) (mM)	H_4SiO_4 (S) (µM)	NH_4 (S) (mM)
190-1175A-												
1H-1, 140-150	1.40				557.0	19.2		51.9	7.46	11.2	556	1.04
1H-2, 140-150	2.90	7.62		34.0	558.0	15.6	479	50.1	6.06	11.3	668	
1H-3, 140-150	4.40	7.88	19.3	34.0	558.0	13.2	480	49.8	5.69	11.3	690	1.46
1H-4, 140-150	5.90	7.89	22.1	34.0	559.0	11.1	482	49.0	4.92	11.5	770	
1H-5, 68-78	6.68	7.86	23.5	34.0	559.0	10.0	483	48.4	4.80	11.5	761	
2H-1, 140-150	8.60	7.96	27.5	33.8	557.0	5.42	480	46.9	3.68	11.3	781	2.36
2H-2, 140-150	10.10	7.79	29.0	33.8	556.0	4.01	480	46.6	3.24	11.3	772	
2H-3, 140-150	11.60	7.91	31.2	33.5	557.0	2.26	482	45.6	3.15	11.2	787	
2H-4, 140-150	13.10	7.85	32.8	33.5	561.0	1.01	485	45.8	2.99	11.2	828	
2H-5, 140-150	14.60	7.94	33.1	33.5	562.0	0.73	487	45.1	3.00	11.0	822	
2H-6, 90-100	15.60	7.66	32.8	33.8	562.0	0.26	484	46.1	2.75	11.0	813	2.52
3H-1, 140-150	18.10	7.79	32.4	33.8	561.0	0.40	484	45.4	2.84	11.1	785	
3H-3, 140-150	21.10	7.94	31.8	33.5	561.0	0.71	484	45.8	2.67	10.9	690	2.71
3H-4, 140-150	22.60	8.09	33.2	33.5	561.0	0.60	483	46.8	2.59	10.7	722	
3H-6, 130-150	25.50	8.05	32.6	34.0	558.0	0.41	479	46.7	2.88	10.5	670	2.64
4H-2, 140-150	29.10	8.04	32.6	33.0	561.0	1.11	485	45.5	2.87	10.8		
4H-4, 140-150	32.10	8.06	32.8	33.5	561.0	0.51	484	45.0	3.07	11.1		3.43
4H-6, 140-150	35.10	8.05	32.0	34.0	558.0	0.25	480	44.7	2.89	11.4		
5H-2, 140-150	38.60	7.69	32.8	33.5	558.0	0.93	482	44.8	3.11	10.8	746	3.64
5H-5, 140-150	43.10	7.87	32.4	33.8	561.0	0.36	486	43.2	3.33	10.9	716	
6H-4, 135-150	51.05	7.99	30.7	33.4	557.0	0.18	481	42.6	3.25	11.1		4.25
7H-3, 135-150	59.05	7.89	29.5	33.0	562.0	1.08	488	41.9	3.09	10.6	632	
8H-3, 135-150	68.55	8.03	27.6	33.0	562.0	0.65	490	39.8	3.06	10.4	790	
9H-3, 135-150	78.05	7.82	27.6	33.5	557.0	0.29	483	40.2	3.19	10.1	822	5.24
10H-2, 135-150	86.05	7.84	27.7	33.0	561.0	1.06	491	39.1	3.06	10.4	761	
12H-4, 135-150	106.65	7.69	27.5	33.0	562.0	0.54	491	38.5	3.30	10.4	831	
13H-4, 135-150	116.15	7.84	27.3	32.5	557.0	0.58	486	38.6	3.17	10.8	813	5.36
14H-5, 140-150	127.20	7.70	24.5	33.0	561.0	0.44	488	38.2	3.12	10.5	746	
15H-4, 140-150	135.20	7.87	26.2	33.0	557.0	0.32	485	38.2	3.09	11.2	735	
16H-4, 140-150	144.70	7.62	25.6	33.0	554.5	0.55	484	36.8	3.58	10.9	796	5.18
17H-4, 145-150	154.25	7.81	25.3	33.0	554.0	0.87	485	36.4	3.46	11.0	822	
18H-4, 145-150	163.75	7.67	24.8	33.0	553.5	0.58	485	36.0	3.45	10.7	761	
19H-4, 145-150	173.25	7.84	23.4	33.0	552.0	0.95	483	35.8	3.41	10.9	802	5.40
20H-4, 145-150	182.75	7.84	22.8	33.0	587.0	0.35	516	35.2	3.81	10.8	883	
21H-4, 135-150	192.15	7.54	22.6	32.5	561.0	0.28	491	35.1	3.65	10.6	893	
22H-4, 145-150	201.75	7.66	21.7	32.5	554.0	0.78	485	34.8	3.74	10.6	854	5.18
23X-4, 98-113	210.78	7.66	22.0	32.5	556.5	1.10	483	36.9	3.99	11.1	841	
25X-3, 130-150	228.90	7.60	22.5	32.5	557.5	0.70	486	35.3	4.64	10.2	893	
26X-4, 130-150	240.10	7.52	22.0	32.5	551.0	1.09	482	35.0	4.43	9.9	960	4.70
27X-4, 120-150	249.60	7.72	22.0	32.5	552.0	0.42	481	35.2	4.38	10.1	874	
28X-5, 120-150	260.80	7.64	23.0	32.5	553.0	0.14	481	36.0	3.97	10.7	857	
29X-5, 120-150	270.40	7.52	23.6	32.5	557.0	1.09	486	37.2	4.21	10.3	982	3.69
30X-2, 120-150	275.50	7.52	24.4	32.5	554.0	0.50	482	37.9	4.11	10.3	939	
31X-4, 120-150	288.10	7.50	24.7	33.0	550.0	1.38	476	39.4	4.50	10.2	976	
32X-3, 120-150	296.20			33.0	559.5	0.65	486	39.5	4.29	10.1	939	2.63
33X-2, 120-150	304.30	7.56	27.2	33.0	553.0	0.71	480	40.0	4.52	9.9	924	
37X-4, 120-150	345.70	7.54	25.1	33.0	551.0	0.53	472	41.9	4.67	9.5	941	
38X-2, 120-150	352.30	7.50	23.5	33.0	555.0	0.00	476	40.9	4.84	9.1	965	1.79
39X-2, 100-150	361.70	7.63	22.6	32.5	555.0	0.00	477	40.4	4.63	9.4	861	
41X-2, 110-150	381.00	7.60	20.2	32.5	553.0	0.75	476	39.5	4.50	9.0	913	
42X-2, 115-150	390.65	7.87	18.8	32.5	553.0	0.84	475	39.5	4.51	9.3	770	
43X-2, 115-150	400.25	7.93	16.9	32.2	553.0	0.40	473	38.0	5.49	8.7	748	1.55

Note: ISE = ion selective electrode, Alk = alkalinity, T = titration, Sal = salinity, R = refractometry, I = ion, S = spectrophotometry.

Table T13. Headspace gas and vacutainer analysis, Hole 1175A.

Core, section, interval (cm)	Depth (mbsf)	Sample method	C_1/C_2	C_1 (ppm)	C_2 (ppm)	C_2= (ppm)	C_3 (ppm)	C_3= (ppm)
190-1175A-								
1H-5, 0-5	6.00	HS		2	0.0	0.0	0.0	0.0
2H-4, 0-5	11.70	HS		4	0.0	0.0	0.0	0.0
3H-2, 0-5	18.20	HS		6,018	0.0	0.0	0.0	0.0
4H-6, 0-5	33.70	HS		9,774	0.0	0.0	0.0	0.0
5H-5, 0-5	41.70	HS		11,682	0.0	0.0	0.0	0.0
6H-2, 0-5	46.70	HS		36,920	0.0	0.0	0.0	0.0
6H-5, 0-5	51.20	HS		9,896	0.0	0.0	0.0	0.0
6H-5, 127-128	52.47	VAC	232,755	558,612	2.4	0.0	0.0	0.0
7H-4, 0-5	59.20	HS		13,883	0.0	0.0	0.0	0.0
8H-4, 0-5	68.70	HS		32,260	0.0	0.0	0.0	0.0
9H-4, 0-5	78.20	HS	97,131	29,139	0.3	0.0	0.0	0.0
10H-3, 0-5	86.20	HS		29,804	0.0	0.0	0.0	0.0
11H-1, 0-5	92.70	HS		384	0.0	0.0	0.0	0.0
12H-2, 0-5	102.30	HS		19,065	0.0	0.0	0.0	0.0
13H-4, 0-5	114.80	HS		31,897	0.0	0.0	0.0	0.0
14H-4, 0-5	124.30	HS		4,488	0.0	0.0	0.0	0.0
15H-5, 0-5	135.30	HS		10,289	0.0	0.0	0.0	0.0
16H-5, 0-5	144.80	HS		13,876	0.0	0.0	0.0	0.0
17H-2, 0-5	149.80	HS		9,652	0.0	0.0	0.0	0.0
18H-2, 0-5	159.30	HS		7,729	0.0	0.0	0.0	0.0
19H-5, 0-5	173.30	HS		7,614	0.0	0.0	0.0	0.0
20H-5, 0-5	182.80	HS		2,427	0.0	0.0	0.0	0.0
21H-5, 0-5	192.30	HS		4,039	0.0	0.0	0.0	0.0
22H-2, 0-5	197.30	HS		11,101	0.0	0.0	0.0	0.0
23X-5, 0-5	210.93	HS	12,790	5,116	0.4	0.3	0.0	0.0
25X-4, 0-5	229.10	HS	51,740	20,696	0.4	0.3	0.0	0.0
26X-5, 0-5	240.30	HS	51,784	20,714	0.4	0.0	0.0	0.0
27X-5, 0-5	249.90	HS	52,029	20,812	0.4	0.0	0.0	0.0
28X-6, 0-5	261.10	HS	49,710	34,797	0.7	0.6	0.0	0.0
29X-6, 0-5	270.70	HS	50,073	25,037	0.5	0.0	0.0	0.0
30X-3, 0-5	275.80	HS		10,926	0.0	0.0	0.0	0.0
31X-3, 0-5	285.40	HS		4,913	0.0	0.0	0.0	0.0
32X-2, 0-5	293.50	HS		8,746	0.0	0.0	0.0	0.0
33X-5, 0-5	307.60	HS		7,166	0.0	0.0	0.0	0.0
37X-5, 0-5	346.00	HS		3,785	0.0	0.0	0.0	0.0
38X-3, 0-5	352.60	HS		1,591	0.0	0.0	0.0	0.0
39X-1, 0-5	359.20	HS		1,482	0.0	0.0	0.0	0.0
40X-CC, 0-5	368.80	HS		2,737	0.0	0.0	0.0	0.0
41X-3, 0-5	381.40	HS	8,063	3,225	0.4	0.0	0.0	0.0
42X-2, 0-5	389.50	HS		310	0.0	0.0	0.0	0.0
43X-3, 0-5	400.60	HS		11	0.0	0.0	0.0	0.0
44X-1, 0-5	406.50	HS		23	0.0	0.0	0.0	0.0

Note: HS = headspace, VAC = vacutainer.

Table T14. Carbon, nitrogen, sulfur, and hydrogen analyses, Hole 1175A.

Core, section, interval (cm)	Depth (mbsf)	Inorganic C (wt%)	$CaCO_3$ (wt%)	TOC (wt%)	Organic C (wt%)	N (wt%)	S (wt%)	H (mg HC/g of sediment)
190-1175A-								
1H-2, 139-140	2.89	0.62	5.22	NA	NA	NA	NA	NA
1H-4, 137-138	5.87	1.20	10.07	NA	NA	NA	NA	NA
1H-5, 69-70	6.69	1.26	10.51	NA	NA	NA	NA	NA
2H-1, 136-137	8.56	1.12	9.38	NA	NA	NA	NA	NA
2H-2, 137-138	10.07	1.76	14.67	NA	NA	NA	NA	NA
2H-3, 137-138	11.57	1.31	10.91	NA	NA	NA	NA	NA
3H-1, 136-137	18.06	1.52	12.71	NA	NA	NA	NA	NA
3H-3, 136-137	21.06	1.58	13.17	NA	NA	NA	NA	NA
3H-5, 127-128	23.97	0.43	3.62	NA	NA	NA	NA	NA
4H-2, 139-140	29.09	1.24	10.39	NA	NA	NA	NA	NA
4H-4, 138-139	32.08	0.87	7.24	NA	NA	NA	NA	NA
4H-6, 140-141	35.10	0.50	4.18	NA	NA	NA	NA	NA
5H-2, 136-137	38.56	1.06	8.87	NA	NA	NA	NA	NA
5H-5, 137-138	43.07	1.12	9.38	NA	NA	NA	NA	NA
6H-4, 111-112	50.81	2.37	19.81	NA	NA	NA	NA	NA
7H-2, 127-128	57.47	0.75	6.25	NA	NA	NA	NA	NA
7H-3, 79-80	58.49	0.27	2.32	NA	NA	NA	NA	NA
7H-4, 29-30	59.49	0.17	1.48	NA	NA	NA	NA	NA
8H-3, 123-124	68.43	1.37	11.42	NA	NA	NA	NA	NA
8H-7, 35-36	73.55	0.33	2.76	NA	NA	NA	NA	NA
9H-3, 134-135	78.04	1.73	14.42	NA	NA	NA	NA	NA
9H-5, 8-9	79.78	2.25	18.77	NA	NA	NA	NA	NA
9H-6, 140-145	82.60	2.14	17.87	NA	NA	NA	NA	NA
10H-2, 134-135	86.04	1.39	11.63	NA	NA	NA	NA	NA
11H-2, 50-51	94.70	0.11	0.93	NA	NA	NA	NA	NA
12H-4, 105-106	106.35	1.45	12.10	NA	NA	NA	NA	NA
13H-4, 132-133	116.12	2.27	18.96	NA	NA	NA	NA	NA
14H-5, 136-137	127.16	2.96	24.73	NA	NA	NA	NA	NA
15H-3, 135-136	133.65	1.74	14.52	NA	NA	NA	NA	NA
16H-1, 77-78	139.57	2.09	17.42	NA	NA	NA	NA	NA
16H-3, 131-132	143.11	4.59	38.27	NA	NA	NA	NA	NA
17H-3, 143-144	152.73	2.15	17.94	NA	NA	NA	NA	NA
18H-3, 143-144	162.23	3.19	26.63	NA	NA	NA	NA	NA
19H-4, 134-135	173.14	2.21	18.45	NA	NA	NA	NA	NA
20H-4, 135-136	182.65	2.37	19.81	NA	NA	NA	NA	NA
21H-4, 134-135	192.14	2.03	16.95	NA	NA	NA	NA	NA
22H-4, 141-142	201.71	2.14	17.87	NA	NA	NA	NA	NA
23X-3, 66-67	208.96	2.41	20.10	NA	NA	NA	NA	NA
23X-4, 90-91	210.70	2.55	21.28	NA	NA	NA	NA	NA
23X-7, 51-52	214.44	3.59	29.93	NA	NA	NA	NA	NA
25X-3, 127-128	228.87	1.25	10.45	NA	NA	NA	NA	NA
26X-3, 129-130	238.59	2.85	23.76	NA	NA	NA	NA	NA
26X-4, 127-128	240.07	1.93	16.12	NA	NA	NA	NA	NA
27X-4, 119-120	249.59	2.53	21.10	NA	NA	NA	NA	NA
28X-2, 118-120	256.28	1.41	11.75	NA	NA	NA	NA	NA
28X-5, 117-118	260.77	1.67	13.99	NA	NA	NA	NA	NA
28X-6, 54-55	261.64	1.41	11.79	NA	NA	NA	NA	NA
29X-5, 118-119	270.38	2.42	20.20	NA	NA	NA	NA	NA
30X-2, 114-115	275.44	2.72	22.72	NA	NA	NA	NA	NA
31X-4, 119-120	288.09	1.50	12.52	NA	NA	NA	NA	NA
33X-2, 114-115	304.24	1.60	13.37	NA	NA	NA	NA	NA
33X-3, 118-119	305.78	1.40	11.69	NA	NA	NA	NA	NA
33X-6, 57-58	309.67	1.75	14.58	NA	NA	NA	NA	NA
37X-4, 119-120	345.69	0.66	5.55	NA	NA	NA	NA	NA
37X-5, 134-135	347.34	0.79	6.58	NA	NA	NA	NA	NA
38X-2, 114-115	352.24	0.70	5.91	NA	NA	NA	NA	NA
39X-2, 103-104	361.73	0.44	3.73	NA	NA	NA	NA	NA
40X-CC, 21-22	369.01	0.81	6.79	NA	NA	NA	NA	NA
41X-2, 105-106	380.95	0.96	8.01	NA	NA	NA	NA	NA
42X-2, 112-113	390.62	0.77	6.42	NA	NA	NA	NA	NA
43X-2, 70-71	399.80	0.41	3.48	NA	NA	NA	NA	NA
43X-CC, 23-24	402.14	0.54	4.55	NA	NA	NA	NA	NA
44X-1, 46-47	406.96	0.77	6.47	NA	NA	NA	NA	NA
46X-CC, 1-2	425.81	0.13	1.11	NA	NA	NA	NA	NA
47X-CC, 13-14	435.53	0.17	1.45	NA	NA	NA	NA	NA

Notes: TOC = total organic carbon, HC = hydrocarbon. NA = not analyzed.

Table T15. Total bacterial populations in sediments, Site 1175.

Depth (mbsf)	Bacterial cells (cells/cm^3)
1.16	6.97×10^7
8.59	3.85×10^7
14.59	9.95×10^6
21.09	1.51×10^7
32.09	2.20×10^7
38.59	8.18×10^6
50.82	7.28×10^7
59.04	3.71×10^5
78.04	8.09×10^6
106.39	6.59×10^6
135.19	8.87×10^6
193.54	6.11×10^6
228.89	4.08×10^6
270.39	3.75×10^6
299.21	4.44×10^6
345.69	1.01×10^6
380.99	1.63×10^6
399.99	3.59×10^5

Table T16. Comparison of near-surface sediment bacterial populations at Site 1175 with data from nine other ODP sites with different overlying-water depths.

Location	ODP leg-site	Depth (mbsf)	Total bacteria (cells/cm^3)
Peru margin	112-681	150	1.05×10^9
Santa Barbara Basin	146-893	577	1.27×10^9
Japan Sea	128-798	900	7.82×10^8
Woodlark Basin	180-1115	1150	2.83×10^8
Cascadia margin	146-890	1326	6.95×10^8
Woodlark Basin	180-1109	2211	3.28×10^8
Juan de Fuca Ridge	139-857	2419	8.28×10^8
Cascadia margin	146-888	2516	5.32×10^8
Lau Basin	135-834	2703	6.12×10^8
Woodlark Basin	180-1108	3188	2.67×10^8
Amazon Fan	155-940	3195	5.62×10^8
Amazon Fan	155-934	3432	6.04×10^8
Eastern Equatorial Pacific	138-851	3760	2.08×10^8
Nankai Trough	190-1173	4791	7.23×10^7
	190-1174	4751	1.47×10^8
	190-1175	2998	6.97×10^7

Table T17. Drilling fluid intrusion estimated based on PFT tracer experiments, Hole 1175A.

Core, section	Total sample weight (g)			Bulk density (g/cm^3)	PFT peak area			Drilling fluid (µL)/sediment (g)		
	Outside	Quarter	Center		Outside	Quarter	Center	Outside	Quarter	Center
190-1175A-										
5H-1	3.07	2.92	3.13	1.62	167	443	174	BD	0.26	BD
5H-3	3.43	3.66	3.98	1.61	352	187	524	0.09	BD	0.29
5H-5	3.00	3.07	3.18	1.63	367	1300	117	0.13	1.68	BD
6H-1	1.87	2.60	3.26	1.58	404	71	343	0.30	BD	0.08
6H-3	3.17	2.71	2.93	1.50	142	390	174	BD	0.18	BD
6H-5	2.90	2.79	1.66	1.68	685	269	401	0.70	BD	0.32

Note: BD = below detection (0.01 µL drilling fluid).

Table T18. Fluorescent microsphere tracer experiments, Hole 1175A.

Core, section	Total sample weight (g)			Microspheres/sediment (g)			Microspheres/sediment (g)		
	Outside	Quarter	Center	Outside	Quarter	Center	Outside	Quarter	Center
190-1175A-									
5H-1	3.07	2.92	3.13	0	52	0	0	18	0
5H-3	3.43	3.66	3.98	149,613	0	0	43,578	0	0
5H-5	3.00	3.07	3.18	157,420	0	0	52,416	0	0
6H-1	1.87	2.60	3.26	0	0	0	0	0	0
6H-3	3.17	2.71	2.93	253	5191	0	80	1,914	0
6H-5	2.90	2.79	1.66	466	0	0	161	0	0

Table T19. Formation factor data from the needle-probe method, Hole 1175A.

Core, section, interval (cm)	Depth (mbsf)	Lithologic type	Formation factor	
			y	z
190-1175A-				
1H-3, 110	4.10	Clayey silt	2.47	2.59
1H-5, 44	6.44	Clayey silt	2.65	2.73
2H-2, 120	9.90	Clayey silt	2.93	2.98
2H-5, 122	14.42	Clayey silt	3.26	3.30
3H-2, 96	19.16	Clayey silt	3.24	3.49
3H-5, 114	23.84	Clayey silt	3.10	3.38
4H-2, 106	28.76	Clayey silt	2.65	2.81
4H-5, 82	33.02	Clayey silt	3.29	3.71
5H-2, 128	38.48	Clayey silt	2.96	3.02
5H-4, 81	41.01	Clayey silt	3.30	3.40
6H-2, 70	47.40	Clayey silt	3.72	4.43
6H-5, 92	52.12	Clayey silt	4.44	6.70
7H-2, 121	57.41	Clayey silt	2.91	2.97
7H-2, 60	56.80	Sand-silt-clay	3.99	4.09
7H-5, 42	61.12	Clayey silt	3.49	5.01
8H-2, 82	66.52	Clayey silt	3.18	3.20
8H-4, 66	69.36	Clayey silt	3.80	4.09
8H-6, 68	72.38	Clayey silt	3.79	4.75
9H-2, 5	75.25	Clayey silt	3.44	4.35
9H-4, 69	78.89	Clayey silt	3.43	4.18
9H-6, 67	81.87	Clayey silt	3.50	4.14
10H-2, 31	85.01	Clayey silt	3.51	3.84
10H-5, 82	90.02	Clayey silt	3.57	4.03
12H-2, 58	102.88	Clayey silt	3.63	3.89
12H-5, 64	107.44	Clayey silt	3.43	3.82
13H-2, 63	112.43	Clayey silt	3.88	4.11
13H-5, 64	116.94	Clayey silt	3.64	3.98
14H-2, 64	121.94	Clayey silt	4.31	4.70
15H-2, 62	131.42	Clayey silt	3.99	4.00
15H-5, 86	136.16	Clayey silt	5.22	5.79
15H-5, 90	136.20	Clayey silt	5.46	6.41
16H-2, 82	141.12	Clayey silt	3.66	3.74
16H-6, 82	147.12	Clayey silt	4.29	4.85
17H-2, 70	150.50	Clayey silt	4.23	4.27
17H-6, 70	156.50	Clayey silt	4.98	5.91
17H-6, 60	156.40	Clayey silt	5.21	4.91
18H-2, 80	160.10	Clayey silt	4.43	4.62
18H-5, 83	164.63	Clayey silt	5.15	6.53
18H-6, 37	165.67	Clayey silt	4.57	5.14
19H-3, 70	171.00	Clayey silt	4.53	5.33
19H-6, 66	175.46	Clayey silt	3.69	4.10
19H-5, 82	174.12	Clayey silt	4.32	4.82
20H-2, 64	178.94	Clayey silt	4.34	4.61
20H-4, 65	181.95	Clayey silt	5.20	6.10
20H-6, 65	184.95	Clayey silt	6.06	7.73
21H-2, 82	188.62	Clayey silt	3.58	3.77
21H-4, 118	191.98	Clayey silt	4.14	4.15
21H-6, 89	194.69	Clayey silt	4.21	4.48

Note: y and z = probe axis.

Table T20. Electrical conductivities and formation factor data for cubes, Hole 1175A.

Core, section, interval (cm)	Depth (mbsf)	Conductivity (S/m)			Temp (°C)	Formation factor		
		x	y	z		x	y	z
190-1175A-								
25X-2, 24	226.34	1.53	1.24	0.98	26.1	3.53	4.35	5.50
26X-3, 104	238.34	1.05	1.32	1.24	26.1	5.17	4.08	4.36
26X-4, 16	238.96	1.30	1.33	1.15	26.1	4.18	4.06	4.70
27X-4, 93	249.33	1.13	1.13	1.16	26.1	4.78	4.77	4.68
27X-7, 6	252.96	1.31	1.24	1.19	26.1	4.14	4.37	4.56
28X-3, 65	257.25	1.21	1.20	1.08	26.0	4.46	4.50	5.02
28X-4, 53	258.63	1.15	1.18	1.07	26.1	4.70	4.59	5.08
28X-5, 74	260.34	1.17	1.18	1.05	26.1	4.64	4.59	5.16
29X-6, 31	271.01	1.16	1.15	1.01	28.9	4.89	4.94	5.65
30X-4, 10	277.40	1.30	1.25	1.04	28.8	4.37	4.56	5.49
30X-5, 51	279.31	1.29	1.19	1.13	28.8	4.40	4.75	5.03
31X-2, 77	284.67	1.02	0.98	0.90	28.4	5.53	5.73	6.26
31X-5, 100	289.40	1.12	1.11	1.08	28.5	5.03	5.09	5.25
32X-2, 7	293.57	1.30	1.31	1.12	28.4	4.35	4.29	5.03
32X-5, 91	298.91	1.04	1.05	1.00	28.4	5.45	5.37	5.63
33X-3, 79	305.39	1.08	1.15	1.03	27.7	5.15	4.85	5.38
33X-6, 26	309.36	1.14	1.21	0.96	27.7	4.90	4.60	5.79
37X-2, 89	342.39	0.79	0.82	0.76	27.8	7.11	6.77	7.34
37X-5, 70	346.70	0.91	0.94	0.77	27.8	6.12	5.91	7.28
38X-1, 67	350.27	0.82	0.82	0.77	27.7	6.83	6.75	7.26
38X-2, 13	351.23	1.00	0.94	0.74	27.8	5.56	5.91	7.53
39X-1, 19	359.39	0.92	0.98	0.75	28.0	6.09	5.71	7.48
39X-2, 71	361.41	0.90	0.89	0.83	28.0	6.24	6.29	6.76
41X-2, 31	380.21	0.83	0.75	0.79	28.0	6.78	7.42	7.06
42X-2, 110	390.60	0.78	0.84	0.68	28.0	7.22	6.63	8.26
43X-1, 67	398.27	0.80	0.82	0.72	28.0	7.01	6.81	7.79
43X-3, 27	400.87	0.83	0.80	0.67	28.0	6.72	6.96	8.40
44X-1, 48	406.98	0.47	0.52	0.49	28.0	12.03	10.73	11.51

Note: x, y, and z = probe axes.

Table T21. Summary of temperature measurements, Hole 1175A.

Depth (mbsf)	Tool	Measurement location	In situ temperature (°C)
0.0	Adara	Mudline	1.50
35.7	Adara	Bottom of Core 4H	4.52
129.3	Adara	Bottom of Core 14H	8.02
216.1	DVTP	After Core 3X	13.40
273.9	DVTP	After Core 29X	16.16

Note: DVTP = Davis-Villinger temperature probe.